

---

# Ionization Based State Read Out of a single $^{87}\text{Rb}$ Atom

Michael Krug

---



München 2017



---

# Ionization Based State Read Out of a single $^{87}\text{Rb}$ Atom

Michael Krug

---

Dissertation  
an der Fakultät für Physik  
der Ludwig–Maximilians–Universität  
München

vorgelegt von  
Michael Krug  
aus München

München, den 8. Dezember 2017

Erstgutachter: Prof. Dr. Harald Weinfurter  
Zweitgutachter: Prof. Jörg Schreiber  
Tag der mündlichen Prüfung: 30. Januar 2018

”After sleeping through a hundred million centuries  
we have finally opened our eyes on a sumptuous  
planet sparkling with color, bountiful with life.  
Within decades, we must close our eyes again. Isn’t it  
a noble, enlightened way of spending our brief time  
in the sun to work at understanding the universe and  
how we have come to wake up in it? This is how I  
answer when I am asked, as I am surprisingly often,  
why I bother to get up in the mornings.”

*Richard Dawkins*

# Zusammenfassung

Verschränkung ist nach E. Schrödinger die fundamentale Charakteristik der Quantenmechanik. Einerseits lebt ein verschränkter Zustand zweier Spin- $\frac{1}{2}$ -Teilchen auf einem vier-dimensionalen Hilbert-Raum und die Theorie, um diesen Zustand zu beschreiben, ist hinreichend verstanden. Auf der anderen Seite ist die experimentelle Realisierung verschränkter Systeme, im Besonderen hybride Licht-Materie-Systeme und deren Nachweis noch immer ein anspruchsvoller Prozess. Ausgehend von einem Quantensystem, das aus einem verschränkten Atom-Photon-Paar besteht, wird hier die experimentelle Anwendung des entanglement swapping Protokolls verwendet, um einen Grundknotenpunkt einer Quanten-Repeater Verbindung aufzubauen, die aus zwei verschränkten Atomen besteht. Die angekündigte Erzeugung von Verschränkung zwischen zwei Atomen bereitet den Weg hin zu einem beweiskräftigem Experiment, um eine lokal-realistische Beschreibung der Welt zu falsifizieren. Ein Hauptbestandteil für diese Experimente ist die schnelle und zuverlässige Auslese des Atomzustandes von  $^{87}\text{Rb}$ .

Diese Arbeit beschreibt die Methode und Experimente zur Analyse des Quantenzustandes eines einzelnen  $^{87}\text{Rb}$ -Atoms unter Verwendung der Photo-Ionisierung. Das Ionisations-Schema basiert auf einem Zwei-Photon-Absorptionsprozess. Das erste Photon ist entweder mit der  $D_1$ - oder  $D_2$ -Linie von  $^{87}\text{Rb}$  resonant, während das zweite Photon eine ausreichend kurze Wellenlänge besitzt, um den angeregten und nur den angeregten Zustand zu ionisieren. Zuerst wird der Einfluss des Ionisationslasers auf die atomaren Niveaus und die entsprechenden Wellenlängen untersucht. Theoretische Überlegungen aus der Zeit-abhängigen Störungsrechnung scheinen imstande zu sein, die beobachtete Verschiebung der atomaren Resonanz-Levels zu erklären, wenn man sie mit den experimentellen Ergebnissen vergleicht. Die Linienbreite der atomaren Resonanzen wird durch den Ionisationslaser vergrößert. Dies kann durch numerisches Lösen der Lindblad-Gleichung erklärt werden und eine große Übereinstimmung wird beobachtet.

Das Hauptthema dieser Arbeit ist das Auslesen eines allgemeinen Zeeman-Zustandes, d.h. Superpositionen der entarteten  $5^2S_{1/2}, |F = 1\rangle$  Mannigfaltigkeit von  $^{87}\text{Rb}$ . Das System wird durch eine Sechs-Niveau-Lindblad-Gleichung beschrieben, um die Leistungsfähigkeit des angedachten Auslese-Verfahren abzuschätzen. Es ergibt sich rechnerische eine maximale Visibility von 0.983. Für die experimentelle Umsetzung

des Auslese-Schemas wird die Verschränkung zwischen dem Polarisationszustand eines spontan emittierten Photons und der Zeeman-Zustand des Atoms verwendet. Durch die Messung der Polarisation wird das Atom in eine beliebige Superposition der Zeeman-Grundzustände projiziert. Eine vollständige Tomographie des Atom-Photon-Zustandes ergibt eine Fidelity von  $0.95 \pm 0.03$ .

Wenn man die erzielten Ergebnisse mit der Detektion der Ionisationsfragmente unter Verwendung von channel electron multipliers kombiniert, kann eine Gesamtdetektionszeit von unter  $1 \mu\text{s}$  realisiert werden. In Kombination mit dem entanglement swapping Protokoll scheint ein beweiskräftiger Test der Bellschen Ungleichung durchführbar, bei dem lokale Wechselwirkung ausgeschlossen werden kann und die hohe Auslese-Genauigkeit bedarf keiner weiteren Annahmen.

# Abstract

Entanglement is, according to E. Schrödinger, the most fundamental trait of quantum mechanics. On the one hand an entangled state of two spin- $\frac{1}{2}$  particles lives on a four dimensional Hilbert space and the theoretical concept describing the state is well understood. On the other hand, the experimental realization of entangled systems, especially hybrid light-matter systems and its analysis, are still a challenging task. Here, starting with a quantum system consisting of an entangled atom-photon pair, the experimental realization of the entanglement swapping protocol is used to build a basic node for a quantum repeater link, consisting of two entangled atoms. The heralded generation of entanglement between the two atoms paves the way towards a conclusive experiment to falsify a local-realistic description of reality. One key ingredient for such experiments is the fast and reliable read-out of the atomic state of  $^{87}\text{Rb}$ .

This thesis describes the method and experiments for quantum state analysis of a single  $^{87}\text{Rb}$  atom using photo-ionization. The ionization scheme is based on a two photon absorption process. The first photon is resonant to either the  $D_1$ - or  $D_2$ -line of  $^{87}\text{Rb}$  while the second photon has a sufficiently small wavelength to ionize the excited and only the excited state. In a first step, the influence of the ionization laser on the atomic levels and the corresponding line width are investigated. Theoretical considerations based on time-dependent perturbation theory seem to be capable of explaining the observed shift in the atomic resonance levels when compared to the experimental results. The line width of the atomic resonances is broadened by the ionization light. This can be explained by numerically solving the Lindblad equation for the atomic system and good agreement can be seen.

The main subject of this thesis is the read-out of general Zeeman states, i.e. superpositions of the degenerate  $5^2S_{1/2}, |F = 1\rangle$  manifold of  $^{87}\text{Rb}$ . To estimate the performance of the considered read-out, the system is modeled by a six level Lindblad equation and a maximal expected visibility of 0.983 is obtained. For the experimental implementation of the read-out procedure entanglement between the polarization state of a spontaneously emitted photon and the Zeeman state of the atom is utilized. By measuring the polarization, the atom is projected into any arbitrary superposition of Zeeman ground states and a full tomography of the atom-photon state yields a fidelity of  $0.95 \pm 0.03$ .

Combining the obtained results with the detection of the ionization fragments using channel electron multipliers an overall detection time well below  $1\mu s$  can be realized. Then, together with the entanglement swapping protocol, a conclusive test of Bell's inequality will be feasible, where local interaction can be excluded and the high detection fidelity does no longer require any additional assumptions.

# Contents

<b>1</b>	<b>Basic concepts</b>	<b>1</b>
1.1	Entanglement . . . . .	1
1.1.1	The Quantum Mechanical Qubit . . . . .	1
1.1.2	Multi-particle states . . . . .	3
	Bell states . . . . .	3
1.1.3	Atom-photon entanglement . . . . .	6
1.1.4	Atom-atom entanglement . . . . .	7
1.1.5	Einstein-Podolski-Rosen-Paradox and Bell's inequality . . . . .	8
	Experimental challenges . . . . .	10
	Detection loophole . . . . .	10
	Locality loophole . . . . .	10
	Proposed experiment to test Bell's inequality . . . . .	11
1.2	Ionization . . . . .	12
1.3	Summary . . . . .	13
<b>2</b>	<b>Experimental Setup and Methods</b>	<b>15</b>
2.1	Laser system . . . . .	15
	Ionization laser . . . . .	17
2.2	Vacuum setup . . . . .	17
2.3	Trapping atoms . . . . .	18
2.3.1	Magneto-optical trap . . . . .	18
2.3.2	Optical dipole trap . . . . .	20
	Detection of atoms . . . . .	20
	Measurement of trapping time . . . . .	22
	Determination of the trapping potential . . . . .	23
<b>3</b>	<b>ac-Stark Shift</b>	<b>25</b>
3.1	The interaction Hamiltonian . . . . .	25
3.1.1	Time-dependent perturbation theory . . . . .	27
	Interaction picture . . . . .	27
	Dyson series . . . . .	28

	Slowly turning on the perturbation . . . . .	29
	Harmonic perturbation . . . . .	30
3.1.2	Light shift in $^{87}\text{Rb}$ . . . . .	31
3.2	Measurements of the Light Shift . . . . .	37
3.2.1	Experimental Sequence . . . . .	38
3.2.2	Measurements of the Ionization Probability Depending on the Laser Frequency . . . . .	39
3.2.3	Dependency of the Light Shift for Increasing Ionization Rates	41
3.2.4	Summary . . . . .	42
<b>4</b>	<b>High Fidelity Read-Out</b>	<b>43</b>
4.1	Hyperfine State Ionization . . . . .	44
4.1.1	Two-Level System . . . . .	44
4.1.2	Three-Level System . . . . .	45
	Experimental sequence . . . . .	50
	Summary . . . . .	51
4.2	Zeeman State Ionization . . . . .	51
4.2.1	Calculations . . . . .	52
4.2.2	Measurements . . . . .	53
4.3	Verification of Atom-Photon Entanglement . . . . .	56
4.3.1	Atom-Photon Correlations . . . . .	56
4.3.2	State Tomography . . . . .	58
	Density matrix . . . . .	58
4.4	Summary . . . . .	64
<b>5</b>	<b>Summary and Outlook</b>	<b>65</b>
5.1	Combining Zeeman state ionization and CEMs . . . . .	66
5.2	Estimations on Loophole-free Test of Bell's Inequality . . . . .	66
5.3	Recent Progress . . . . .	68
<b>A</b>	<b>Data tables</b>	<b>69</b>
<b>B</b>	<b>Six-Level system</b>	<b>71</b>
<b>C</b>	<b>Pulse Sequence</b>	<b>75</b>
<b>D</b>	<b>ac-Stark shift calculated values</b>	<b>77</b>
	<b>Bibliography</b>	<b>81</b>



# Chapter 1

## Basic concepts

The subject of this thesis is the implementation of a new, fast and efficient read-out scheme of the Zeeman state of a single  $^{87}\text{Rb}$  atom based on photo-ionization. For the preparation of the Zeeman states, entanglement between the spin of the atom and the polarization state of a spontaneously emitted photon is utilized. The obtained results are embedded into an experiment for generating entanglement of two macroscopically separated atoms for a test of Bell's inequality without relying on the fair sampling assumption and excluding any local interaction. Therefore, the following chapter gives a short introduction of the concept of qubits and entanglement. Characteristic features of entangled quantum states lead to the Einstein-Podolski-Rosen paradox and Bell's inequality which are reviewed here and also several applications of entanglement will be shown. The second part of this chapter describes the process of ionization and how it can be used for the read-out of an atomic Zeeman state.

### 1.1 Entanglement

#### 1.1.1 The Quantum Mechanical Qubit

A classical two-state system is always in one of the two well-defined states “ $\uparrow$ ” or “ $\downarrow$ ”, while a quantum mechanical spin- $\frac{1}{2}$  system (qubit) can be in a coherent superposition of the two corresponding quantum states  $|\uparrow\rangle$  and  $|\downarrow\rangle$ ,

$$|\Psi\rangle = \alpha |\uparrow\rangle + \beta |\downarrow\rangle \quad (1.1)$$

with  $\{\alpha, \beta\} \in \mathbb{C}$ .  $|\Psi\rangle$  needs to be normalized, such that  $|\alpha|^2 + |\beta|^2 = 1$ . For better visualization one can re-write the qubit state as

$$|\Psi\rangle = \cos \frac{\theta}{2} |\uparrow\rangle_z + e^{i\phi} \sin \frac{\theta}{2} |\downarrow\rangle_z. \quad (1.2)$$

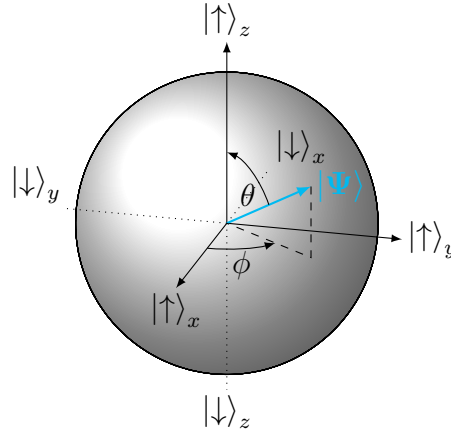


**Figure 1.1:** The surface of the Bloch sphere represents pure states like (1.2) fully determined by the spherical angles  $\theta$  and  $\phi$ .

Here  $\theta$  is the polar angle, while  $\phi$  is the azimuthal angle in spherical coordinates. These two angles allow to represent every qubit state (1.2) by a point on the surface of the Bloch sphere as shown in fig. 1.1.

By analogy, every quantum mechanical two-level system can be represented by such a qubit state. In these systems the “spin orientation” along a given axis  $\vec{a}$  are given by the corresponding basis vectors  $|\uparrow\rangle_{\vec{a}}$  and  $|\downarrow\rangle_{\vec{a}}$  by the respective degree of freedom. Some examples are experimentally realized in the polarization of photons or for two states of an atom. In this thesis, the atomic qubit will be encoded in the Zeeman-spin state of the  $5^2S_{1/2}, |F = 1\rangle$  of  $^{87}\text{Rb}$ , while the photonic qubit is encoded in the polarization state of a spontaneously emitted photon.

Performing a measurement on a quantum system in the state  $|\Psi\rangle$  with the Hermitian operator  $\hat{\mathcal{A}}$ , the system is projected onto an eigenstate of  $\hat{\mathcal{A}}$ . The result of a measurement yields the corresponding eigenvalues  $\lambda_{\hat{\mathcal{A}}}$  while the expectation value of  $\hat{\mathcal{A}}$  is given by

$$\langle \hat{\mathcal{A}} \rangle = \langle \Psi | \hat{\mathcal{A}} | \Psi \rangle. \quad (1.3)$$

For spin- $\frac{1}{2}$  systems the Pauli matrices

$$\hat{\sigma}_x = \begin{pmatrix} 0 & 1 \\ 1 & 0 \end{pmatrix}, \quad \hat{\sigma}_y = \begin{pmatrix} 0 & -i \\ i & 0 \end{pmatrix}, \quad \hat{\sigma}_z = \begin{pmatrix} 1 & 0 \\ 0 & -1 \end{pmatrix}, \quad \hat{\sigma}_0 = \begin{pmatrix} 1 & 0 \\ 0 & 1 \end{pmatrix} \quad (1.4)$$

span the space of observables together with the identity  $\hat{\sigma}_0 = \mathbb{1}$ . The corresponding eigenvectors of  $\hat{\sigma}_x$  and  $\hat{\sigma}_y$  can be decomposed in the eigenstates of  $\hat{\sigma}_z$  ( $|\uparrow\rangle_z$  and  $|\downarrow\rangle_z$ )

as

$$|\uparrow\rangle_x = \frac{1}{\sqrt{2}} (|\downarrow\rangle_z + |\uparrow\rangle_z) \quad (1.5a)$$

$$|\downarrow\rangle_x = \frac{1}{\sqrt{2}} (|\downarrow\rangle_z - |\uparrow\rangle_z) \quad (1.5b)$$

$$|\uparrow\rangle_y = \frac{1}{\sqrt{2}} (i|\downarrow\rangle_z + |\uparrow\rangle_z) \quad (1.5c)$$

$$|\downarrow\rangle_y = \frac{1}{\sqrt{2}} (|\downarrow\rangle_z + i|\uparrow\rangle_z). \quad (1.5d)$$

For any arbitrarily oriented measurement basis  $\vec{a}$  in  $\mathbb{R}^3$ , the matrix can be written as the scalar product of the unit vector of the basis and the Pauli-matrices

$$\vec{\hat{\sigma}} \cdot \vec{a} = \begin{pmatrix} \hat{\sigma}_x \\ \hat{\sigma}_y \\ \hat{\sigma}_z \end{pmatrix} \cdot \begin{pmatrix} a_x \\ a_y \\ a_z \end{pmatrix} = \begin{pmatrix} a_z & a_x - ia_y \\ a_x + ia_y & -a_z \end{pmatrix} \quad (1.6)$$

One can see from (1.4) that the Pauli matrices do not commute  $[\hat{\sigma}_i, \hat{\sigma}_j] = 2i\epsilon_{ijk}\hat{\sigma}_k$ . Hence a system prepared in an eigenstate of  $\hat{\sigma}_i$  yields maximally random results if measured in a complementary basis  $\hat{\sigma}_{j \neq i}$ .

### 1.1.2 Multi-particle states

A system consisting of more than one particle is called entangled if one can not write its state as the tensor product of states of its constituents

$$|\Psi\rangle \neq |\Psi\rangle_a \otimes |\Psi\rangle_b \otimes \dots \quad (1.7)$$

According to Schrödinger, entanglement is *the* characteristic trait of quantum mechanics [1]. Entangled states can be in a well-defined, pure state, whereas the measurement result on the individual particles is fully random [2].

#### Bell states

If we restrict the system to two qubits the resulting state (1.7) will be defined in a four-dimensional Hilbert space. Besides the standard basis consisting of the product of the single qubit basis states  $|\uparrow\rangle_z, |\downarrow\rangle_z$ , a basis defined by the maximally

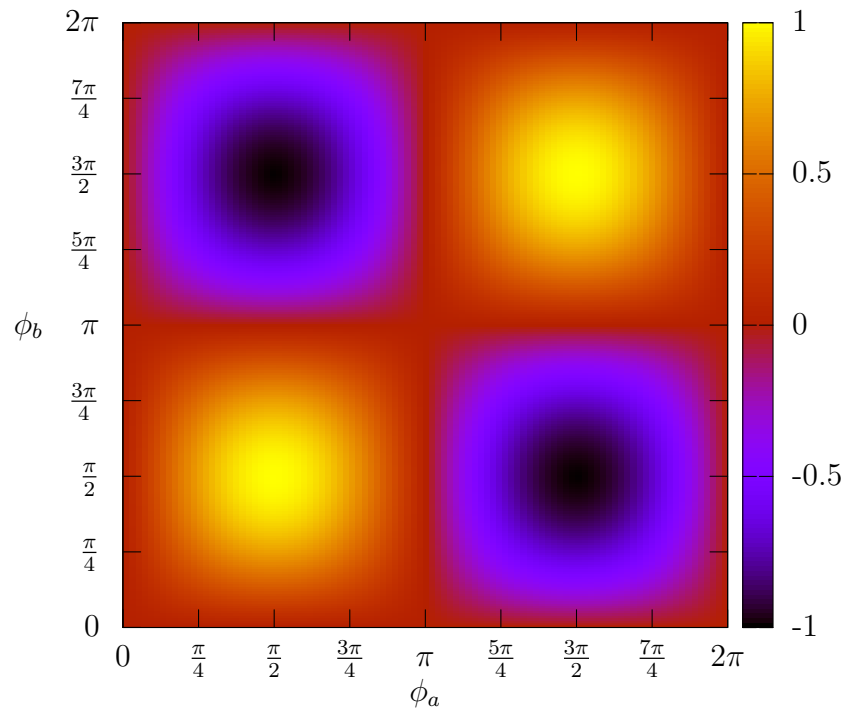


**Figure 1.2:** *Correlations:* The expectation value of a 2-qubit system in the  $|\Psi^+\rangle$  state measured in the equatorial plane ( $\theta_{a,b} = \frac{\pi}{2}$ ). The highest (anti-)correlations occur when both directions are (anti-)parallel and the system is measured in  $\hat{\sigma}_{x,y}$ -direction. this can be seen from (1.10), where the spins are parallel along the  $x$ - and  $y$ -direction. In any intermediate direction the correlation is reduced.

entangled Bell states [3] can be found with

$$|\Psi^-\rangle = \frac{1}{\sqrt{2}} (|\uparrow\rangle_z |\downarrow\rangle_z - |\downarrow\rangle_z |\uparrow\rangle_z) \quad (1.8a)$$

$$|\Psi^+\rangle = \frac{1}{\sqrt{2}} (|\uparrow\rangle_z |\downarrow\rangle_z + |\downarrow\rangle_z |\uparrow\rangle_z) \quad (1.8b)$$

$$|\Phi^-\rangle = \frac{1}{\sqrt{2}} (|\uparrow\rangle_z |\uparrow\rangle_z - |\downarrow\rangle_z |\downarrow\rangle_z) \quad (1.8c)$$

$$|\Phi^+\rangle = \frac{1}{\sqrt{2}} (|\uparrow\rangle_z |\uparrow\rangle_z + |\downarrow\rangle_z |\downarrow\rangle_z). \quad (1.8d)$$

$|\Psi^-\rangle$  is the antisymmetric singlet state, while the remaining states  $|\Psi^+\rangle$  and  $|\Phi^\pm\rangle$  are the symmetric triplet states. We can transform e.g.  $|\Psi^+\rangle$  into a triplet state in the complementary bases,

$$|\Psi^+\rangle = \frac{1}{\sqrt{2}} (|\uparrow\rangle_x |\uparrow\rangle_x + |\downarrow\rangle_x |\downarrow\rangle_x) \quad (1.9)$$

$$= \frac{1}{\sqrt{2}} (|\downarrow\rangle_y |\downarrow\rangle_y - |\uparrow\rangle_y |\uparrow\rangle_y). \quad (1.10)$$

One can not find a basis in which an entangled state can be separated and we get a maximally random outcome if the measurement bases are conjugate, e.g. for  $\hat{x}$  and  $\hat{z}$ . This can be understood if we calculate the expectation value of a joined measurement performed on both constituents [4]. The quantum state  $|\Psi^+\rangle$  is measured by Alice (Bob) in the direction  $\vec{a}$  ( $\vec{b}$ ). By using (1.6) the Pauli operator in direction  $\vec{a}$  is given by

$$\hat{\sigma}_a = \begin{pmatrix} \cos \theta_a & e^{-i\phi_a} \sin \theta_a \\ e^{i\phi_a} \sin \theta_a & -\cos \theta_a \end{pmatrix} \quad (1.11)$$

and for a joined measurement we get

$$\begin{aligned} \hat{\sigma}_a \otimes \hat{\sigma}_b &= \begin{pmatrix} \cos \theta_a & e^{-i\phi_a} \sin \theta_a \\ e^{i\phi_a} \sin \theta_a & -\cos \theta_a \end{pmatrix} \otimes \begin{pmatrix} \cos \theta_b & e^{-i\phi_b} \sin \theta_b \\ e^{i\phi_b} \sin \theta_b & -\cos \theta_b \end{pmatrix} = \quad (1.12) \\ &= \begin{pmatrix} \cos \theta_a \cos \theta_b & e^{-i\phi_b} \cos \theta_a \sin \theta_b & e^{-i\phi_a} \cos \theta_b \sin \theta_a & e^{-i(\phi_a+\phi_b)} \sin \theta_a \sin \theta_b \\ e^{i\phi_b} \cos \theta_a \sin \theta_b & -\cos \theta_a \cos \theta_b & e^{-i(\phi_a-\phi_b)} \sin \theta_a \sin \theta_b & -e^{-i\phi_a} \cos \theta_b \sin \theta_a \\ e^{i\phi_a} \cos \theta_b \sin \theta_a & e^{i(\phi_a-\phi_b)} \sin \theta_a \sin \theta_b & -\cos \theta_a \cos \theta_b & -e^{-i\phi_b} \cos \theta_a \sin \theta_b \\ e^{i(\phi_a+\phi_b)} \sin \theta_a \sin \theta_b & -e^{i\phi_a} \cos \theta_b \sin \theta_a & -e^{i\phi_b} \cos \theta_a \sin \theta_b & \cos \theta_a \cos \theta_b \end{pmatrix}. \quad (1.13) \end{aligned}$$

The expectation value can be calculated as in (1.3) and is given by

$$\begin{aligned}\langle \hat{\sigma}_a \otimes \hat{\sigma}_b \rangle &= \langle \Psi^+ | \hat{\sigma}_a \otimes \hat{\sigma}_b | \Psi^+ \rangle \\ &= \sin \theta_a \sin \theta_b \cos(\phi_a - \phi_b) - \cos \theta_a \cos \theta_b.\end{aligned}\quad (1.14)$$

The calculated expectation value for a 2-qubit system can be tested experimentally by measuring the correlations of the outcome of the measurements on Alice's (along  $\vec{a}$ ) and Bob's (along  $\vec{b}$ ) side and we get after  $N$  trials

$$\langle \hat{\sigma}_a \otimes \hat{\sigma}_b \rangle = \frac{1}{N} \left( N_{\uparrow\uparrow}^{\vec{a},\vec{b}} + N_{\downarrow\downarrow}^{\vec{a},\vec{b}} - N_{\downarrow\uparrow}^{\vec{a},\vec{b}} - N_{\uparrow\downarrow}^{\vec{a},\vec{b}} \right) \quad (1.15)$$

which converges to (1.14) for large numbers [5]. Here  $N$  is the number of performed measurements, while, e.g.  $N_{\uparrow\downarrow}^{\vec{a},\vec{b}}$ , is the number of events where Alice measured  $|\uparrow\rangle$  along the direction  $\vec{a}$  and Bob measured  $|\downarrow\rangle$  along  $\vec{b}$ . It can be seen in fig. 1.2 that if the measurement basis do coincide, perfect correlations can be observed. These correlations are experimentally limited by the visibility, i.e. the contrast of the interference fringes

$$v = \frac{v_{max} - v_{min}}{v_{max} + v_{min}}. \quad (1.16)$$

In (1.15) we assume that all particles are detected. If this is not the case,  $N$  is substituted by the number of detected coincidences

$$N_{det} = N_{\uparrow\uparrow}^{\vec{a},\vec{b}} + N_{\downarrow\downarrow}^{\vec{a},\vec{b}} + N_{\downarrow\uparrow}^{\vec{a},\vec{b}} + N_{\uparrow\downarrow}^{\vec{a},\vec{b}}. \quad (1.17)$$

By performing a measurement on one particle, the other system is projected into the corresponding state. This can be utilized for the preparation of Bob's state by choosing the appropriate measurement bases on Alice's side. In our setup we will use this scheme for the preparation of general Zeeman states, i.e. superpositions of the degenerate  $5^2S_{1/2}, |F=1\rangle$  manifold of  $^{87}\text{Rb}$ .

### 1.1.3 Atom-photon entanglement

In our experiment we use entanglement between the polarization state of a photon and the spin state of a  $^{87}\text{Rb}$  atom. The atom is excited into the  $5^2P_{3/2}, |F'=0, m_F=0\rangle$  state with a short optical pulse. This excited state spontaneously decays into the Zeeman manifold of the  $5^2S_{1/2}, |F=1\rangle$  ground state with the magnetic quantum numbers  $m_F = \{\pm 1, 0\}$ , represented by the state  $|F=1, m_F = \{\pm 1, 0\}\rangle$ , by emitting a  $\sigma^\mp$ - or  $\pi$ -polarized photon, depicted by  $|\sigma^\pm, \pi\rangle$ . In our setup the  $\pi$ -polarized photons do not couple into the single mode fiber which defines the quantization axis of the system and are therefore not detected [6]. As the decay

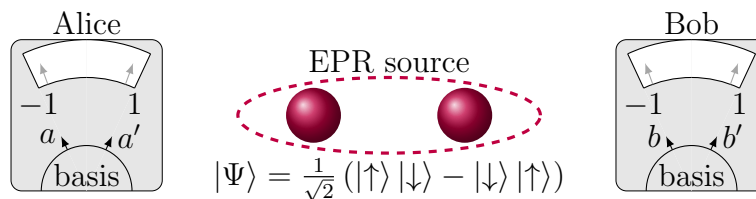


**Figure 1.3:** *Experimental setup to test Bell's inequality:* An EPR source generates entangled particles in the state  $|\Psi^-\rangle$ . These particles are transmitted to the two measurement apparatuses Alice (A) and Bob (B) where spin measurements along the directions  $a, a', b, b'$  are performed with the possible outcomes  $\pm 1$ .

channels are indistinguishable in all degrees of freedom except their polarization, the entangled atom-photon state reads as

$$|\Psi\rangle_{AP} = \frac{1}{\sqrt{2}} (|1, -1\rangle |\sigma^+\rangle + |1, 1\rangle |\sigma^-\rangle) \quad (1.18)$$

$$= \frac{1}{\sqrt{2}} (|\downarrow\rangle_z |\uparrow\rangle_z + |\uparrow\rangle_z |\downarrow\rangle_z) \quad (1.19)$$

By measuring the polarization of the photon along freely chosen directions, the atom is projected into different corresponding spin states [7]. As one can see in fig. 1.2 the probability to find an atom in the state, e.g.  $|\uparrow\rangle_x$  is one conditioned on the measured polarization state of the photon as  $|\uparrow\rangle_x$ . This fact will be utilized for the preparation of Zeeman superposition states and the prepared states will then be read-out via two-photon photo-ionization (see fig. 4.6).

#### 1.1.4 Atom-atom entanglement

For the heralded generation of entanglement of two atoms that are separated by a macroscopic distance, one can use the entanglement swapping protocol [8]. In this scheme two entangled atom-photon pairs are used. The photons are guided to a Bell state measurement apparatus [9] where they interfere. By measuring the spacial and polarization state the photons are projected onto Bell states  $|\Psi^\pm\rangle$  based on the Hong-Ou-Mandel effect [10, 11]. The generation of atom-atom entanglement is heralded by a coincident detection of two photons.

### 1.1.5 Einstein-Podolski-Rosen-Paradox and Bell's inequality

The question whether the description of nature given by quantum mechanics is complete or not was discussed controversially from the beginning of quantum mechanics until the present. Einstein, Podolski and Rosen claimed in their famous paper "*Can quantum-mechanical description of physical reality be considered complete ?*" [12] that any physical theory should be complete, real, and local. In their words this means that every element of the physical reality must have a counterpart in the physical theory to be *complete*. They grant a theory to be *real* if, without in any way disturbing a system, we can predict with certainty (i.e. with probability equal to unity) the value of a physical quantity, then there exists an element of physical reality corresponding to this physical quantity. The word *local* means in their context that the real factual situation of the system  $S_2$  (i.e. *Bob*) is independent of what is done with the system  $S_1$  (i.e. *Alice*), which is spatially separated from the former [13].

According to the authors, this is not fulfilled by quantum mechanics. The answer to this question was a rather philosophical as the proposed gedankenexperiment was based on the continuous variables position  $\hat{x}$  and momentum  $\hat{p}_x$  dealing with infinite dimensions of the corresponding Hilbert spaces and any experimental test was impracticable at that time.

Based on the assumptions made by Einstein, Bohm simplified the problem to a decaying spin-0 system resulting in an spin- $\frac{1}{2}$  singlet state  $|\Psi^-\rangle$  consisting of two particles [14]. For this system Bell derived an inequality, where predictions made by any local-realistic theory differ from those of quantum mechanics [15, 16].

Bell considered the source proposed by Bohm as shown in fig. 1.3 emitting particle pairs in the singlet state  $|\Psi^-\rangle$  towards two measurement devices one each on Alice's and one on Bob's side. Each of them performs measurements in two bases  $a$  and  $a'$  for Alice and  $b$  and  $b'$  for Bob respectively. The possible measurement outcomes for each measurement are the states  $|\uparrow\rangle_k$  and  $|\downarrow\rangle_k$  with  $k \in \{a, a', b, b'\}$  to which we assign the values  $\pm 1$ . If we want to describe the setup of fig. 1.3 in a local realistic model, each measurement outcome is determined by a set of local variables  $\lambda$ . The probabilistic measurement results are caused by an unknown statistical (and experimentally inaccessible) distribution  $p(\lambda)$ , therefore  $\lambda$  is also referred to as local *hidden* variable (LHV). Every single measurement outcome is described by the observable  $A_a(\lambda) = \pm 1$  and  $B_b(\lambda) = \pm 1$ , determined only by the value of  $\lambda$  and the locally chosen orientation  $a, a', b, b'$ . This means that the outcome of a measurement is independent of the measurement apparatus in use. The observables do not depend on any variable of the opposite party, hence locality is preserved. The expectation

value for a joined measurement of  $A_a$  and  $B_b$  can be written as

$$E(a, b) = \int_{\Lambda} A_a(\lambda) B_b(\lambda) p(\lambda) d\lambda$$

and for different analyzer settings  $a'$  and  $b'$  it can be shown that

$$\begin{aligned} E(a, b) - E(a, b') &= \int_{\Lambda} A_a(\lambda) B_b(\lambda) [1 \pm A_{a'}(\lambda) B_{b'}(\lambda)] p(\lambda) d\lambda - \\ &\int_{\Lambda} A_a(\lambda) B_{b'}(\lambda) [1 \pm A_{a'}(\lambda) B_b(\lambda)] p(\lambda) d\lambda. \end{aligned} \quad (1.20)$$

As the possible outcomes are bound by 1, i.e.  $|A_a(\lambda)| \leq 1 \geq |B_b(\lambda)|$  the absolute value  $|E(a, b) - E(a, b')|$  is also bound by

$$|E(a, b) - E(a, b')| \leq \int_{\Lambda} [1 \pm A_{a'}(\lambda) B_{b'}(\lambda)] p(\lambda) d\lambda + \int_{\Lambda} [1 \pm A_{a'}(\lambda) B_b(\lambda)] p(\lambda) d\lambda$$

which yields the bound

$$S(a, a', b, b') = |E(a, b) - E(a, b')| + |E(a', b) + E(a', b')| \leq 2 \quad (1.21)$$

for local realistic theories [17].

We can calculate the expectation value predicted by quantum mechanics for the  $|\Psi^-\rangle$  state and measurement directions  $\vec{a}$ ,  $\vec{b}$  with the operator  $\hat{\mathcal{A}} = \hat{\sigma} \cdot \vec{a}$  and  $\hat{\mathcal{B}} = \hat{\sigma} \cdot \vec{b}$  as

$$E_{qm}(a, b) = \langle \hat{\mathcal{A}} \cdot \hat{\mathcal{B}} \rangle = \langle \Psi^- | \hat{\sigma}_a \otimes \hat{\sigma}_b | \Psi^- \rangle = -\vec{a} \cdot \vec{b}$$

similar to eq. (1.15). If we choose the vectors  $a, a', b, b'$  to lie in the equatorial plane of the Bloch sphere (see fig. 1.2) and the included angles  $\angle(a, b) = \angle(b, a') = \angle(a', b') = 45^\circ$  one possible set of vectors is

$$\vec{a} = \begin{pmatrix} \sin 0^\circ \\ \cos 0^\circ \\ 0 \end{pmatrix}, \vec{a}' = \begin{pmatrix} \sin 90^\circ \\ \cos 90^\circ \\ 0 \end{pmatrix}, \vec{b} = \begin{pmatrix} \sin 45^\circ \\ \cos 45^\circ \\ 0 \end{pmatrix}, \vec{b}' = \begin{pmatrix} \sin 135^\circ \\ \cos 135^\circ \\ 0 \end{pmatrix}. \quad (1.22)$$

Inserting the values in (1.14) with  $\theta_{a, a', b, b'} = \frac{\pi}{2}$  and

$$\phi_a = 0, \quad \phi_{a'} = \frac{\pi}{2}, \quad \phi_b = \frac{\pi}{4}, \quad \phi_{b'} = \frac{3\pi}{4}$$

these vectors result in a parameter  $S_{qm}$  for the CHSH-inequality as

$$S_{qm}(a, a', b, b') = 2\sqrt{2} > 2. \quad (1.23)$$

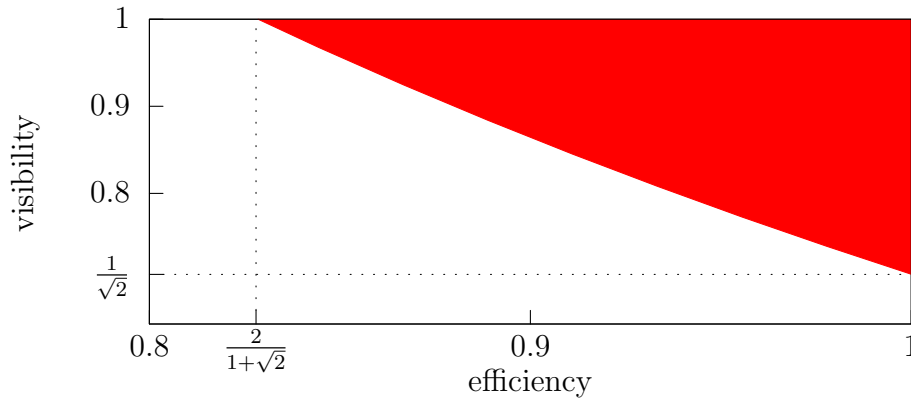


**Figure 1.4:** *Detection efficiency and visibility required for a loophole free test of Bell's inequality:* For closing the detection loophole the efficiency  $\eta$  and the visibility  $v$  of the experiment must lie in the red shaded area limited by (1.24).

Bell paved the way to distinguish experimentally between a local realistic world claimed by Einstein, Podolski and Rosen or a non-local/non-realistic world.

### Experimental challenges

Until now all experiments [11, 18–26] testing Bell's inequality (1.21) indicate that a local-realistic description of nature seems not to be possible. However, all these experiments failed to exclude all local-realistic theories due to experimental shortcomings, and additional assumptions had to be made. This gives rise to loopholes so that a local realistic description is still possible. The two most prominent loopholes are the following:

**Detection loophole** It can be shown [27–29] that the detection efficiency  $\eta$ , defined as the ratio of detected and generated pairs  $\eta = N_{det}/N$  with  $N_{det}$  defined in (1.17) and the visibility (1.16) both must fulfill

$$\eta \left( 1 + v\sqrt{2} \right) > 2. \quad (1.24)$$

to exclude all LHV theories. To be able to reject the assumption that the detected sample behaviors equally to the entire sample, the experimental parameters must lie inside the area shaded in red in fig. 1.4.

**Locality loophole** A fundamental request of Einstein was the independence of the measurement processes performed by Alice and Bob. If one assumes that no

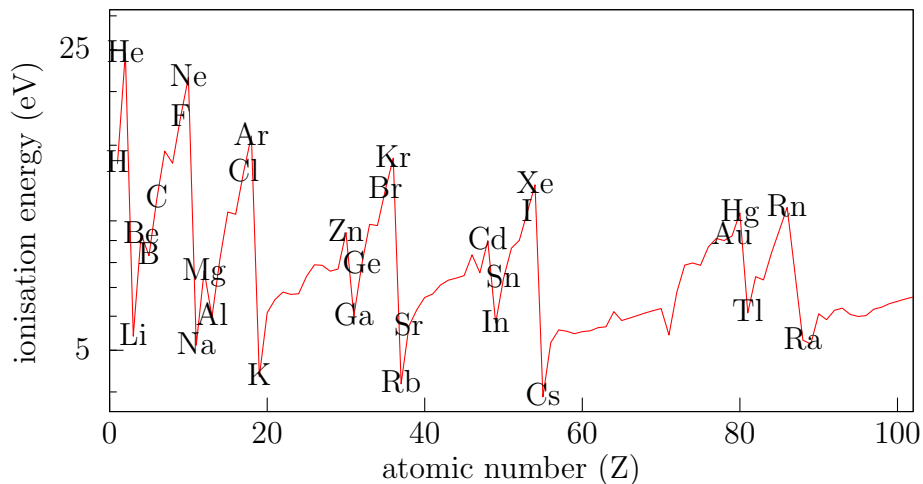


**Figure 1.5:** The ionization energy required to remove the first outermost electron from the atom depending on the atomic number [33].

interaction faster than the speed of light is possible, the two measurement events have to be space-like separated with respect to the required measurement time  $\tau_{meas} < c \cdot |\vec{x}_1 - \vec{x}_2|$  to perform a measurement.

### Proposed experiment to test Bell's inequality

Until now almost all experiments were in favor of quantum mechanics but a conclusive test closing all loopholes is still unsettled [8, 30, 31]. Only for photons both loopholes could be closed [21, 25, 26] but not as required within a single experiment. The main challenge in all these experiments is the implementation of a detection setup that is fast and efficient. For this purpose an experimental setup is designed in an "event-ready" scheme [8] to generate entanglement of two atoms separated by a macroscopic distance to close the detection loophole. To exclude any local interaction, a read-out scheme based on photo-ionization is implemented and described in this thesis. The ionization fragments are detected with high efficiency to ensure that the experiment lies inside the parameter space bounded by (1.24). This is realized by using channel electron multipliers (CEM) and are described in detail in [32]. The time to determine the state of the atom  $t_{meas} < 1 \mu s$  and a separation of the two measurement apparatuses of 300 m is required.

## 1.2 Ionization

The read-out scheme of an  $^{87}\text{Rb}$  atom presented in this thesis is based on *photo-ionization*. The basic concept of photo-ionization, i.e. the removal of an electron by absorbing one or several photons is explained in the following.

The process of ionization was first observed by Hertz, Hallwachs and Lennard [34–36] and explained by Einstein [37]. The photoelectric effect leveraged the quantum theory of light proposed by Planck [38].

The energy of the incident photon  $E_{ph} = \hbar\omega$  must exceed the binding energy  $E_i$  of the most weakly bound electron. If the photon gets absorbed by the atom an electron with the kinetic energy  $E_{kin} = E_{ph} - E_i$  is released. Therefore photons with insufficient energy can not ionize an atom. The energy required strongly depends on the atomic number  $Z$  as shown in fig. 1.5. The ionization rate, i.e. the number of ionization events per time, can be described by the transition rate

$$\Gamma_{ion} = \sigma_{ph}(\omega)\Phi \quad (1.25)$$

with  $\Phi = I_{ph}/\hbar\omega_{ph}$  being the photon flux density, i.e. the number of photons traveling through a unit area per second.  $\sigma_{ph}(\omega)$  is the scattering cross section of the considered atomic state. A detailed discussion of its calculation can be found in [39–41]. One can see from (1.25) that the speed of the ionization process is proportional to the intensity of the ionization light. The ionization cross section of the  $5P$  excited states for various wavelengths are given in tab. A.4 [42].

The required ionization energy can be made up of several photons leading to multi-photon ionization [43]. With the use of two photons, the energy per photon can be reduced, e.g. the ionization energy of the ground state of  $^{87}\text{Rb}$  is 4.2 eV, while the ionization energy of the excited state  $5P$  is 2.6 eV corresponding to a wavelength shorter than  $\lambda = 295.2$  nm and  $\lambda = 473.22$  nm respectively. In this thesis a two photon transition is utilized for the read-out of the Zeeman spin state of a  $^{87}\text{Rb}$  atom. The first photon is resonant to the  $5^2S_{1/2}, F = 1 \rightarrow 5^2P_{1/2}, F' = 1$  transition, while the second photon has a wavelength of 450 nm corresponding to an energy of 2.76 eV sufficient to remove the valence electron. By varying the polarization of the first photon, the selection rules for electric dipole transitions define which Zeeman state of the joined atom-photon state (1.19) gets excited and ionized. This provides a method to ionize arbitrary coherent superpositions of atomic substates.

In the proposed experiment for a loophole-free test of Bell's inequality, the released electron and ion will be accelerated towards channel electron multipliers generating a macroscopic current [31, 32, 44]. By using higher intensities of the ionization light, the ionization process can be speed up and the measurement time can be reduced below 1  $\mu\text{s}$ . In combination with the CEMs the read-out can be fast and

efficient enough for a test of Bell's inequality without relying on the fair sampling assumption and excluding local interactions.

## 1.3 Summary

This chapter gave a short introduction of the concept of entanglement and its logical consequences. The derivation of Bell's inequality suggests that a local realistic description of the physical reality does not seem to be possible. Nevertheless, this statement has been waiting to be tested experimentally for nearly the last 50 years. To perform such an experiment two entangled atom-photon pairs are aimed to be used and entanglement between the two atoms is generated in a heralded way by the entanglement swapping protocol. The read-out of the atomic spin states can be done by two-photon ionization and the ionization fragments will be detected by channel electron multipliers. The experimental realization of a sub- $\mu\text{s}$  atomic state read-out is the main subject of this thesis and a key ingredient towards a conclusive test of Bell's inequality.



# Chapter 2

## Experimental Setup and Methods

In this chapter the general setup of the experiment is described. For performing experiments with a single atom, the atom has to be isolated from the environment and has to be well localized. Further requirements are the ability to observe the atom efficiently and to control the internal degrees of freedom of the atom. For this purpose the setup consists of three main building blocks namely the laser system, the vacuum chamber and the trap formed by a magneto-optical trap and the optical dipole trap. These parts will be explained in the following.

### 2.1 Laser system

The laser system of the experiment is based on five diode lasers. Three of them are optically stabilized by means of feedback from a diffraction grating in Littrow configuration [45]. Via saturation spectroscopy in a Rubidium gas cell, we stabilize the frequency to atomic resonance lines. The three lasers and the resulting frequencies are shown in fig. 2.1 and in the course of this thesis we will refer to the nomenclature used therein. The temperature of the diodes is stabilized with thermo-electric elements and commercial controller electronics. With acousto-optical modulators (AOMs) the frequency can be additionally shifted in a range of  $\pm 300$  MHz. The intensity can also be switched within  $\sim 10$  ns. By using the AOMs in double pass arrangement, a switching ratio of more than 100 dB is achieved to suppress any light leakage. The intensity of the cooling and repump light is stabilized by a PID-controller [46]. The remaining short-term frequency fluctuations are about 700 kHz arising from phase noise of the diode and 2 MHz on the longer time scale [7]. A further diode laser is used at a wavelength of 856 nm to generate the potential for the optical dipole trap. The light is switched by an AOM and stabilized for slow variations  $< 1$  kHz with a photo diode and a PID-controller as shown in fig. 2.2.

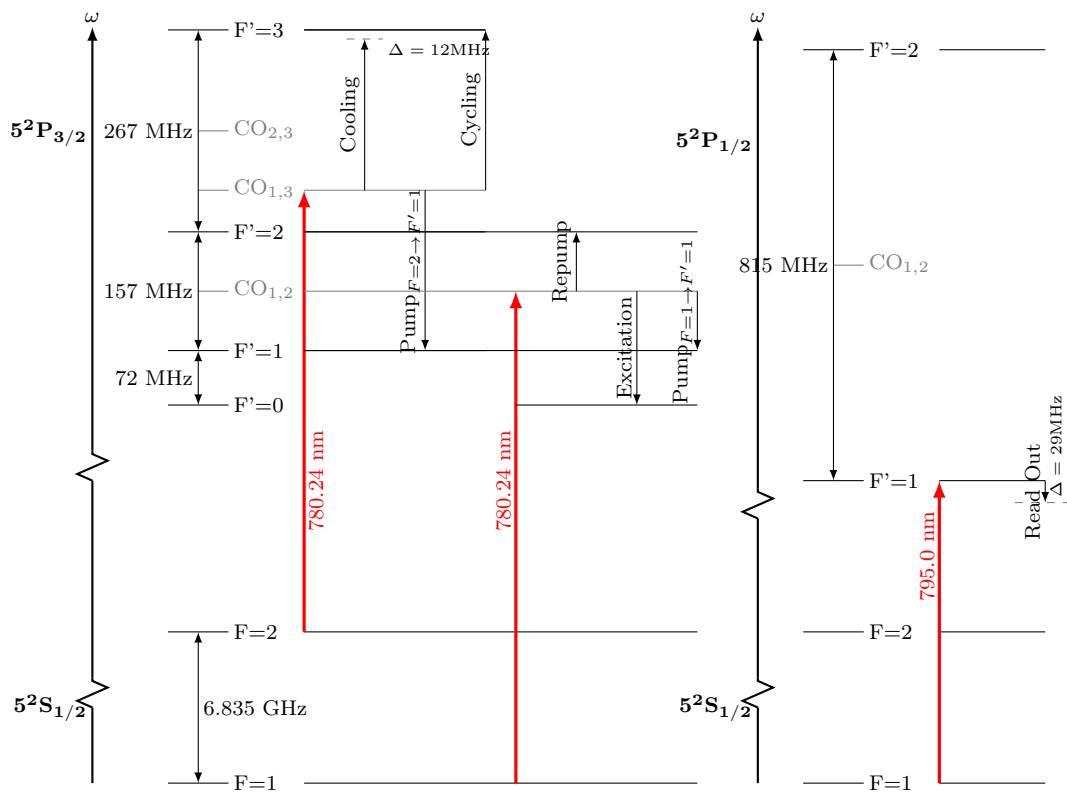


**Figure 2.1:** Laser system in use

**Ionization laser** The fast ionization of a  $^{87}\text{Rb}$  atom is done by utilizing a two-photon transition, where the first photon is resonant to the  $D_1$ - or  $D_2$ -line of  $^{87}\text{Rb}$  respectively, and the second one has a wavelength shorter than  $\lambda_{ion} < 473.2$  nm. The time needed to ionize the atom depends on the intensity of the ionization light and hence a high intensity is desired. As a first step, the spacial mode is purified by a single mode fiber and the light is focused on the atom with a microscope objective. As a light source, several systems were tested, but the development still continues and higher intensities might be available in the future.

The first system that came into operation was a diode pumped solid state (DPSS) laser by *Laser Quantum* with an output power of 350 mW. As it is a cw laser the light was switch by an AOM in double pass configuration and coupled into a single mode fiber. With this system we achieved an output power of  $\sim 100$ mW at the position of the atom [32, 44]. Besides the high losses due to the AOM, the request in stabilizing the temperature of the heat sink was challenging and impeded a stable operation. To overcome the losses of the AOM, a laser diode was directly pulsed with a *Picolas LDP-V03-100 UF3* driver module for pulsed lasers. A typical pulse can be seen in fig. 3.4. With a 100 mW *Nichia NDA4116E* single mode laser diode at a wavelength of 450 nm, a coupling efficiency of 0.60 was achieved. As the repetition rate of 15 Hz for the requested pulses is low, we can overdrive this temperature stabilized diode mounted in a standard laser mount by a factor of 4 and achieve output powers at the position of the atom of  $\sim 250$ mW. The advantage of the new system was not only the higher intensity, but also the reduced space requirements, electronics and temperature stabilization.

## 2.2 Vacuum setup

The experimental chamber consists of a glass cell that is attached to the main vacuum chamber and sealed with a 2 mm thick Indium wire to a milled flange [47, 48]. This glass cell allows a very good optical access to the experimental area. The outer dimensions of the cell of 41 mm  $\times$  21 mm  $\times$  120 mm and a thickness of 3 mm are suited to host channel electron multipliers as described in [32, 44, 49, 50]. Two highly reflective layers are coated onto one side of the cell to enable the generation of a retro-reflected magneto-optical trap (see fig. 2.2). The entire vacuum chamber is pumped by an ion getter pump <sup>1</sup> to a pressure of  $\approx 10^{-9}$  mbar. To achieve a certain pressure of Rubidium atoms, dispensers are mounted inside the chamber and heated by a current of  $\approx 2$  A. As the lifetime of the atom inside the trap is mainly limited by collisions with the background gas, a UV-LED *P8D236* by *Seoul Optodevice* is mounted in the proximity of the glass cell to dissociate atoms deposited on the inside of the glass cell. During the loading of the optical dipole

---

<sup>1</sup>Varian, VacIon Plus 20

trap the LED is switched on to increase the pressure of Rb, while the deactivation of the LED after the successful loading increases the lifetime of the atom inside the trap. With this setup, it is possible to hold atoms for a reasonable time of more than 5 s. This is 6 orders of magnitude longer than the time needed for the read-out of the atomic state described in this thesis.

## 2.3 Trapping atoms

To manipulate the quantum state of a single  $^{87}\text{Rb}$  atom it has to be well localized in a defined position. While the interaction with the environment is suppressed by the vacuum chamber, the trapping is done in two steps. The first step is to generate a cloud of laser cooled atoms with a magneto-optical trap. In the second step a single atom is loaded into the conservative potential of an optical dipole trap.

### 2.3.1 Magneto-optical trap

To trap a single  $^{87}\text{Rb}$  atom we start with a magneto-optical trap (MOT) that serves as a reservoir of cold atoms [51–57]. The trap consists of three pairs of circularly polarized beams that are back-reflected into themselves. The two horizontal beams are weakly convergent to compensate for losses while passing through the glass cell several times as shown in fig. 2.2 [47]. This is necessary to achieve balanced beams within each pair of beams at the position of the atom cloud. A birefringent plate is inserted in each incident beam to compensate polarization dependent losses so that a high degree of circular polarization is ensured at the center of the MOT. A third (vertical) beam pair is additionally introduced (see fig. 2.2) to generate cooling and confinement in all three dimensions. The magnetic quadrupole field is generated by two coils in anti-Helmholtz configuration with a field gradient  $\partial_z B$  on the order of  $\sim 10 \text{ G cm}^{-1}$  while operated by a current of up to 2 A [47].

Laser light red-detuned to the  $5^2\text{S}_{1/2} |F = 2\rangle \rightarrow 5^2\text{P}_{3/2} |F' = 3\rangle$  transition by 12 MHz is used to cool the atoms (see fig. 2.1). This transition is suitable as it is closed which means that the atom can only decay from  $5^2\text{P}_{3/2} |F' = 3\rangle$  to the  $|F = 2\rangle$  ground state. To counteract a small fraction of off-resonant excitation to the  $5^2\text{P}_{3/2} |F' = 2\rangle$  state and subsequent decay to the  $|F = 1\rangle$  ground state repump light is admixed to the cooling beams.

Due to the Doppler effect [58], the motion of the atom shifts the atomic resonance frequency so the atoms preferably scatter light coming from the opposite direction of its motion. This leads to an effective loss of kinetic energy [59, 60]. This cooling process is limited by the Doppler temperature for  $^{87}\text{Rb}$  of  $T_D = \frac{\hbar\Gamma}{2k_B} = 146 \text{ } \mu\text{K}$ . A magneto-optical trap makes use of the effect of polarization gradient cooling to cool below the Doppler limit. The Zeeman splitting of the atomic levels in consequence

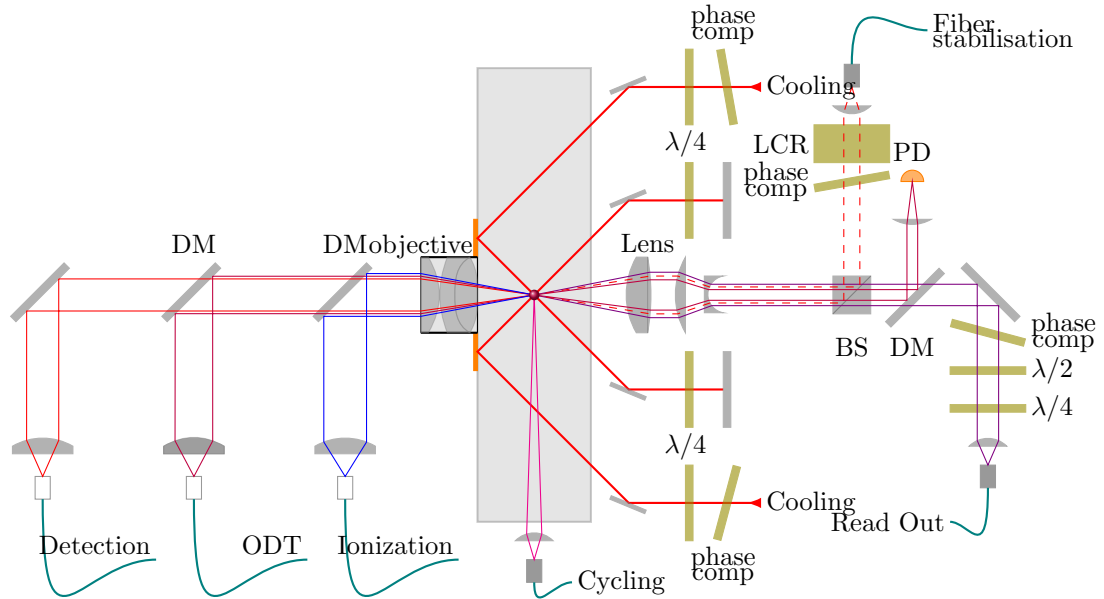


**Figure 2.2:** *Experimental setup:* The atoms are trapped in an optical dipole trap(ODT) generated by a tightly focused laser beam. This beam is overlapped in an confocal microscope arrangement with the detection volume collecting scattered photons into a single mode fiber. To generate a high intensity of ionizing light the ionization beam is also focused via the microscope objective. The excitation, pumping and vertical cooling beams are not shown.

BS - beam splitter, phase comp. - compensation plate for phase shifts, DM - dichroic mirror,  $\lambda/2$ ,  $\lambda/4$  - half and quarter wave plates, LCR - liquid crystal retarder, PD - photo diode

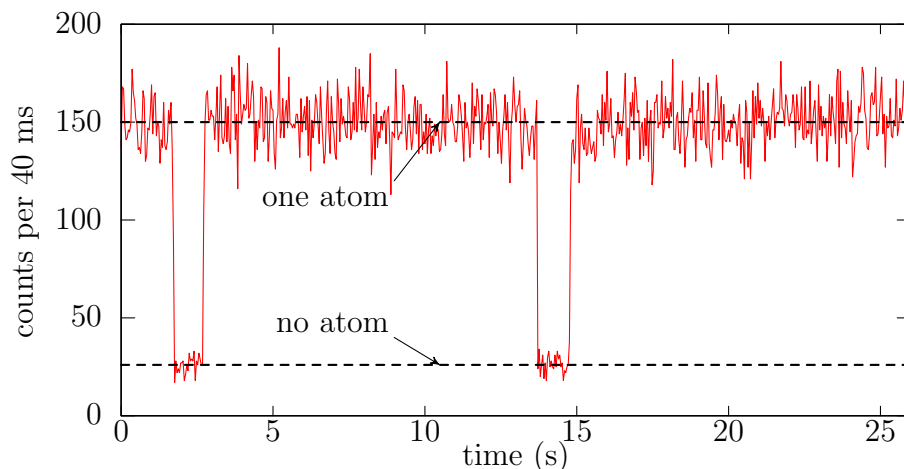


**Figure 2.3:** The fluorescence light of the single atom inside the optical dipole trap detected by APDs. The atom is continuously cooled. Due to the tight focus only one atom can remain in the trap.

of the magnetic field gradient causes that light is resonant depending on its position relative to the origin of the magnetic field. This causes friction, hence cooling, and a cloud of several thousand cold atoms is formed [61, 62].

### 2.3.2 Optical dipole trap

The center of the MOT is overlapped with the focus of a tightly focused laser that is far red-detuned to the  $5^2S_{1/2} \rightarrow 5^2P_{1/2,3/2}$  transitions at a wave length of 856 nm generating an optical dipole trap (ODT) with a conservative potential to trap a single  $^{87}\text{Rb}$  atom [55, 63]. The trap light induces a light shift of the atomic ground state and thereby generates the trap potential. The output of a single-mode laser diode is coupled into a single-mode optical fiber and guided to the confocal microscope. The intensity of the trap light is monitored with a photo diode and stabilized by an AOM and a PID-controller in a closed loop as shown in fig. 2.2. The optical dipole trap is focused to a spot with a waist of  $1.94 \pm 0.03 \mu\text{m}$  and a Rayleigh range of  $13.8 \pm 0.4 \mu\text{m}$  (See table A.5 for more details). The polarization of the trap light is cleaned by a polarizer to avoid Zeeman-state dependence of the potential [7].

**Detection of atoms** The confocal microscope is used not only to focus the optical dipole trap but also to collect fluorescence light of the atoms inside the trap into a single-mode optical fiber guiding it to single photon counting detectors, here Avalanche Photo Diodes (APDs). The counts of the photon detectors are monitored

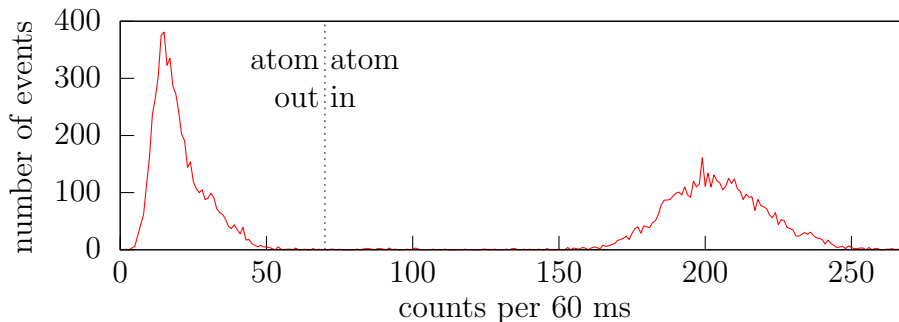


**Figure 2.4:** *Fluorescence detection:* To determine if an atom is present the fluorescence light of the trapped atom is detected by APDs and their counts are integrated over 60 ms. If more than 70 counts are registered the atom is assumed to be in the trap while at lower count rates the trap is assumed to be empty.

by a computer program. A typical trace can be seen in fig. 2.3. The control program recognizes the step-like increase in fluorescence counts and subsequently switches off the quadrupole field of the MOT to prevent further atoms entering the trap region. In fig. 2.3 the atom is further illuminated with cooling light until it leaves the trap. The step-like decrease in count rate indicates the loss of an atom and the loading sequence is repeated.

To determine if an atom is lost during an experimental sequence, cooling light is switched on and the fluorescence counts are integrated for 60 ms (see fig. 2.4) at the end of any pulse sequence. If the count rate is above a certain threshold we assume that the atom "survived" the experimental sequence in the trap. As we can see in fig. 2.4 the threshold is set to 70 counts/s and an accurate distinction can be made. The drawback of this method is the time required to determine the result of an experiment by several milliseconds. This led to the developments of channel electron multipliers [32, 44] and an atomic read-out scheme based on ionization described in the course of this thesis.

For each realization of the experiment we get the binary answer "atom in the trap" or "no atom in the trap". The relative frequency for the corresponding result can be calculated as  $\frac{N_{in}}{N}$  or  $\frac{N_{out}}{N}$  with  $N = N_{in} + N_{out}$  is the total number of performed experiments. One can estimate the probability  $p_{in} = \frac{N_{in}}{N}$  with the the statistical error as the standard deviation of the Bernoulli experiment

$$\sigma = \sqrt{\frac{1}{N}p_{in}(1 - p_{in})}. \quad (2.1)$$

Based on this considerations the errors are estimated throughout the thesis.

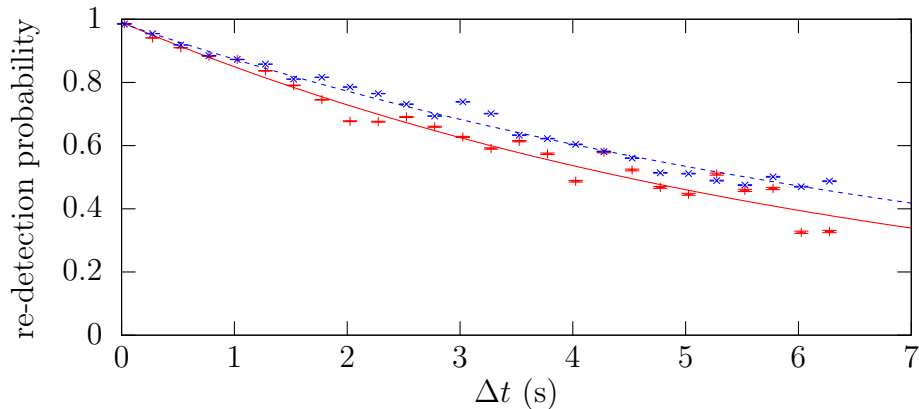


**Figure 2.5:** Probability to re-detect the atom after the time  $\Delta t$ : Shown is the life time of a trapped atom while continuously cooled (red) or in absence of cooling light (blue). In the latter case the cooling light is switched off after the loading of an atom and after  $\Delta t$  the cooling light is switched on again to determine whether the atom is still present. The exponential fits on the data yield a life time of  $6.53 \pm 0.18$  s and  $8.14 \pm 0.16$  s, respectively.

**Measurement of trapping time** As we use a tightly focused trap beam and only shallow field gradients of the magneto-optical trap, the density of the atoms around the optical dipole trap is too low to overcome the blockade mechanism as described in [55,63]. This effect accounts for an elegant way that only a single atom is present as any further atom leads to the loss of both atoms. This collisional blockade gives rise to two different operational modes of the trap. The first case is the "dark" trap where an atom is captured in the trap and no further cooling light is applied. In contrast to the "dark" trap the atom is continuously cooled in the "bright" trap.

In the "bright" trap the life time is limited by collisions with the hot background gas and parametric heating from intensity noise of the trap potential. The life time is determined by switching on the magneto-optical trap until an atom is present. Then the magneto-optical trap and the cooling light is switched off for a certain time  $\Delta t$ . After this time cooling light is switched on and via the fluorescence detection the presence of an atom is scrutinized. The measurement is repeated for different  $\Delta t$ . As we neglect heating because of beam-pointing noise, the re-detection probabilities of the atom in the trap goes like  $e^{-t/\tau}$  [64]. To reduce statistical errors the experiments are repeated several hundred times for each  $\Delta t$  to retrieve the relative frequencies of re-detecting the atom.

In the "bright" trap cooling light can on one side counteract parametric heating but

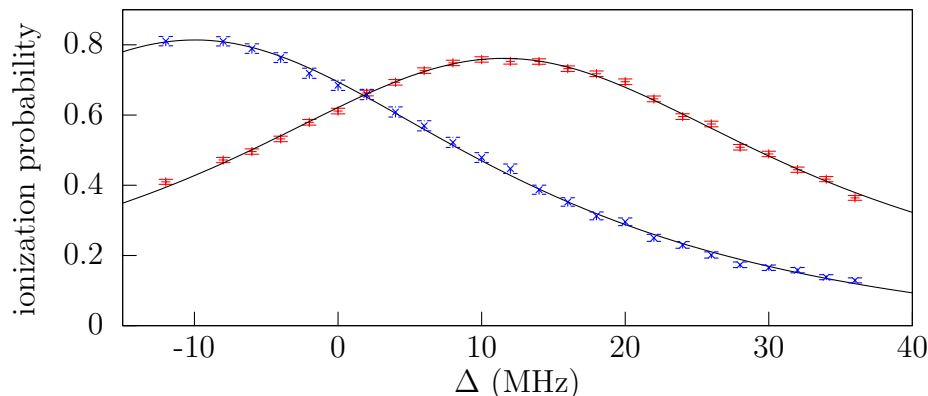


**Figure 2.6:** *Light shift induced by the optical dipole trap:* We compare the ionization probability of the atom when the optical dipole trap is switched on during the ionisation process (red) or switched off (blue). By varying the frequency of the cycling laser we scan over the Lorentzian profile of the  $5^2S_{1/2}, |F = 2\rangle \rightarrow 5^2P_{3/2}, |F' = 3\rangle$  transition. A fit to the Lorentzian (2.2) is shown in black. The peak of the probabilities are located at  $\Delta_{\text{off}} = -9.97 \pm 0.38$  MHz and  $\Delta_{\text{on}} = 11.53 \pm 0.11$  MHz, resulting in a light shift of the optical dipole trap of  $\Delta_{\text{ODT}} = 21.5 \pm 0.396$  MHz.

it also decelerates further atoms and induces inelastic collisions between two atoms. Any imbalance in the cooling beam can also lead to an increased lost rate and we expect a shorter life time for the trapped atom [56]. As in case of the "dark" trap we determine the presence of an atom after the time  $\Delta t$  and calculate the relative frequencies of re-detecting the atom.

The results are shown in fig. 2.5. The  $e^{-1}$  life time is  $8.14 \pm 0.16$  s for the dark trap and  $6.53 \pm 0.18$  s for the bright trap and, as expected, we see the longer life time of the "dark" trap. The measured storage time is sufficient for our experiments.

**Determination of the trapping potential** The optical dipole trap generates a conservative potential by inducing a light shift of the ground state of  $^{87}\text{Rb}$  [65]. To determine the trap potential we measure the light shift of the  $5^2S_{1/2}, |F = 2\rangle \rightarrow 5^2P_{3/2}, |F' = 3\rangle$  transition. For this purpose the frequency of the laser light resonant to the cycling transition is varied by an AOM to sweep over the atomic resonance. The excited atom is ionized with a certain probability as described in more detail in chapter 4.2. The ionization probability depends on the laser frequency and shows

a Lorentzian profile

$$f(\Delta) = a_0 \frac{\delta}{\Delta^2 + \delta^2}, \quad (2.2)$$

where  $\delta$  is the full width at half-maximum (FWHM) of the line and  $\Delta$  is the detuning of the cycling laser relative to the atomic resonance frequency [53,66]. To resolve the light shift caused by the trap potential, we compare the central frequency of the profile when the trap is on and when the trap is switched off during the ionization process. By fitting eq. (2.2) onto the data the peaks of the profile can be determined and a difference of  $\Delta_{\text{ODT}} = 21.5 \pm 0.396$  MHz is obtained as shown in 2.6. We see a broadening of the line compared to the natural line width of  $2\pi \cdot 6.0666(18)$  MHz. As we use a low intensity  $I_{\text{cycling}} = 15 \cdot I_{\text{sat}}$ , the broadening arises not only from power broadening but also from the Zeeman state dependent light shift caused by the ionization light of 450 nm (see chapter 3) and by adding a further decay channel to the atomic system described in chapter 4.

The experimental setup as described here enables us to store a  $^{87}\text{Rb}$  atom for a sufficient amount of time. The storage time is orders of magnitude larger than the time required for the generation and verification of entanglement between the polarization of a photon and the spin state of the atom based on fluorescence detection.

# Chapter 3

## ac-Stark Shift

For the read-out of the atomic qubit (shortly introduced in chapter 1.1.3) intense laser light is used to ionize a  $^{87}\text{Rb}$  atom depending on its Zeeman spin state. In order to achieve a high-fidelity read-out of the atomic state the precise frequency of the atomic resonance has to be known. With this knowledge off-resonant excitations can be suppressed. The atomic resonance is subject to the ac-Stark shift caused by both the optical dipole trap at a wavelength of  $\lambda_{\text{ODT}} = 856 \text{ nm}$  and the laser light used to ionize the atom at  $\lambda_{\text{ion}} = 450 \text{ nm}$ . Therefore the influence of both fields is reviewed. These preliminary studies are a first step towards the Zeeman state dependent ionization described chapter in 4.

### 3.1 The interaction Hamiltonian

If we assume the wavelength of the radiation to be larger than the size of the atom, so that the dipole approximation can be used, the interaction of an oscillating electric field  $\mathbf{E}$  with an atom is described by the Hamiltonian

$$\hat{\mathcal{H}} = \hat{\mathcal{H}}_{Atom} + \hat{\mathcal{H}}_{Field} - e \mathbf{d} \cdot \mathbf{E}, \quad (3.1)$$

where  $\hat{\mathcal{H}}_{Atom}$  is the Hamiltonian of the unperturbed atom and  $\hat{\mathcal{H}}_{Field}$  the Hamiltonian of the radiation field [67].  $\mathbf{d}$  is the position vector of the (outer) electron and  $e$  its charge.

The electric field can be written with the annihilation (creation) operators  $\hat{a}_{\mathbf{k}}$  ( $\hat{a}_{\mathbf{k}}^\dagger$ ) as

$$\mathbf{E}(\mathbf{r}, t) = \sum_{\mathbf{k}} \hat{\epsilon}_{\mathbf{k}} \mathcal{E}_{\mathbf{k}} \hat{a}_{\mathbf{k}} e^{-i\omega_{\mathbf{k}}t + i\mathbf{k} \cdot \mathbf{r}} + \sum_{\mathbf{k}} \hat{\epsilon}_{\mathbf{k}} \mathcal{E}_{\mathbf{k}} \hat{a}_{\mathbf{k}}^\dagger e^{i\omega_{\mathbf{k}}t - i\mathbf{k} \cdot \mathbf{r}} \quad (3.2a)$$

$$= \mathbf{E}^{(+)}(\mathbf{r}, t) + \mathbf{E}^{(-)}(\mathbf{r}, t) \quad (3.2b)$$

where  $\mathcal{E}_{\mathbf{k}} = \sqrt{\frac{\hbar\omega_{\mathbf{k}}}{2\epsilon_0 V}}$  is the amplitude of the electric field for wave vector  $\mathbf{k}$ , the polarization is assumed to be linear along the polarization unit vector  $\hat{\epsilon}_{\mathbf{k}} \in \mathbb{R}^3$ , and the mode volume  $V$  [67].

The Hamiltonian of the free field can be written as

$$\hat{\mathcal{H}}_{Field} = \sum_{\mathbf{k}} \hbar\omega_{\mathbf{k}} \left( \hat{a}_{\mathbf{k}}^\dagger \hat{a}_{\mathbf{k}} + \frac{1}{2} \right). \quad (3.3)$$

Let  $\{|i\rangle\}$  with  $\sum_i |i\rangle \langle i| = \mathbb{1}$  be a complete set of atomic energy eigenstates and  $\hat{\sigma}_{ij} = |i\rangle \langle j|$  the atomic transition operators, then the atomic Hamiltonian can be written as

$$\hat{\mathcal{H}}_{Atom} = \sum_i E_i |i\rangle \langle i| = \sum_i E_i \hat{\sigma}_{ii}. \quad (3.4)$$

For the position operator we get

$$e\mathbf{d} = \sum_{i,j} e |i\rangle \langle i| \mathbf{d} |j\rangle \langle j| = \sum_{i,j} \mathcal{P}_{ij} \hat{\sigma}_{ij} \quad (3.5)$$

with  $\mathcal{P}_{ij} = e \langle i| \mathbf{d} |j\rangle$  the electric dipole transition matrix element. By using

$$g_{\mathbf{k}}^{ij} = -\frac{\mathcal{P}_{ij} \cdot \hat{\epsilon}_{\mathbf{k}} \mathcal{E}_{\mathbf{k}}}{\hbar} \quad (3.6)$$

and dropping the zero-point energy of  $\hat{\mathcal{H}}_{Field}$  [67], (3.1) becomes

$$\hat{\mathcal{H}} = \sum_{\mathbf{k}} \hbar\nu_{\mathbf{k}} \hat{a}_{\mathbf{k}}^\dagger \hat{a}_{\mathbf{k}} + \sum_i E_i \hat{\sigma}_{ii} + \hbar \sum_{i,j} \sum_{\mathbf{k}} g_{\mathbf{k}}^{ij} \hat{\sigma}_{ij} \left( \hat{a}_{\mathbf{k}} e^{-\nu_{\mathbf{k}} t} + \hat{a}_{\mathbf{k}}^\dagger e^{\nu_{\mathbf{k}} t} \right). \quad (3.7)$$

If we now take the atomic ladder operators

$$\hat{\sigma}_{ij}^z = |i\rangle \langle i| - |j\rangle \langle j| \quad (3.8a)$$

$$\hat{\sigma}_{ij}^+ = |i\rangle \langle j| \quad (3.8b)$$

$$\hat{\sigma}_{ij}^- = |j\rangle \langle i| \quad (3.8c)$$

write the energy difference of the atomic levels  $(E_i - E_j) = \hbar\omega_{ij}$ , and omit constant energy terms, we end up with the Hamiltonian as

$$\hat{\mathcal{H}} = \underbrace{\sum_{\mathbf{k}} \hbar\nu_{\mathbf{k}} \hat{a}_{\mathbf{k}}^\dagger \hat{a}_{\mathbf{k}} + \sum_i E_i \hat{\sigma}_{ii}}_{\hat{\mathcal{H}}_0} + \underbrace{\hbar \sum_{i,j} \sum_{\mathbf{k}} g_{\mathbf{k}}^{ij} (\hat{\sigma}_{ij}^+ + \hat{\sigma}_{ij}^-)}_{\hat{\mathcal{V}}(t)} \cdot \left( \hat{a}_{\mathbf{k}} e^{-\nu_{\mathbf{k}} t} + \hat{a}_{\mathbf{k}}^\dagger e^{\nu_{\mathbf{k}} t} \right) \quad (3.9)$$

where the last term describes the interaction between the atom and the light field. So far only the dipole approximation is used. The *rotating-wave approximation* (RWA) is explicitly not used until now to make sure not to lose any significant effects as not only resonant effects shall be considered.

### 3.1.1 Time-dependent perturbation theory

The Hamiltonian of the atom-photon system given in (3.9) is clearly time-dependent. Hence we want to use time-dependent perturbation theory for further insight [68]. We can split the Hamiltonian (3.9) into two parts, namely

$$\hat{\mathcal{H}} = \hat{\mathcal{H}}_0 + \hat{\mathcal{V}}(t) \quad (3.10)$$

and we end up with a time-independent part  $\hat{\mathcal{H}}_0$  and the time-dependent part  $\hat{\mathcal{V}}(t)$ . For  $\hat{\mathcal{V}}(t) = 0$  we assume that  $|n\rangle$  are the known atomic energy eigenstates<sup>1</sup> of  $\hat{\mathcal{H}}_0$  satisfying

$$\hat{\mathcal{H}}_0 |n\rangle = E_n |n\rangle. \quad (3.11)$$

We want to know how a certain initial state which at  $t = 0$  is given by

$$|\Psi(t=0)\rangle = \sum_n c_n(t=0) |n\rangle \quad (3.12)$$

evolves and we are interested in  $c_n(t)$  in a way that

$$|\Psi(t)\rangle = \sum_n c_n(t) e^{-\frac{iE_n t}{\hbar}} |n\rangle. \quad (3.13)$$

Here the time evolution of  $c_n(t)$  is only due to  $\hat{\mathcal{V}}(t)$  and the probability to find the system in state  $|n\rangle$  is found by evaluating  $|c_n(t)|^2$ .

#### Interaction picture

For calculating  $|c_n(t)|^2$  it is convenient to change to the *Interaction* or *Dirac* picture where we define

$$|\Psi(t)\rangle_I = e^{\frac{i\hat{\mathcal{H}}_0 t}{\hbar}} |\Psi(t)\rangle_S \quad (3.14)$$

For any observable we can connect the Schrödinger and the Interaction picture via

$$\hat{\mathcal{A}}_I = e^{\frac{i\hat{\mathcal{H}}_0 t}{\hbar}} \hat{\mathcal{A}}_S e^{-\frac{i\hat{\mathcal{H}}_0 t}{\hbar}}. \quad (3.15)$$

---

<sup>1</sup>For the considerations of time-dependent perturbation theory the atomic eigenstates are labeled  $|n\rangle$  to avoid confusion with the notation used before where the atomic states were labeled with  $|i\rangle, |j\rangle$ .

Taking the time derivative of (3.14) with the Hamiltonian of (3.10) we see that

$$i\hbar \frac{\partial}{\partial t} |\Psi(t)\rangle_I = \hat{\mathcal{V}}_I |\Psi(t)\rangle_I \quad (3.16)$$

which is a Schrödinger-like equation [68] with the total  $\hat{\mathcal{H}}$  replaced by  $\hat{\mathcal{V}}_I$ . The wave function  $|\Psi(t)\rangle_I$  can be expanded as

$$|\Psi(t)\rangle_I = \sum_n c_n(t) |n\rangle \quad (3.17)$$

with  $|n\rangle$  being basis states in the interaction picture. Making use of the fact that

$$c_n(t) = \langle n | \Psi(t) \rangle_I \quad (3.18)$$

(3.16) results in a couples system of equations

$$i\hbar \frac{d}{dt} c_n(t) = \sum_m V_{nm} e^{i\omega_{nm}t} c_m(t) \quad (3.19)$$

with  $\omega_{nm} = (E_n - E_m)/\hbar$  and

$$V_{nm}(t) e^{i\omega_{nm}t} = \langle n | e^{i\hat{\mathcal{H}}_0 t/\hbar} \hat{\mathcal{V}}(t) e^{-i\hat{\mathcal{H}}_0 t/\hbar} | m \rangle. \quad (3.20)$$

**Dyson series** For the time-dependent perturbation theory we want to expand the coefficients of (3.18) as

$$c_n(t) = c_n^{(0)} + c_n^{(1)} + c_n^{(2)} + \dots \quad (3.21)$$

in a power series of the the strength parameter  $g_{\mathbf{k}}$  of the time-dependent potential in eq. (3.9) to solve the differential equation (3.19). With the time-evolution operator  $\hat{\mathcal{U}}_I(t)$

$$|\Psi(t)\rangle_I = \hat{\mathcal{U}}_I(t) |\Psi(t=t_0)\rangle_I \quad (3.22)$$

eq. (3.16) is analogous to

$$i\hbar \frac{d}{dt} \hat{\mathcal{U}}_I(t) = \hat{\mathcal{V}}_I(t) \hat{\mathcal{U}}_I(t). \quad (3.23)$$

This can be solved for the initial condition  $\hat{\mathcal{U}}_I(t)|_{t=t_0} = 1$  by integrating

$$\hat{\mathcal{U}}_I(t, t_0) = 1 - \frac{i}{\hbar} \int_{t_0}^t \hat{\mathcal{V}}_I(t') \hat{\mathcal{U}}_I(t', t_0) dt'. \quad (3.24)$$

Eq. (3.22) can be approximated by iterating the last step eq. (3.24) and the Dyson series [69] is obtained

$$\hat{\mathcal{U}}_I(t, t_0) = 1 - \frac{i}{\hbar} \int_{t_0}^t \hat{\mathcal{V}}_I(t') \left( 1 - \frac{i}{\hbar} \int_{t_0}^{t'} \hat{\mathcal{V}}_I(t'') \hat{\mathcal{U}}_I(t'', t_0) dt'' \right) dt' \quad (3.25a)$$

$$\begin{aligned} &= 1 - \int_{t_0}^t dt' \hat{\mathcal{V}}_I(t') + \left( \frac{-i}{\hbar} \right)^2 \int_{t_0}^t dt' \int_{t_0}^{t'} dt'' \hat{\mathcal{V}}_I(t') \hat{\mathcal{V}}_I(t'') \\ &+ \dots + \\ &\left( \frac{-i}{\hbar} \right)^n \int_{t_0}^t dt' \int_{t_0}^{t'} dt'' \dots \int_{t_0}^{t^{n-1}} dt^n \times \hat{\mathcal{V}}_I(t') \hat{\mathcal{V}}_I(t'') \dots \hat{\mathcal{V}}_I(t^n) \end{aligned} \quad (3.25b)$$

from which the time development of the initial state  $|i\rangle$  at  $t_0 = 0$  can be computed via (3.22) as

$$\begin{aligned} |i\rangle_I &= \hat{\mathcal{U}}_I(t, 0) |i\rangle_I = \sum_n |n\rangle \langle n | \hat{\mathcal{U}}_I(t, 0) |i\rangle_I \\ &= \sum_n c_n(t) |n\rangle \end{aligned} \quad (3.26)$$

Both sides of this equation can be expanded via (3.21) and (3.25b) and using (3.20), we obtain while restricting to second order perturbation theory

$$c_n^{(0)}(t) = \delta_{ni} \quad (3.27a)$$

$$c_n^{(1)}(t) = \frac{-i}{\hbar} \int_{t_0}^t e^{i\omega_{ni}t'} V_{ni}(t') dt' \quad (3.27b)$$

$$c_n^{(2)}(t) = \left( \frac{-i}{\hbar} \right)^2 \sum_m \int_{t_0}^t dt' \int_{t_0}^{t'} dt'' e^{i\omega_{nm}t'} V_{nm}(t') e^{i\omega_{mi}t''} V_{mi}(t'') \quad (3.27c)$$

**Slowly turning on the perturbation** For calculating the influence of the perturbation on the eigenstates of the system, we slowly turn on the perturbation, starting in the past with  $\hat{\mathcal{V}}(t \rightarrow -\infty) = 0$  and we achieve the full strength of the perturbation at  $t = 0$  according to

$$\hat{\mathcal{V}}(t) = e^{nt} \hat{\mathcal{V}}. \quad (3.28)$$

with  $\hat{\mathcal{V}}$  time-independent. With the system prepared in the state  $|i\rangle$  in the interaction picture at time  $-\infty$ ,  $c_i(t < 0)$  can be calculated using (3.27) as

$$\begin{aligned} c_i^{(0)}(t) &= 1 \\ c_i^{(1)}(t) &= \frac{-\iota}{\hbar} V_{ii} \lim_{t_0 \rightarrow -\infty} \int_{t_0}^t e^{\eta t'} dt' = \frac{-\iota}{\hbar \eta} V_{ii} e^{\eta t} \\ c_i^{(2)}(t) &= \left(\frac{-\iota}{\hbar}\right)^2 |V_{ii}|^2 \frac{e^{2\eta t}}{2\eta^2} + \left(\frac{-\iota}{\hbar}\right) \sum_{m \neq i} \frac{|V_{mi}|^2 e^{2\eta t}}{2\eta (E_i - E_m + \iota \hbar \eta)} \end{aligned}$$

and up to the second order we have

$$c_i(t) \approx 1 - \frac{\iota}{\hbar \eta} V_{ii} e^{\eta t} + \left(\frac{-\iota}{\hbar}\right)^2 |V_{ii}|^2 \frac{e^{2\eta t}}{2\eta^2} + \left(\frac{-\iota}{\hbar}\right) \sum_{m \neq i} \frac{|V_{mi}|^2 e^{2\eta t}}{2\eta (E_i - E_m + \iota \hbar \eta)} \quad (3.29)$$

To retrieve a time independent expression [68], we calculate the time derivative of (3.29)  $\dot{c}_i(t)$ , divide it by  $c_i(t)$  and let  $\eta \rightarrow 0$ , i.e. replace  $e^{\eta t}$  by unity, hence

$$\frac{\dot{c}_i(t)}{c_i(t)} \approx -\frac{\iota}{\hbar} V_{ii} + \left(\frac{-\iota}{\hbar}\right) \sum_{m \neq i} \frac{|V_{mi}|^2}{(E_i - E_m)}. \quad (3.30)$$

With the ansatz

$$c_i(t) = e^{-\iota \Delta_i t / \hbar}$$

we obtain

$$\frac{\dot{c}_i(t)}{c_i(t)} = \frac{-\iota}{\hbar} \Delta_i \quad (3.31)$$

where  $\Delta_i$  is now constant in time and consistent with the r.h.s. of (3.30) as well as with results given by the time-independent perturbation method.

The physical meaning of  $\Delta_i$  can be understood by bearing in mind that  $e^{-\iota \Delta_i t / \hbar} |i\rangle$  in the interaction picture is connected to  $e^{-\iota (\Delta_i + E_i) t / \hbar} |i\rangle$  in the Schrödinger picture. Thus, due to the interaction with the electromagnetic field, the energy of the state  $|i\rangle$  is therefore shifted from

$$E_i \rightarrow E_i + \Delta_i. \quad (3.32)$$

**Harmonic perturbation** For calculating the energy shift of the system caused by a harmonic perturbation [68, 70] of the form

$$\hat{\mathcal{V}}(t) = \hat{\mathfrak{V}} e^{\iota \omega t} + \hat{\mathfrak{V}}^\dagger e^{-\iota \omega t} \quad (3.33)$$

e.g. an oscillating electric field, the considerations mentioned before are still valid. The only thing one has to do is to substitute

$$E_{n(m)} - E_i \rightarrow E_{n(m)} - E_i \pm \hbar\omega$$

in (3.29). The energy shift [68] can thus be written as

$$\Delta E/\hbar \approx \sum_{m \neq i} \frac{|V_{mi}|^2}{(\omega_i - \omega_m \pm \omega)} \quad (3.34)$$

and we can apply this to (3.9). In the next chapter we will see how an intense laser light field of the form (3.33) affects the level structure of the atomic levels. As the light shift depends only on  $|V_{mi}|^2$  it can be seen that for an atomic system the light shift depends on the levels which are coupled by the electromagnetic field.

### 3.1.2 Light shift in $^{87}\text{Rb}$

The Hamiltonian describing the interaction between an atom and a light field as given in (3.9) is in the interaction picture

$$\begin{aligned} \hat{\mathcal{V}}(t) = \hbar \sum_{i,j} \sum_{\mathbf{k}} g_{\mathbf{k}}^{ij} \left\{ \left( \hat{\sigma}_{ij}^+ \hat{a}_{\mathbf{k}}^\dagger e^{i\Delta_{ij\mathbf{k}}^+ t} + \hat{\sigma}_{ij}^- \hat{a}_{\mathbf{k}} e^{-i\Delta_{ij\mathbf{k}}^+ t} \right) + \right. \\ \left. + \left( \hat{\sigma}_{ij}^+ \hat{a}_{\mathbf{k}} e^{i\Delta_{ij\mathbf{k}}^- t} + \hat{\sigma}_{ij}^- \hat{a}_{\mathbf{k}}^\dagger e^{-i\Delta_{ij\mathbf{k}}^- t} \right) \right\} \end{aligned} \quad (3.35)$$

with  $\Delta_{ij\mathbf{k}}^\pm = \omega_i - \omega_j \pm \omega_{\mathbf{k}}$ . Tracing over the light field<sup>2</sup> the ac-Stark shift can be calculated in the light of (3.34) is

$$\Delta E_{ij}/\hbar \approx \sum_{i \neq j} \left( \frac{|g_L^{ij} \hat{\sigma}_{ij}^+|^2}{\Delta_{ijL}^+} + \frac{|g_L^{ij} \hat{\sigma}_{ij}^-|^2}{\Delta_{ijL}^+} + \frac{|g_L^{ij} \hat{\sigma}_{ij}^+|^2}{\Delta_{ijL}^-} + \frac{|g_L^{ij} \hat{\sigma}_{ij}^-|^2}{\Delta_{ijL}^-} \right) \quad (3.36)$$

The *rotating wave approximation* can be applied and the energy non-conserving terms  $|g_L^{ij} \hat{\sigma}_{ij}^+|^2 / \Delta_{ijL}^+$  and  $|g_L^{ij} \hat{\sigma}_{ij}^-|^2 / \Delta_{ijL}^-$  can be neglected [67]. These terms describe the cases where a photon is absorbed and the atom is de-excited and also where a photon is emitted and the atom is excited from the lower state respectively.

---

<sup>2</sup>This can be done as we are dealing with a classical intense laser light source at frequency  $\omega_L$

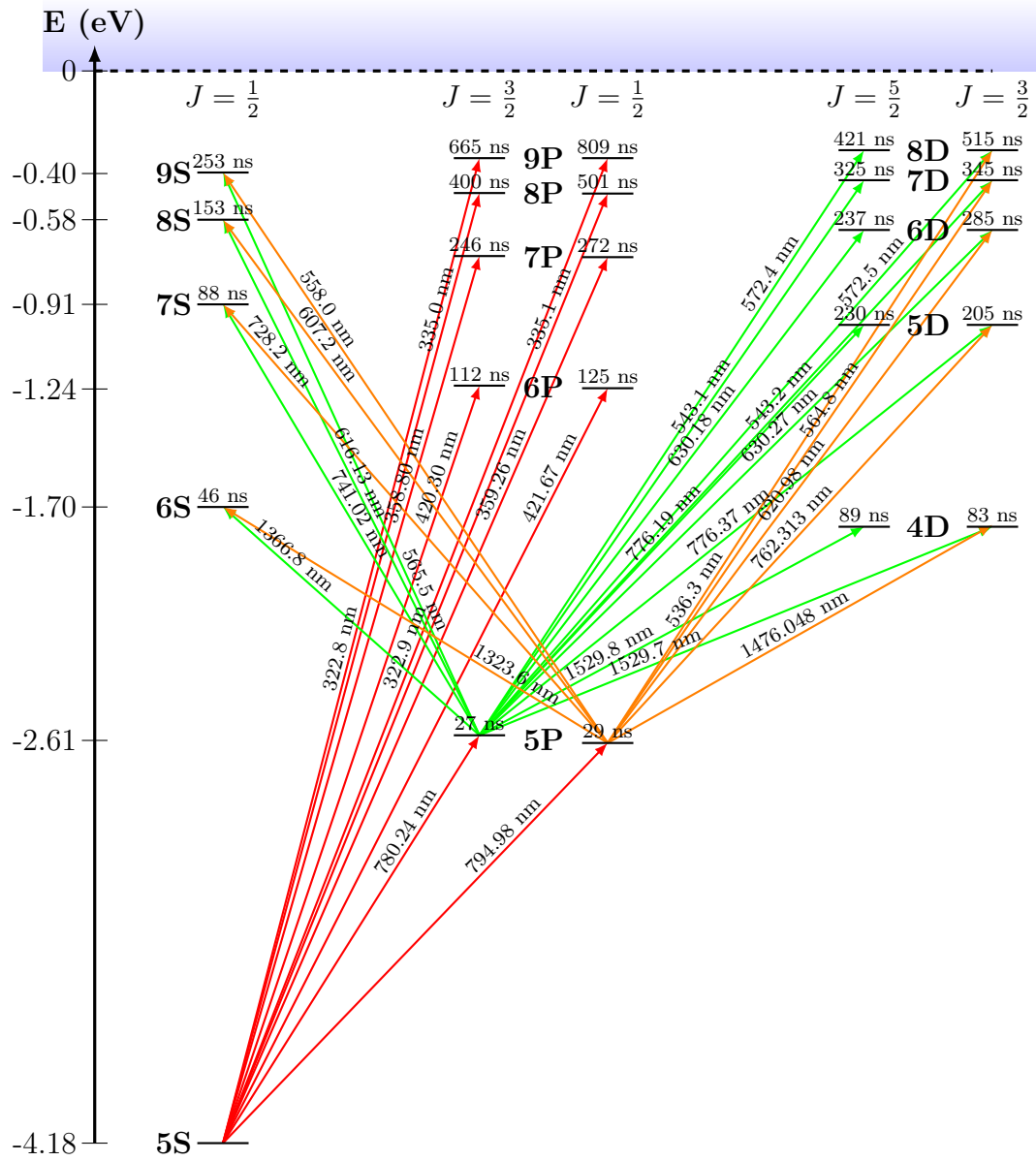


**Figure 3.1:** Level scheme of  $^{87}\text{Rb}$ . Lifetimes of the levels (black) and transition wavelength are taken from [71–73]

Transition	$A_{JJ'}(s^{-1})$	$E_J(\text{cm}^{-1})$	$E_{J'}(\text{cm}^{-1})$
$5^2S_{1/2} \rightarrow 5^2P_{1/2}$	$3.592 \cdot 10^7$	0	12578.960
$5^2S_{1/2} \rightarrow 5^2P_{3/2}$	$3.755 \cdot 10^7$	0	12816.560
$5^2S_{1/2} \rightarrow 6^2P_{1/2}$	$2.456 \cdot 10^6$	0	23717.190
$5^2S_{1/2} \rightarrow 6^2P_{3/2}$	$3.664 \cdot 10^6$	0	23792.690
$5^2S_{1/2} \rightarrow 7^2P_{1/2}$	$7.266 \cdot 10^5$	0	27835.050
$5^2S_{1/2} \rightarrow 7^2P_{3/2}$	$1.226 \cdot 10^6$	0	27870.140
$5^2S_{1/2} \rightarrow 8^2P_{1/2}$	$3.233 \cdot 10^5$	0	29834.960
$5^2S_{1/2} \rightarrow 8^2P_{3/2}$	$5.835 \cdot 10^5$	0	29853.820
$5^2S_{1/2} \rightarrow 9^2P_{1/2}$	$1.732 \cdot 10^5$	0	30958.940
$5^2S_{1/2} \rightarrow 9^2P_{3/2}$	$3.296 \cdot 10^5$	0	30970.220
$5^2P_{1/2} \rightarrow 6^2S_{1/2}$	$6.332 \cdot 10^6$	12578.960	20133.600
$5^2P_{1/2} \rightarrow 7^2S_{1/2}$	$2.640 \cdot 10^6$	12578.960	26311.460
$5^2P_{1/2} \rightarrow 8^2S_{1/2}$	$1.254 \cdot 10^6$	12578.960	29046.840
$5^2P_{1/2} \rightarrow 9^2S_{1/2}$	$6.573 \cdot 10^5$	12578.960	30499.060
$5^2P_{3/2} \rightarrow 6^2S_{1/2}$	$1.311 \cdot 10^7$	12816.560	20133.600
$5^2P_{3/2} \rightarrow 7^2S_{1/2}$	$4.400 \cdot 10^6$	12816.560	26311.460
$5^2P_{3/2} \rightarrow 8^2S_{1/2}$	$2.192 \cdot 10^6$	12816.560	29046.840
$5^2P_{3/2} \rightarrow 9^2S_{1/2}$	$1.130 \cdot 10^6$	12816.560	30499.060
$5^2P_{1/2} \rightarrow 4^2D_{3/2}$	$1.125 \cdot 10^7$	12578.960	19355.450
$5^2P_{1/2} \rightarrow 5^2D_{3/2}$	$2.438 \cdot 10^6$	12578.960	25700.560
$5^2P_{1/2} \rightarrow 6^2D_{3/2}$	$2.595 \cdot 10^6$	12578.960	28687.150
$5^2P_{1/2} \rightarrow 7^2D_{3/2}$	$2.037 \cdot 10^6$	12578.960	30280.180
$5^2P_{1/2} \rightarrow 8^2D_{3/2}$	$1.390 \cdot 10^6$	12578.960	31221.470
$5^2P_{3/2} \rightarrow 4^2D_{3/2}$	$2.080 \cdot 10^6$	12816.560	19355.450
$5^2P_{3/2} \rightarrow 5^2D_{3/2}$	$4.788 \cdot 10^5$	12816.560	25700.560
$5^2P_{3/2} \rightarrow 6^2D_{3/2}$	$5.312 \cdot 10^5$	12816.560	28687.150
$5^2P_{3/2} \rightarrow 7^2D_{3/2}$	$3.966 \cdot 10^5$	12816.560	30280.180
$5^2P_{3/2} \rightarrow 8^2D_{3/2}$	$2.824 \cdot 10^5$	12816.560	31221.470
$5^2P_{3/2} \rightarrow 4^2D_{5/2}$	$1.250 \cdot 10^7$	12816.560	19355.010
$5^2P_{3/2} \rightarrow 5^2D_{5/2}$	$2.706 \cdot 10^6$	12816.560	25703.520
$5^2P_{3/2} \rightarrow 6^2D_{5/2}$	$3.157 \cdot 10^6$	12816.560	28689.410
$5^2P_{3/2} \rightarrow 7^2D_{5/2}$	$2.457 \cdot 10^6$	12816.560	30281.690
$5^2P_{3/2} \rightarrow 8^2D_{5/2}$	$1.659 \cdot 10^6$	12816.560	31222.480

**Table 3.1:** Atomic properties of selected transitions in  $^{87}\text{Rb}$  taken from [73]. The Einstein coefficients  $A_{JJ'}$  are related to the reduced matrix element according to (3.38b) and used for the calculations shown in fig. 3.2. The energies of the states are given by  $E_J$  and  $E_{J'}$  to calculate  $\Delta_{ij\mathbf{k}}^\pm$  in (3.37).

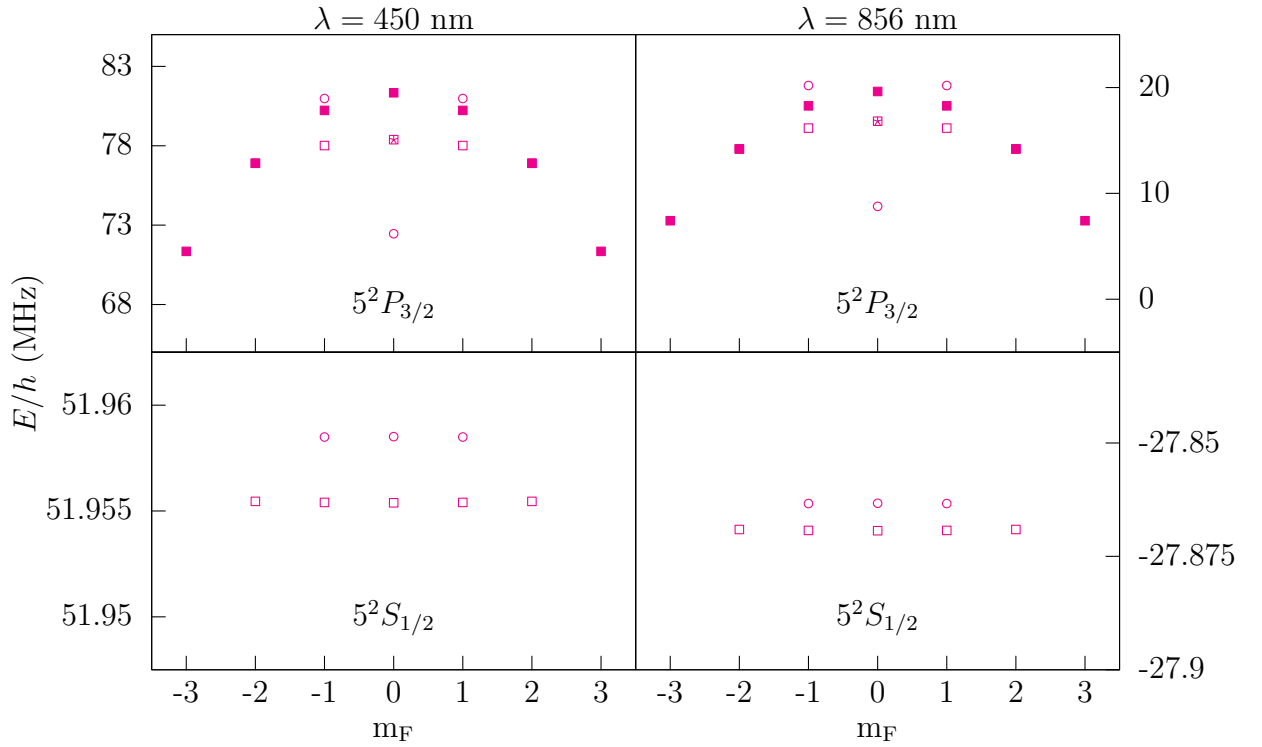


**Figure 3.2:** Predicted ac-Stark shift for different hyperfine levels in  $^{87}\text{Rb}$  as shown in fig. 4.1 and 4.6. In the upper row the light shift for the excited  $5^2P_{3/2}$  state are shown with  $F' = 0$  marked by  $*$ ,  $F' = 1$   $\circ$ ,  $F' = 2$   $\square$ ,  $F' = 3$   $\blacksquare$ . In the lower row the ground state  $5^2S_{1/2}$  with  $F = 1$  and  $F = 2$  is depicted by  $\circ$  and  $\square$

*left column:* Light shift induced by a linearly polarized laser at a wavelength of 450 nm and an intensity of  $85.2 \text{ kW/mm}^2$  used for photoionisation. The computed values can be found in D.3 while the values for circular polarized light can be found in in D.1 and D.2. The values for the states  $F' = 1, m_F = \pm 2$  and  $F' = 2, m_F = \pm 2$  coincide at these explicit set of parameter.

*right column:* Light shift induced by a linearly polarized laser at a wavelength of 856 nm at an intensity of  $2.94 \text{ kW/mm}^2$  used for the optical dipole trap.

state	$A$	$B$
$5^2S_{1/2}$	3417.341	0
$5^2P_{1/2}$	406.2	0
$5^2P_{3/2}$	84.845	12.52
$6^2S_{1/2}$	807.66	0
$6^2P_{1/2}$	132.5	0
$6^2P_{3/2}$	27.700	3.953
$7^2S_{1/2}$	319.759	0
$7^2P_{1/2}$	59.32	0
$7^2P_{3/2}$	12.57	1.762
$8^2S_{1/2}$	159.2	0
$8^2P_{1/2}$	32.12	0
$8^2P_{3/2}$	6.739	0.935
$9^2S_{1/2}$	90.9	0
$9^2S_{1/2}$		0
$9^2P_{3/2}$	4.05	0.55
$4^2D_{3/2}$	25.1	2.230
$4^2D_{5/2}$	-16.9	3.166
$5^2D_{3/2}$	14.43	0.913
$5^2D_{5/2}$	-7.44	1.290
$6^2D_{3/2}$	7.84	0.442
$6^2D_{5/2}$	-3.4	0.623
$7^2D_{3/2}$	4.53	0.243
$7^2D_{5/2}$	-2.0	0.343
$8^2D_{3/2}$	2.840	0.147
$8^2D_{5/2}$	-1.20	0.207
$9^2D_{3/2}$	1.90	0.094
$9^2D_{5/2}$	-0.80	0.133

**Table 3.2:** Hyperfine constants  $A$  and  $B$  (in MHz) of  $^{87}\text{Rb}$  [71] used for calculating the hyperfine level split eq. (3.40).

The ac-Stark shift of a hyperfine level  $|F, m_F\rangle$  is therefore given by

$$\Delta E_{F,m_F}/\hbar \approx \sum_{F',m_{F'}} \left\{ \frac{\left| \langle F, m_F | g_{\mathbf{k}}^{\{F,m_F\},\{F',m_{F'}\}} | F', m_{F'} \rangle \right|^2}{\Delta_{ijL}^+} + \frac{\left| \langle F, m_F | g_{\mathbf{k}}^{\{F,m_F\},\{F',m_{F'}\}} | F', m_{F'} \rangle \right|^2}{\Delta_{ijL}^-} \right\} \quad (3.37)$$

where the sum goes over all atomic states that couple to the light field. The matrix element  $\langle F, m_F | g_{\mathbf{k}}^{\{F,m_F\},\{F',m_{F'}\}} | F', m_{F'} \rangle$  represents the coupling between the levels  $|F, m_F\rangle$  and  $|F', m_{F'}\rangle$ . We can factor out the angular dependence with a reduced matrix element, and using Wigner 3-j and 6-j symbols [68, 74–76] we obtain

$$\begin{aligned} \langle F, m_F | g_{\mathbf{k}}^{\{F,m_F\},\{F',m_{F'}\}} | F', m_{F'} \rangle &= \\ &= \langle F || e \hat{\epsilon}_{\mathbf{k}} || F' \rangle (-1)^{F'-1+m_F} \sqrt{2F+1} \cdot \begin{pmatrix} F' & 1 & F \\ m'_{F'} & q & m_F \end{pmatrix}_{3j} \end{aligned} \quad (3.38a)$$

$$\begin{aligned} &= \langle J || e \hat{\epsilon}_{\mathbf{k}} || J' \rangle (-1)^{J+m_F+I} \sqrt{(2F+1)(2F'+1)(2J+1)} \times \\ &\times \begin{pmatrix} F' & 1 & F \\ m'_{F'} & q & m_F \end{pmatrix}_{3j} \cdot \left\{ \begin{matrix} J & J' & 1 \\ F' & F & I \end{matrix} \right\}_{6j} \end{aligned} \quad (3.38b)$$

The 3-j symbol vanishes unless the sublevels satisfy  $m_F = m'_{F'} + q$  where  $q \in \{0, \pm 1\}$  describes the polarization of the light field. The nuclear angular momentum  $I$  for  $^{87}\text{Rb}$  is  $3/2$  (see table A.2).

The reduced matrix element  $\langle J || e \hat{\epsilon}_{\mathbf{k}} || J' \rangle$  in eq. 3.38b is connected to the Einstein coefficients of the state and the life time of the respective atomic state via

$$\frac{1}{\tau_{JJ'}} = A_{JJ'} = \frac{\omega_0^3}{3\pi\epsilon_0\hbar c^3} \cdot \frac{2J+1}{2J'+1} |\langle J || e \hat{x}_q || J' \rangle|^2 \quad (3.39)$$

with  $\omega_0 = |\omega_{J'} - \omega_J|$  [77].

One can see in (3.38b) and (3.37) that for the calculation of the ac-Stark shift the hyperfine states of the atomic states have to be considered. For this purpose the exact frequency of the transitions  $\omega_0$  can be calculated with the hyperfine energy shift [74] as

$$\Delta E_{hfs} = A_{hfs} \frac{K}{2} + B_{hfs} \frac{\frac{3}{2}K(K+1) - 2I(I+1)J(J+1)}{4I(2I-1)J(2J-1)} \quad (3.40)$$

where  $K = F(F+1) - I(I+1) - J(J+1)$ . The values for the magnetic dipole

constant  $A_{hfs}$  and the electric quadrupole constant  $B_{hfs}$  can be found in [71, 74]. The magnetic octupole constant  $C_{hfs}$  is not considered in our calculations as measurements in general are not yet sufficiently precise to provide a nonzero value for  $C_{hfs}$ , and thus it is not listed [74]. The values for the states considered for the calculations are shown in tab. 3.2. The accuracy of the predicted energy shift depends now on the number of atomic states taken into account. From the values provided by [71–73] we can now calculate the light shifts of the  $5^2S_{1/2} \rightarrow 5^2P_{1/2,3/2}$  transition. In our setup the intensity of the ionization laser can be as high as  $85.2 \text{ kW/mm}^2$  while the optical dipole trap is operated at an intensity of  $2.94 \text{ kW/mm}^2$ . For both wavelength and intensities we calculated the shift of the levels according to (3.37). This is then compared to the measured values shown in chapter 3.2.

For an intensity of  $85.2 \text{ kW/mm}^2$  the predicted relative light shift for a wavelength of 450 nm is 28 MHz for the  $5^2S_{1/2}, |F = 2\rangle \rightarrow 5^2P_{3/2}, |F' = 3\rangle$  transition. Both the ground state  $5^2S_{1/2}, |F = 2\rangle$  and the  $5^2P_{3/2}, |F' = 3\rangle$  state are shifted upwards in frequency. This result is in good agreement with the measured values shown below. Contrary to this, the relative light shift of the  $5^2S_{1/2}, |F = 2\rangle \rightarrow 5^2P_{3/2}, |F' = 3\rangle$  transition induced by the optical dipole trap at a wavelength of 856 nm is predicted to be 45 MHz where the ground state shifts downwards and the excited state upwards.

In the measurements shown in fig. 2.6 we observe a light shift of 21 MHz. This disagreement can be caused by wave front aberrations of the light field or diffraction errors of the microscope objective but is still a subject worth of further investigations. One can see in fig. 3.2 that the induced light shift of the ground state does not depend on the Zeeman state  $m_F$  when using linearly polarized light while the excited state clearly dependence on  $m_F$ . The optical dipole trap can therefore trap atoms independent of the Zeeman state of the  $^{87}\text{Rb}$  atom.

## 3.2 Measurements of the Light Shift

As we have seen in the previous chapter, an intense laser light shifts the atomic levels due to the ac-Stark shift. In order to ionize the atom from the  $5^2S_{1/2}, |F = 2\rangle$  ground state via the intermediate state  $5^2P_{3/2}, |F' = 3\rangle$  with high fidelity the atomic resonance has to be determined with high accuracy. The experimentally determined values are compared with the estimated values for the ac-Stark shift for a laser at a wavelength of 450 nm. The values shown in fig. 3.2 are for a single intensity but depending on  $m_F$ . From eq. (3.37) we see a linear dependency of the light shift of the intensity. For this purpose we vary the intensity of the ionization laser and measure the relative light shifts induced by the ionization laser at wavelength of 450 nm.

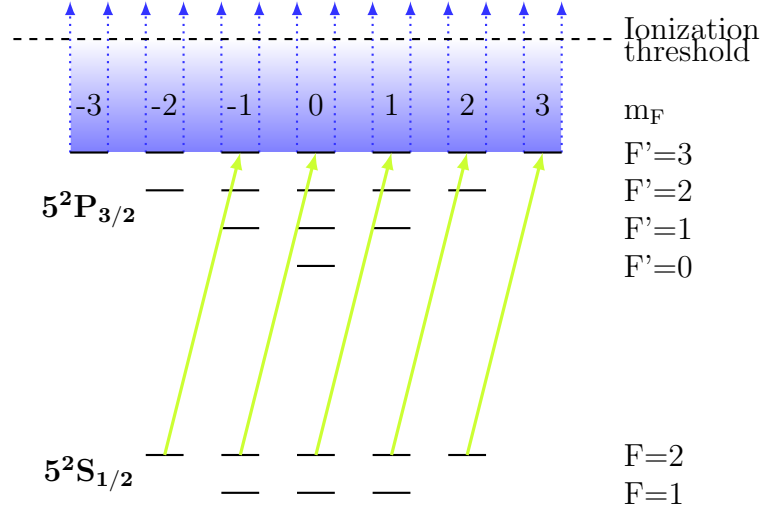


**Figure 3.3:** *Hyperfine state detection:* The atom is initially prepared in the  $5^2S_{1/2}, |F = 2\rangle$  state. From there it is excited to the  $5^2P_{3/2}, |F' = 3\rangle$  state and subsequently ionized.

### 3.2.1 Experimental Sequence

After loading a single atom in the optical dipole trap, as described in section 2.3.2, the experimental sequence starts by optically pumping the atomic state into the  $5^2S_{1/2}, |F = 2\rangle$  ground state. This is achieved by depopulating the  $5^2S_{1/2}, |F = 1\rangle$  ground state with light resonant to the  $5^2S_{1/2}, |F = 1\rangle \rightarrow 5^2P_{3/2}$  transitions. From this initial state the atom is ionized by a two step photo-ionization as shown in fig 3.3. The first red laser of a wavelength of 780 nm is tuned close to the resonance of the  $5^2S_{1/2}, |F = 2\rangle \rightarrow 5^2P_{3/2}, |F' = 3\rangle$  cycling transition while the second laser has a wavelength of 450 nm with sufficient energy to ionize the atom. This laser light induces a light shift on the states involved in the cycling transition as shown above. The change of the  $5^2S_{1/2}, |F = 2\rangle \rightarrow 5^2P_{3/2}, |F' = 3\rangle$  transition frequency is determined by measuring the ionization probability for different detuning of the cycling laser. In detail, the frequency is varied by an acousto-optical modulator (AOM) [78] over a range of 52 MHz. The pulse sequence is shown in fig. 3.4. The Cycling transition is driven for 325 ns temporally embedded into the ionization pulse of 450 ns. The population of the intermediate state  $5^2P_{3/2}, |F' = 3\rangle$  changes by varying the frequency of the Cycling laser. The population is higher the closer the frequency of the laser is to the resonance of the shifted transition. As this atomic state is meant to get ionized, the ionization probability is a measure for the population of the intermediate state. The loss of the atom due to photo-ionization is detected by switching on the cooling light again after the pulse sequence and

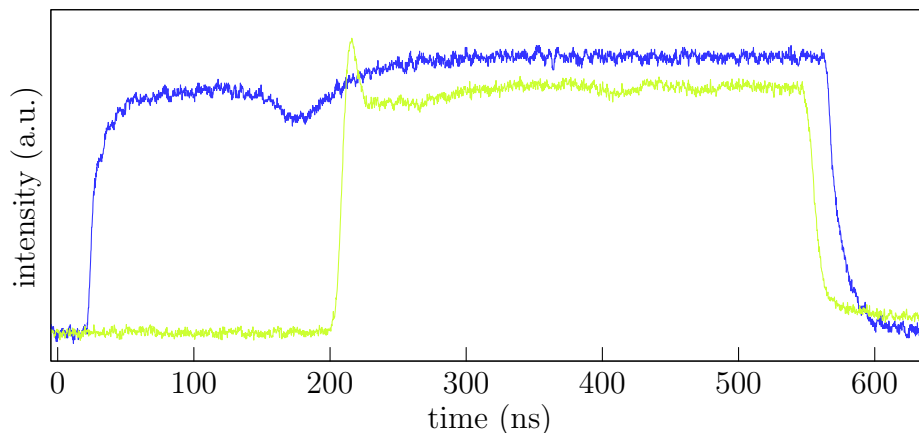


**Figure 3.4:** Typical pulse sequence for ionizing the  $5^2S_{1/2}, |F = 2\rangle$  state. The cycling pulse — has a FWHM of 325 ns and an intensity of  $15 \cdot I_{sat} = 250 \mu\text{W}/\text{mm}^2$ . The intensity of the ionisation pulse — is varied up to  $85.2 \text{ kW}/\text{mm}^2$ . The cycling pulse is placed after an dip in the ionization pulse caused by the overdrive of the diode to ensure an approx. constant ionization rate.

integrating the number of detected photons similar to the procedure described on page 21. If the atom is removed from the trap, we assess that it was ionized, since the  $^{87}\text{Rb}^+$  ion can not be held in our optical dipole trap. Contrary to this, if the atom is still present, no ionization took place. To see the dependency of the light shift on the intensity of the ionization laser light as expected from eq. (3.37) these measurements are repeated for different intensities of the ionization laser.

### 3.2.2 Measurements of the Ionization Probability Depending on the Laser Frequency

At the beginning of the experimental sequence the atom is prepared in the  $5^2S_{1/2}, |F = 2\rangle$  state [44]. Subsequently, the probability to ionize the atom depending on the frequency of the cycling light is determined. Therefore, the frequency of the cycling laser is varied from  $\Delta = -16 \text{ MHz}$  to  $\Delta = 36 \text{ MHz}$  with respect to the unperturbed atomic resonance for which  $\Delta = 0$ . The ionization laser induces a light shift of the ground state in opposition to the light shift that is induced by the optical dipole trap. The depth of the trap and hence the induced light shift is kept constant at 21.5 MHz as explained in sec. 2.3.2. In fig. 3.5 the result for an intensity of  $I_{450 \text{ nm}} = 42.6 \text{ kW}/\text{mm}^2$  is shown. The Lorentzian profile eq. 2.2 is then fitted to the measured values. We obtain a light shift of  $\Delta = 11.5 \pm 0.19 \text{ MHz}$  relative to the unperturbed atomic transition for the  $5^2S_{1/2}, |F = 2\rangle \rightarrow 5^2P_{3/2}, |F' = 3\rangle$

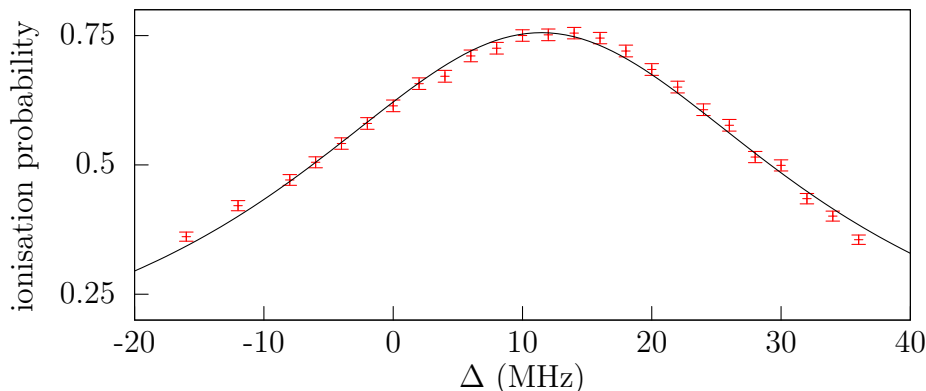


**Figure 3.5:** *Dependency of the ionization rate on the frequency detuning of the excitation light of the  $5^2S_{1/2}, |F = 2\rangle \rightarrow 5^2P_{3/2}, |F' = 3\rangle$  transition:* Shown is the probability to re-detect the atom after an ionization pulse sequence for different detunings  $\Delta$ . The intensity of the ionization laser is  $I_{450 \text{ nm}} = 49.8 \text{ kW/mm}^2$ . The light shift  $\delta = 11.5 \pm 0.19 \text{ MHz}$  determined by fitting the Lorentzian function (2.2) shown in black. The error bars indicate the  $1\sigma$  standard deviation. To circumvent significant power broadening of the line the Cycling laser intensity  $I_{cyc} = 6 \cdot I_{sat}$ . Therefore the ionization probability does not reach values above 0.75.

transition (see fig. 2.1), whereas the line width is  $24.3 \pm 1.8 \text{ MHz}$  by fitting (2.2) to the data [79].

This observed line broadening is caused by three contributions. At the beginning of the ionization pulse sequence each Zeeman level is assumed to be equally populated, thus we observe a mixture of all light shifts as we can not resolve a single state in particular. For a perfectly linearly polarized light field we expect a splitting difference of 5.8 MHz. Additionally, any admixture of circularly polarized light to the ionizing light field causes an even bigger spread of the light-shifts for different Zeeman levels as it can be seen in tab. D.1 and D.2. For a purely circular polarized light field, we expect a spread of 37.5 MHz. This effect is reduced by means of controlling the output polarization of the optical fiber by 3-paddle polarization controller.

A further contribution is the reduction of the life time of the  $5^2P_{3/2} |F' = 3\rangle$  state due to the additional decay channel opened by the ionization. This can be understood by considering the ionization process within a three level system with the states  $|1\rangle, |2\rangle, |3\rangle$  as the ground, excited and ionization state respectively. The natural line width is determined by the decay rate  $\Gamma_{2 \rightarrow 1}$ . If we treat the ionization process equivalent to a spontaneous decay from  $|2\rangle \rightarrow |3\rangle$  with the decay rate  $\Gamma_{2 \rightarrow 3}$  we see a broadening of the transition  $|1\rangle \rightarrow |2\rangle$  if we increase the ionization rate [80].

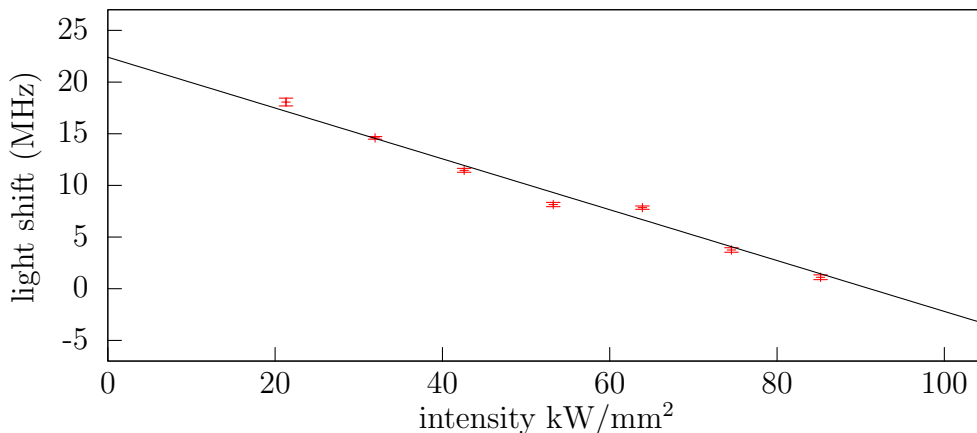


**Figure 3.6:** *Light shift induced by the ionization laser:* For increasing intensity of the ionization laser the frequency of the  $5^2S_{1/2}, |F=2\rangle \rightarrow 5^2P_{3/2}, |F'=3\rangle$  transition decreases by  $-0.246 \pm 0.017 \text{ MHz}/\frac{\text{kW}}{\text{mm}^2}$  obtained from a linear fit on the measured light shifts depicted by  $+$ . The fit also reproduces the result for the optical dipole trap of  $21.5 \pm 0.396 \text{ MHz}$  where the intensity  $I_{450 \text{ nm}} = 0$ .

This will be discussed in detail in chapter 4 and the results can be seen in fig. 4.5. The last contribution are aberrations of the microscope objective considering the light field of the optical dipole trap [81].

### 3.2.3 Dependency of the Light Shift for Increasing Ionization Rates

As a next step, we are interested in the dependency of the light shift on increasing ionization rate. Since the wavelength of the ionization laser is 450 nm, hence blue detuned for all transitions from  $5^2S_{1/2}$  to  $5^2P_{1/2,3/2}$ , the transition frequency should decrease, when the intensity of the ionization laser is increased. To verify this, the measurements described in the previous chapter are performed for different intensities of the ionization laser and the results are shown in fig. 3.6. For each data point a measurement as described above is performed and the position of the center of the Lorentzian profile is plotted. We obtain a decrease in the transition frequency by  $-0.246 \pm 0.017 \text{ MHz}/\frac{\text{kW}}{\text{mm}^2}$  by fitting a linear function to these data. This result is in good agreement with the calculations shown in fig. 3.2, where we expect a light shift averaged over all  $m_F$  of 24.9 MHz at an intensity of 85.2 kW/mm<sup>2</sup> and the results shown in section 2.3.2.

### 3.2.4 Summary

In this chapter the principles of the interaction between an atom and a light field were shown. Starting from an ab initio approach, we were able to derive predictions for the light shift in a  $^{87}\text{Rb}$  atom with high accuracy by second order time dependent perturbation theory. The experimental results for measuring the light shift were in good agreement with these calculations and we are able to calibrate the frequency of the cycling laser in a way to resonantly drive the  $5^2S_{1/2}, |F = 2\rangle \rightarrow 5^2P_{3/2}, |F' = 3\rangle$  transition with high fidelity avoiding off-resonant excitations. The calculations for the optical dipole trap do not agree with the measured light shift of  $21.5 \pm 0.396$  MHz. The reason for this can be the incomplete data set for the calculations and aberrations of the microscope objective used for the optical dipole trap causing polarization dependent light shifts [7]. The Zeeman state dependency of the light shift of the excited state can cause line broadening for both cases and can explain the line width depicted in fig. 2.6, whereas both light fields do not lift the degeneracy of the ground state under the assumption that they are perfectly linear polarized. This ensures the indistinguishability of the atomic state after the generation of Atom-photon entanglement as described in section 1.1.3.

## Chapter 4

# Ultra Fast High Fidelity Read-Out of Atomic State

In order to verify entanglement between the polarization state of a photon and the spin state of an atom, both the polarization state of the photon and the spin state of the atom have to be determined. While the photonic state can be measured using polarization analysis, the read-out of the atomic spin state can be realized in various ways. For atomic ions the so-called shelving technique can be utilized due to the deep potential of an ion trap. In this case, the atom emits sufficient photons, while it is optically driven on a closed transition [82–84]. Neutral atoms confined in a shallow trap would be lost due to the light pressure of the laser light before they can scatter enough photons to discriminate the atomic hyperfine state [6,7,55]. In recent experiments this was circumvented by a STIRAP-process [85], where an atomic Zeeman state was first mapped onto a hyperfine state and thereupon the atom was removed from the trap depending on the hyperfine state. A two step process has been implemented for a faster and more accurate state detection, where the atom is first excited from the ground state depending on its Zeeman state and in a second step the excited state is ionized.

In this chapter the ionization process is modeled by the Lindblad master equation to determine the experimental requirements for a successful read-out of the atomic spin state. The Master equation will be used for solving a three level atomic system for the read-out of hyperfine states as already shown in fig 3.3, while in section 4.2 the read-out of Zeeman states as depicted in fig. 4.6 will be investigated within the frame work of a six level system [86]. For all calculations the corresponding measurements are presented.

## 4.1 Hyperfine State Ionization

It is necessary to understand the dynamics of the read-out process based on ionization to achieve a high-fidelity read-out of the atomic state. Ionizing the intermediate state  $5^2P_{3/2}, |F' = 3\rangle$  opens an additional decay channel, which leads to a broadening of the line and can cause off-resonant excitations reducing state-selectivity. This effect is discussed in the following, first by modeling the relevant atomic states with a three level system consisting of the ground level  $5^2S_{1/2}, |F = 2\rangle$  ( $|1\rangle$ ), the intermediate excited state  $5^2P_{3/2}, |F' = 3\rangle$  ( $|2\rangle$ ) and the ionized state ( $|3\rangle$ ) as shown in fig. 4.1. By calculating the evolution of the population of each state we see a broadening of the line width different from the line broadening of a two level system. For this purpose, we compare a simple model of a two-level system with a three level system, analyzing the master equation using the calculated and measured line width. One obtains the line width of a transition driven by a monochromatic wave, which is broadened by the applied ionization laser field. For a two-level system the line width is influenced (only) by the power of the driving field and determined by the number of scattered photons. Finally, the results of the calculations will be compared with experimental results.

### 4.1.1 Two-Level System

First, let us consider the case of a two-level atom with ground (excited) state  $|g\rangle$  ( $|e\rangle$ ) using the density matrix

$$\hat{\rho} = \sum_i p_i |\psi_i\rangle \langle \psi_i|. \quad (4.1)$$

In the two-dimensional case here  $\hat{\rho} = \begin{pmatrix} \rho_{gg} & \rho_{ge} \\ \rho_{eg} & \rho_{ee} \end{pmatrix}$ . The line width of the transition can be observed by detecting the scattered light, while scanning the frequency of a narrow band laser around the resonance [53, 87–89]. In the steady state the scattering rate  $\Gamma_P$  is proportional to the population of the excited state  $\rho_{ee}$  and the decay rate  $\gamma$

$$\gamma_P = \gamma \rho_{ee} = \frac{s_0 \cdot \frac{\gamma}{2}}{1 + s_0 + \left(\frac{2\delta}{\gamma}\right)^2}. \quad (4.2)$$

Here,  $s_0 = I/I_{sat}$  is the on-resonance saturation parameter with the saturation intensity  $I_{sat} = \pi \hbar c / 3 \lambda^3 \tau$ . For high intensities ( $s_0 \gg 1$ ) the ground and excited state are equally populated and  $\gamma_P \rightarrow \gamma/2$ , and

$$\Gamma_P = \left( \frac{s_0}{1 + s_0} \right) \left( \frac{\gamma/2}{1 + (2\delta/\gamma')^2} \right)$$

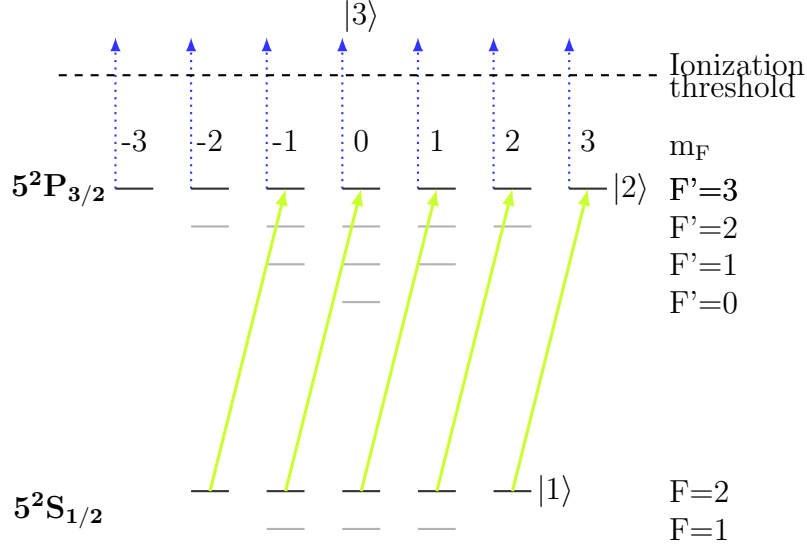


**Figure 4.1:** *Hyperfine state selective ionization:* The atom is initially prepared in the  $5^2S_{1/2}, |F = 2\rangle$  state ( $|1\rangle$ ). From there it is excited to the  $5^2P_{3/2}, |F' = 3\rangle$  state ( $|2\rangle$ ) and subsequently ionized ( $|3\rangle$ ).

with

$$\gamma' = \gamma\sqrt{1 + s_0} \quad (4.3)$$

being the so-called power broadened line width of the transition [53].

### 4.1.2 Three-Level System

Next, we consider an atomic three-level system with the additional level  $|3\rangle$  as depicted in fig. 4.1. Contrary to an atomic two-level system the time evolution of the system can not be described analytically. In general, the dynamics of a  $N$ -dimensional quantum system described by the density matrix  $\hat{\rho}$  interacting with a light field can be described by the *Lindblad* Master-equation [86,90]

$$\dot{\rho}(t) = -\frac{i}{\hbar} [\hat{\mathcal{V}}(t), \rho] - \sum_{i,j} \frac{\Gamma_{ij}}{2} (\hat{\sigma}_{ij}^- \hat{\sigma}_{ij}^+ \rho(t) + \rho(t) \hat{\sigma}_{ij}^- \hat{\sigma}_{ij}^+ - 2\hat{\sigma}_{ij}^+ \rho(t) \hat{\sigma}_{ij}^-) = \hat{\mathcal{L}} \cdot \rho \quad (4.4)$$

with the atom-light interaction Hamiltonian  $\hat{\mathcal{V}}(t)$  similar to (3.10) and the annihilation and creation operators (3.8) connecting the states  $|i\rangle$  and  $|j\rangle$  as a linear basis of the system, while  $\Gamma_{ij}$  describes a spontaneous decay from  $|j\rangle \rightarrow |i\rangle$  by determining the dynamics of the system.

The evolution of the atomic state's density matrix  $\hat{\rho}(t)$  is determined by evaluating  $\dot{\rho}(t) = \hat{\mathcal{L}} \cdot \rho$  with

$$\hat{\mathcal{L}} \cdot \rho = \begin{pmatrix} l_{1,1}(t) & l_{1,2}(t) & l_{1,3}(t) \\ l_{2,1}(t) & l_{2,2}(t) & l_{2,3}(t) \\ l_{3,1}(t) & l_{3,2}(t) & l_{3,3}(t) \end{pmatrix}.$$

We model the ionization process as the incoherent decay rate  $\gamma_{3,2} = \Gamma_{ion}$  according to eq. (1.25), while the spontaneous decay rate of the excited state  $|2\rangle$  to the ground state  $|1\rangle$  is given by  $\gamma_{1,2} = \Gamma_{D_2}$ . As there is no coherent coupling driven by a light field between  $|1\rangle \rightarrow |3\rangle$  and  $|2\rangle \rightarrow |3\rangle$  and no decay from  $|3\rangle \rightarrow |1\rangle$  and  $|3\rangle \rightarrow |2\rangle$  (see fig. 4.1) the single elements of  $\hat{\mathcal{L}} \cdot \rho$  can be written as

$$l_{1,1}(t) = 2\gamma_{1,2}\rho_{2,2} + \imath(\rho_{1,2}\Omega_{2,1} - \rho_{2,1}\Omega_{1,2}) \quad (4.5a)$$

$$l_{1,2}(t) = \imath\{\Omega_{1,2}(\rho_{1,1} - \rho_{2,2}) + \rho_{1,2}[2\delta_1 + \imath(\gamma_{1,2} + \gamma_{3,2})]\} \quad (4.5b)$$

$$l_{1,3}(t) = \imath(2\delta_1\rho_{1,3} - \rho_{2,3}\Omega_{1,2}) \quad (4.5c)$$

$$l_{2,1}(t) = -\imath\{\Omega_{2,1}(\rho_{1,1} - \rho_{2,2}) + \rho_{2,1}[2\delta_1 - \imath(\gamma_{1,2} + \gamma_{3,2})]\} \quad (4.5d)$$

$$l_{2,2}(t) = -2(\gamma_{1,2} + \gamma_{3,2})\rho_{2,2} + \imath(\Omega_{1,2}\rho_{2,1} - \Omega_{2,1}\rho_{1,2}) \quad (4.5e)$$

$$l_{2,3}(t) = -\imath\rho_{1,3}\Omega_{2,1} - \rho_{2,3}(\gamma_{1,2} + \gamma_{3,2}) \quad (4.5f)$$

$$l_{3,1}(t) = \imath(\rho_{3,2}\Omega_{2,1} - 2\rho_{3,1}\delta_1) \quad (4.5g)$$

$$l_{3,2}(t) = \imath\rho_{3,1}\Omega_{1,2} - \rho_{3,2}(\gamma_{1,2} + \gamma_{3,2}) \quad (4.5h)$$

$$l_{3,3}(t) = 2\rho_{2,2}\gamma_{3,2}, \quad (4.5i)$$

with the Rabi frequencies  $\Omega_{i,j}(t) = \Omega_{j,i}(t)$  driving the transition  $|i\rangle \rightarrow |j\rangle$  and the light field being detuned from the respective atomic resonance by  $\delta_i$ .

Using `mathematica 8.0`<sup>TM</sup> one can numerically solve this set of partial differential equations for the populations  $\rho_{i,j}(t)$  during the ionization process. The system is initially prepared in the state  $|1\rangle$ , hence  $\rho_{1,1}(t=0) = 1$ , whereas all other elements of  $\hat{\rho}(t=0)$  are zero. Applying a light field at the transition  $5^2S_{1/2}, |F=2\rangle \rightarrow 5^2P_{3/2}, |F'=3\rangle$  leads to a population of the state  $|2\rangle$ , which can decay back to the  $5^2S_{1/2}, |F=2\rangle$  with the decay rate  $\Gamma_{D_2}$  or can get ionized with the rate  $\Gamma_{ion}$ . This ionization rate can be determined within the frame work of a rate model as

$$\Gamma_{ion} = \frac{I_p \sigma_p}{2E_p}$$

with  $\frac{I_p}{E_p}$  the photon flux of the ionization light, while  $E_p = \hbar\omega_p$  is the energy of the photon, and  $\sigma_p$  the ionization cross section [42, 91, 92].

Fig. 4.2 shows the evolution of the diagonal matrix elements hence populations

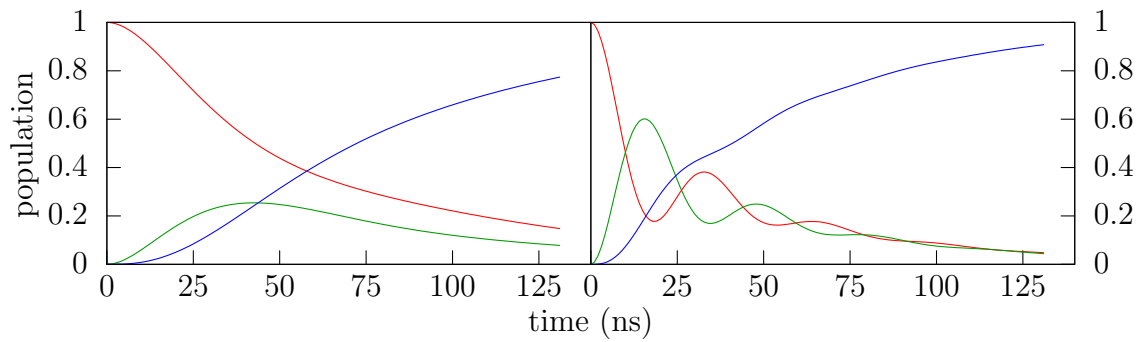


**Figure 4.2:** *Evolution of populations:* The population in levels  $|1\rangle$  (red),  $|2\rangle$  (green) and  $|3\rangle$  (red) are shown according to the model. The light field resonant to the  $5^2S_{1/2}, |F = 2\rangle \rightarrow 5^2P_{3/2}, |F' = 3\rangle$  transition with an intensity of  $I_{cyc} = 5I_{sat}$  (left) and  $I_{cyc} = 50I_{sat}$  (right) is applied for 130 ns and the intermediate state  $|2\rangle = 5^2P_{3/2}, |F' = 3\rangle$  (green) decays with a decay rate of  $\Gamma_{D_2}$  back into  $|1\rangle$  or gets ionized with an ionization rate of  $\Gamma_{ion} = \Gamma_{D_2}$  into the state  $|3\rangle$  (blue). With higher  $I_{cyc}$  the probability to ionize increases as seen on the right and the atom oscillates between the ground and excited state several times whereas at low intensities no oscillation take place. For all intensities  $I_{cyc}$  the probability to ionize the atom increases monotonously.

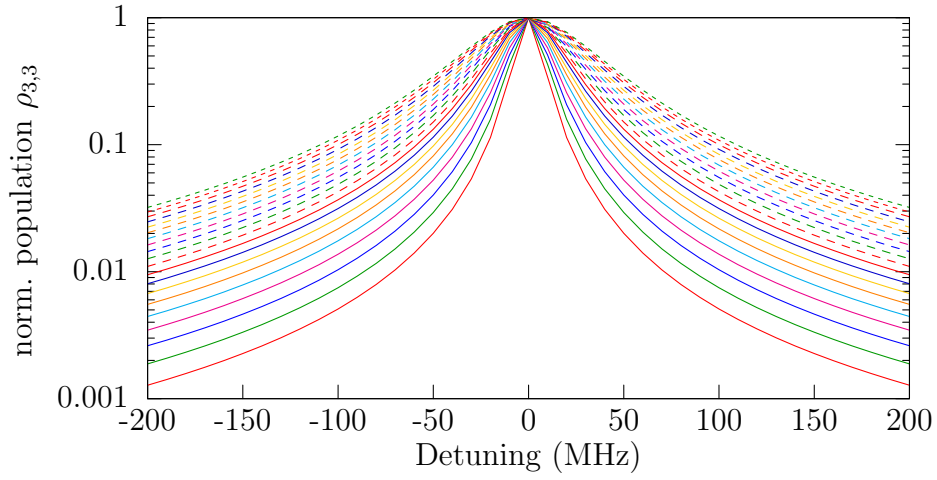


**Figure 4.3:** *Calculated line width:* Relative population of the ionization state  $\rho_{3,3}$  as a function of the detuning  $\delta_1$  of the excitation light to the  $5^2S_{1/2}, |F = 2\rangle \rightarrow 5^2P_{3/2}, |F' = 3\rangle$  ( $|1\rangle \rightarrow |2\rangle$ ) transition after a pulse length of  $t = 5/\Gamma_{D_2}$ . The ionization rate varies from  $\Gamma_{ion} = \frac{1}{2} \cdot \Gamma_{D_2}$  (solid red) to  $\Gamma_{ion} = 10 \cdot \Gamma_{D_2}$  (dashed green) while the intensity of the light field driving  $|1\rangle \rightarrow |2\rangle$  is set to  $I = I_{sat}$ . For increasing ionization rates a broadening of the line can be observed. For clarity the populations are re-normalized to unity at the resonance  $\delta_1 = 0$ .

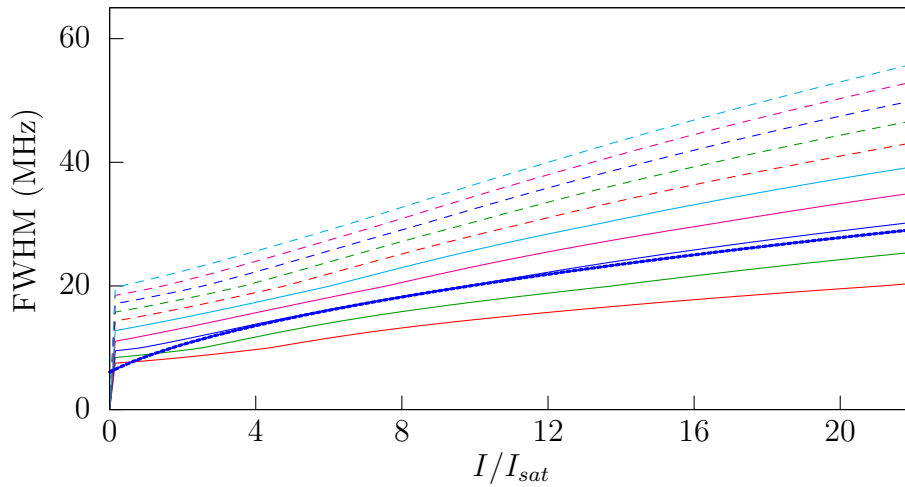


**Figure 4.4:** *Power broadening:* Depending on the intensity of the laser light driving the transition  $5^2S_{1/2}, |F = 2\rangle \rightarrow 5^2P_{3/2}, |F' = 3\rangle$  the spectral width increases with increasing ionization rate  $\Gamma_{ion}$ . Additionally, line broadening in a two-level system with  $\Gamma_{D_2}$  according to eq. (4.3) is shown (dotted blue) for reference. The line width increases with increasing ionization rate. Shown are results for ionization rates  $\Gamma_{ion} = \frac{1}{2} \cdot \Gamma_{D_2}$  (solid red) up to  $\Gamma_{ion} = 10 \cdot \Gamma_{D_2}$  (dashed turquoise) where the cycling transition is driven for 130 ns.

$\hat{\rho}_{i,i}(t)$  for the case the light on the  $|1\rangle \rightarrow |2\rangle$ -transition and the ionization laser are applied for  $T = 5/\Gamma_{D_2}$ . The probability to ionize the atom is given by the matrix element  $\rho_{3,3}(t)$  and it can be seen that  $\rho_{3,3}$  is a monotone function, which approaches unity at the end of the pulse.

Now we want to consider the dependency of the ionization probability on the frequency of the cycling light. This will be important in the context of state-selectivity of the process, as in the real atomic system there are several excited levels and their excitation can lead to an erroneous read-out. The detuning from the resonance  $\delta_1$  is varied from  $-200$  MHz to  $200$  MHz at a given intensity to calculate the line width of the  $|1\rangle \rightarrow |2\rangle$ -transition. The results for  $I = I_{sat}$  are shown in fig. 4.3 where the ionization rate is increased from  $\Gamma_{ion} = \frac{1}{2}\Gamma_{D_2}$  to  $\Gamma_{ion} = 10 \cdot \Gamma_{D_2}$  in steps of  $1/2 \cdot \Gamma_{D_2}$ . The FWHM here is defined as the detuning frequency, where the ionization probability reached half of its maximum value at resonance.

For various intensities  $I_{cyc}$  and ionization rates  $\Gamma_{ion}$  one can see that the line is broadened for high ionization rates compared to the 2-level system as shown in fig. 4.4. This is caused by opening an additional decay channel of the  $5^2P_{3/2}, |F' = 3\rangle$  excited state resulting in a reduction of its life time.

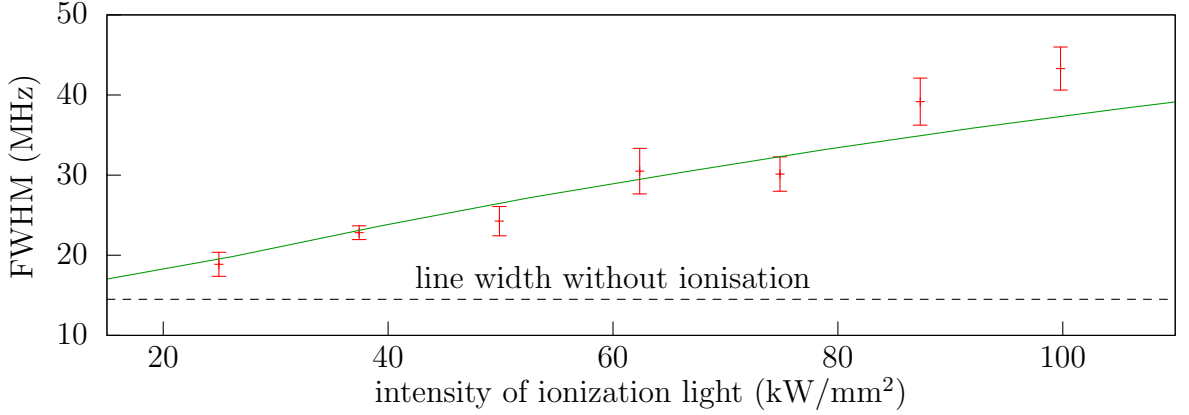


**Figure 4.5:** Measured line width of the  $5^2S_{1/2}, |F = 2\rangle \rightarrow 5^2P_{3/2}, |F' = 3\rangle$  transition depending on the intensity of the ionization laser. For higher intensities  $I_{ion}$  the line gets broader while the Cycling laser intensity is kept constant. The green line is the predicted line width obtained from solving (4.5) while the red points indicate the results obtained from fitting the ionization probabilities onto eq. (2.2). The error bars indicate the asymptotic standard errors returned from the fitting algorithm [79] while the dashed line marks the two-level line width for the applied intensity of  $I_{cyc} = 6 \cdot I_{sat}$ .

### Experimental sequence

A single atom is loaded into the optical dipole trap and prepared into the  $5^2S_{1/2}, |F = 2\rangle$  state by optical pumping to experimentally verify the broadening of the  $5^2S_{1/2}, |F = 2\rangle \rightarrow 5^2P_{3/2}, |F' = 3\rangle$  transition. A pulse sequence as shown in fig. 3.4 is applied, where for each data point a certain value for the intensity of the ionization laser  $I_{ion}$  as well as  $I_{cyc}$  is chosen and when the detuning of the Cycling laser  $\Delta_{cyc}$  from the atomic resonance is varied by an AOM. For each  $I_{ion}$  the ionization probability depending on the detuning  $\delta_{cyc}$  is recorded. An example of this procedure is already shown in fig. 2.6. We can estimate the line width of the  $5^2S_{1/2}, |F = 2\rangle \rightarrow 5^2P_{3/2}, |F' = 3\rangle$  transition by fitting a Lorentzian function (2.2) to the measured frequencies. As expected, the full width at half maximum (FWHM) increases with higher ionization rates  $\Gamma_{ion}$ . Comparing the measured line width with the calculation based on the experimental parameters, we see a good agreement of the two data sets.

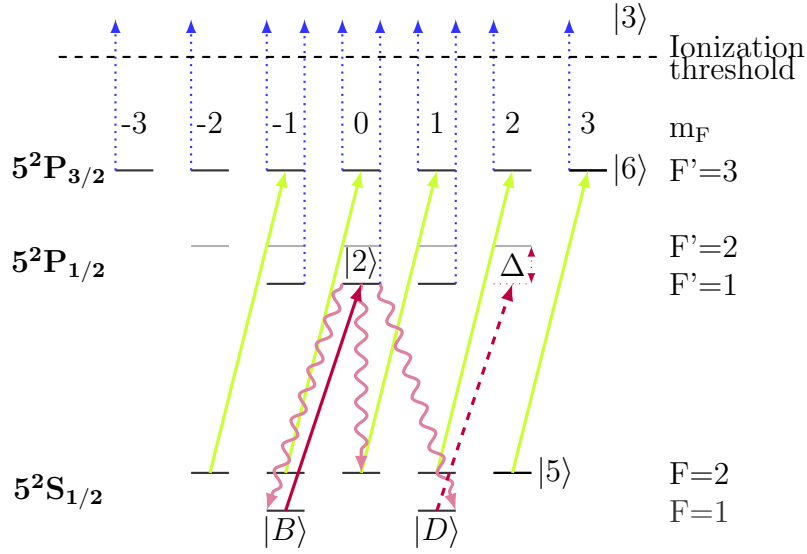


**Figure 4.6:** *Zeeman state detection:* The atom is initially prepared in the bright state  $|B\rangle = |1\rangle$ , a superposition of  $5^2S_{1/2}, |F = 1, m_F = \pm 1\rangle$  (see eq. (4.7) and gets excited to the  $5^2P_{1/2}, |F' = 1\rangle$  state  $|2\rangle$ . The excited state can either get ionized ( $|3\rangle$ ) or it can spontaneously decay either to the bright state  $|B\rangle$  or the orthogonal dark state ( $|D\rangle = |4\rangle$ ) on the  $F = 1$  ground state manifold. A further decay can occur to the  $5^2S_{1/2}, |F = 2\rangle$  ( $|5\rangle$ ) which can be emptied via the hyperfine state detection by using  $5^2P_{3/2}, |F' = 3\rangle$  as an intermediate state ( $|6\rangle$ ) that gets ionized as described in the previous chapter.

## Summary

By solving the Master equation (4.5) we are able to explain the experimentally observed broadening of the atomic transition  $5^2S_{1/2}, |F = 2\rangle \rightarrow 5^2P_{3/2}, |F' = 3\rangle$  in a  $^{87}\text{Rb}$  atom. The broadening depends not only on the intensity of the laser field driving the Cycling transition but also on the intensity of the ionization light. The photo ionization reduces the life time of the intermediate state and this leads to an increase of the line width.

## 4.2 Zeeman State Ionization

The encoding and reading out of an atomic qubit encoded in the  $|m_F = \pm 1\rangle$  subspace of the Zeeman manifold of the  $5^2S_{1/2}, |F = 1\rangle$  ground state requires the ability to distinguish different superpositions of Zeeman states  $|F = 1, m_F = \pm 1\rangle$ . As the states are energetically degenerate, the selection which state gets ionized can

not be done spectroscopically<sup>1</sup>, addressed by different frequencies [93] but via the selection rules of atomic dipole transitions. The polarization state of the read-out laser incident along the quantization axis can be written as

$$\mathcal{P} = \cos(\alpha) |L\rangle + \sin(\alpha) e^{i\phi} |R\rangle \quad (4.6)$$

(see fig. 1.1) and the atomic state that gets excited to the  $5^2P_{1/2}, |F = 1\rangle$  level (*bright* state) can be written as

$$|B\rangle = \sin(\alpha) e^{-i\phi} |1, +1\rangle - \cos(\alpha) |1, -1\rangle = |1\rangle \quad (4.7)$$

while the *dark* state

$$|D\rangle = \cos(\alpha) |1, +1\rangle + \sin(\alpha) e^{i\phi} |1, -1\rangle = |4\rangle \quad (4.8)$$

remains unaffected<sup>2</sup>.

### 4.2.1 Calculations

Similar to the previous calculations we can now calculate the probabilities for the Zeeman state dependent ionization process. For this purpose, we consider the six levels shown in fig. 4.6. To discern the *bright* state  $|B\rangle$  and the *dark* state  $|D\rangle$ , it is necessary to avoid the decay from  $5^2P_{1/2}, |F' = 1\rangle$  into the ground state. As this process is spontaneous, the excited state can now also decay in the dark state, thereby causing erroneous read-out (not ionized instead of ionized). Furthermore, the dark state can be off-resonantly excited via  $5^2P_{1/2}, |F' = 2\rangle$  and then ionized or decay into the bright state and thus also leads to a wrong read-out result (ionized instead of not ionized). From the  $5^2P_{1/2}, |F = 1\rangle$  state the Clebsch-Gordan coefficients of the transitions to the ground state lead to the fact that 5/6 of the population decays to the  $5^2S_{1/2}, |F = 2\rangle$  state, while the rest (1/6) decays into the bright and the dark state with equal probability. All the population that decays to the  $5^2S_{1/2}, |F = 2\rangle$  state will be ionized as well via the  $5^2S_{1/2}, |F = 2\rangle \rightarrow 5^2P_{3/2}, |F' = 3\rangle$  transition, hence not leading to an erroneous measurement result.

As in 4.1.2 we solve eq. (4.4)

$$\dot{\rho}(t) = \hat{\mathcal{L}} \cdot \rho$$

numerically (See appendix B for the single elements of  $\hat{\mathcal{L}} \cdot \rho$ ). The probability of ionizing the bright state depends mainly on the length and intensity of the read-out pulse and the ionization rate  $\Gamma_{ion}$ . Assuming an ionization rate  $\Gamma_{ion} = 5 \cdot \Gamma_{D_1}$  we calculate the ionization probability for a range of the read-out intensity from

<sup>1</sup>The degeneracy could be lifted by applying a magnetic field, but this causes time evolution i.e. Larmor precession, of the qubit state and hence is not favorable [7].

<sup>2</sup>The state  $5^2S_{1/2}, |F = 1, m_F = 0\rangle$  (if present) is always bright for  $\mathcal{P}$ .

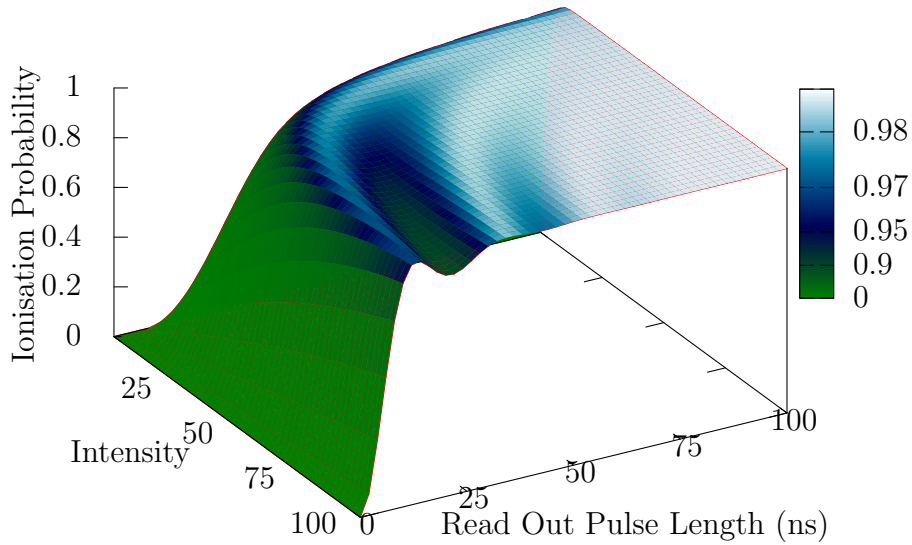


**Figure 4.7:** *Ionisation probability:* Shown is the calculated probability to ionize the bright state (4.7) depending on the pulse length and the intensity of the read-out pulse for an ionization rate of  $\Gamma_{ion} = 5 \cdot \Gamma_{D_1}$ . Depicted is the population of the matrix element  $\rho_{3,3}$

$I_{ro} = 0 \dots 100 \cdot I_{sat}$  and a pulse length from  $0 \dots 100$  ns. The result is presented in fig. 4.7. The ionization probability does not show a monotone behavior as the intermediate state can be depopulated by means of Rabi oscillations before it can get ionized. Additionally, population in the excited state can still get ionized even if the cycling laser is already switched off, as shown in fig. C.1. Due to the residual decay into the dark state the maximum ionization probability is 0.983. If the atom is initially prepared in the dark state, it still can get ionized with a probability of 0.0221 due to off-resonant excitations via the  $5^2P_{1/2}, |F = 2\rangle$  state. Hence we expect a maximum fidelity of the read-out procedure of 0.961 for this considered ionization rate and set of parameters.

## 4.2.2 Measurements

We entangle the atomic spin state with the polarization state of the photon to measure the performance of the atomic read-out scheme described above. In detail, the atom is optically pumped into the  $5^2S_{1/2}, |F = 1, m_F = 0\rangle$  state and excited to the  $5^2P_{3/2}, |F' = 0, m_F = 0\rangle$  state with a short optical pulse with a FWHM of 21 ns. From there, spontaneous decay into the  $5^2S_{1/2}, |F = 1, m_F = \{0, \pm 1\}\rangle$  state takes place. Due to the conservation of angular momentum, the atom emits a left circularly polarized photon when it decays into the  $|1, -1\rangle$  state or it emits right

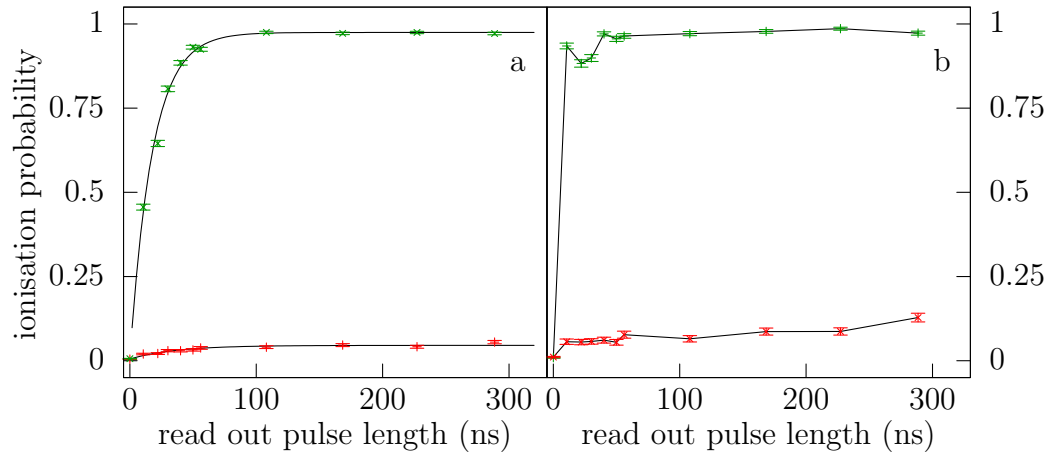


**Figure 4.8:** *Time dependency of the read-out procedure:* The atom is prepared in the bright or dark state of the read-out light field by measuring the polarization of the emitted photon (Photon in  $|\uparrow\rangle_x$  green,  $|\downarrow\rangle_x$  red). The length of the read-out pulse is varied while the intensity is kept constant. (a) For an intensity  $I = 200 \cdot I_{sat}$  the probability to ionize the atom increases giving the maximal contrast of  $0.929 \pm 0.001$ . The black curve indicates an exponential fit to the data and yields an ionization time  $\tau = 17.76 \pm 0.6$  ns. (b) For high intensities  $I = 3000 \cdot I_{sat}$  a depopulation of the intermediate state due to Rabi oscillations can be observed. Due to the high intensity the dark state shows a finite ionization probability because of off-resonant excitation to the  $5^2P_{1/2}, |F = 2\rangle$ .

circularly polarized photon when it decays into the  $|1, +1\rangle$  state. The decay into the  $5^2S_{1/2}, |F = 1, m_F = 0\rangle$  state can not be observed as the emitted  $\pi$ -photon does not couple into the detection optics. The joined atom-photon state reads therefore as

$$|\Psi_{AP}\rangle = \frac{1}{\sqrt{2}} (|1, -1\rangle |L\rangle + |1, +1\rangle |R\rangle) \quad (4.9)$$

if we define the quantization axis  $z$  as the direction in which the photons are collected by the detection optics [6, 7, 11, 47, 48, 56, 94, 95]. By measuring the polarization state of the emitted photon, the atom is projected onto a well defined spin state similar to eq (1.19). If, e.g., a  $|R\rangle$  photon is measured as shown in fig. 4.9, the state of the atom is projected into the  $|1, +1\rangle$  state and would be a bright state for a  $|L\rangle$ -polarized read-out laser pulse with the angles  $\alpha = \phi = 0$  in eq. (4.6). This argument can be extended to all other measurement bases [6, 7, 96] allowing to prepare arbitrary atomic states and to test them with different polarizations of the read-out laser. In fig. 4.8 the results for measuring the ionization probability depending on the pulse length of the read-out laser for two different intensities are shown with an ionization rate of  $\Gamma_{ion} = 5 \cdot \Gamma_{D_2}$ . The polarization of the photon is measured in  $\hat{\sigma}_x$  basis

$$|H/V\rangle_{Ph} = \frac{1}{\sqrt{2}} (|L\rangle \pm |R\rangle)$$

which projects the atom either into the dark state or the corresponding bright state of the read-out pulse (4.6) which is horizontally polarized ( $\alpha = \pi/2, \phi = 0$ ).

To estimate the required time for the read-out an exponential function  $f(x) = B - Ae^{-t/\tau}$  is fitted to the data of fig. 4.8. This can be done within a rate model to estimated the ionisation time and we obtain a result of  $\tau_{bright} = 17.8 \pm 0.56$  ns for the bright state. As we have seen in fig. 4.7 the contrast does not reach unity for finite ionization rates and we get a contrast of  $0.929 \pm 0.001$ . The difference to the calculated values can be explained by residual magnetic fields that cause Larmor precession and polarization errors both in the photonic measurement and the polarization of the read-out laser.

The calculated non-monotonic behavior of the ionization probability as predicted for the 6-level model (see fig. 4.7) can be seen for very high read-out intensities  $I > 3000 \cdot I_{sat}$ . As the dark state gets excited via the  $5^2P_{1/2}, |F = 2\rangle$  state the contrast is reduced to  $0.87 \pm 0.018$ . Although the ionization is faster for such high intensities this range of experimental parameters has to be discarded due to the reduced contrast compared to fig. 4.8 (a).

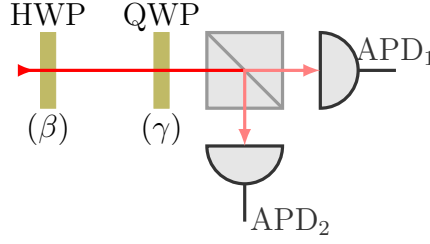


**Figure 4.9:** *Photonic state detection:* The emitted photon is coupled into a single mode optical fiber as shown in fig. 2.2. The polarization analysis consists of a quarter- and a half-wave plate to adjust the photon measurement basis by the angles  $\gamma$  and  $\beta$ . By dint of a polarizing beam splitter the polarization state can be determined if the photon is detected by an APD in the corresponding output port. This setup enables to measure on the one hand the polarization state of the photon but also to monitor the fluorescence of the trapped  $^{87}\text{Rb}$  atom.

### 4.3 Verification of Atom-Photon Entanglement

Using the methods described in the previous section we are now able to test if the spontaneous decay of  $5^2P_{3/2}, |F' = 0, m_F = 0\rangle$  generates an entangled state similar to eq. (1.19) and not a mixture of separable states. The polarization of the emitted photon can be detected by means of a polarizing beam splitter in combination with optical retarders [97] aligned along suitable axes as shown in fig. 4.9. The spin state of the atom is measured with the methods described in section 4.2, which enables us to select the atomic measurement basis simply by choosing the appropriate polarization of the read-out laser. Conditioned on the detection of a photon the atomic state detection enables a complete state tomography of the joined atom-photon state.

#### 4.3.1 Atom-Photon Correlations

In order to perform a full tomography of the atom-photon state, the ability to choose photonic measurement basis  $\hat{\sigma}_{x,y,z}$  is required. This can be done by using a combination of a half wave plate (HWP) and a quarter wave plate (QWP). We call the rotation angles of the HWP and QWP  $\beta$  and  $\gamma$  respectively. For detecting linear polarization we set  $\gamma = \pi/2$  and the photon is projected onto the state

$$\begin{aligned} \text{APD}_1 : \quad & \cos(2\beta) |H\rangle - \sin(2\beta) |V\rangle = \cos(2\beta + \frac{\pi}{4}) |P\rangle - \sin(2\beta + \frac{\pi}{4}) |M\rangle \\ \text{APD}_2 : \quad & \sin(2\beta) |H\rangle + \cos(2\beta) |V\rangle = \sin(2\beta + \frac{\pi}{4}) |P\rangle + \cos(2\beta + \frac{\pi}{4}) |M\rangle. \end{aligned}$$

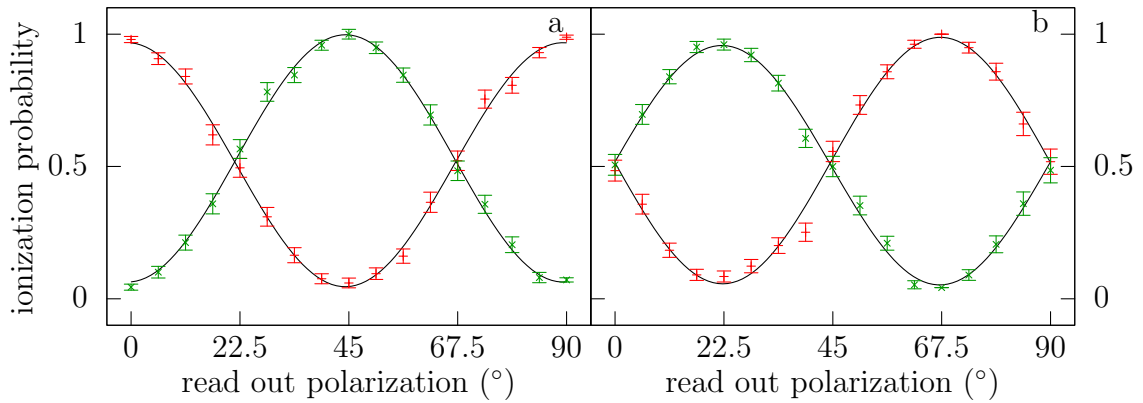


**Figure 4.10:** *Atom-photon correlations:* Shown are the probabilities to ionize the atom if the photon is measured to be in the a)  $|\uparrow\rangle_x$  (green) or  $|\downarrow\rangle_x$  (red) state while the polarization of the read-out laser is varied by a HWP from  $0^\circ$  to  $90^\circ$ . In b) the photon is measured in  $|\uparrow\rangle_y$  (green) or  $|\downarrow\rangle_y$  (red).

We can write eq. (1.19) as

$$\begin{aligned}
 |\Psi_{AP}\rangle &= \frac{1}{\sqrt{2}} (|\downarrow\rangle_z |L\rangle + |\uparrow\rangle_z |R\rangle) \\
 &= \frac{1}{\sqrt{2}} (|\downarrow\rangle_x |V\rangle + |\uparrow\rangle_x |H\rangle) \\
 &= \frac{1}{\sqrt{2}} (|\downarrow\rangle_y |P\rangle + |\uparrow\rangle_y |M\rangle)
 \end{aligned}$$

and depending on the outcome of the measurement on the photon, the atom is projected onto the corresponding state. In fig 4.10 the photon is measured in  $\hat{\sigma}_x$ -basis (a) and  $\hat{\sigma}_y$ -basis (b). In the first case, if the photon is detected in APD<sub>1</sub> (i.e. in the state  $|H\rangle$ ), the atom is projected onto the state  $|\uparrow\rangle_x$ . If the polarization of the read-out laser is set to  $\frac{1}{\sqrt{2}}(|L\rangle - |R\rangle)$ , i.e.  $\alpha = \frac{\pi}{4}$ ,  $\phi = \pi$ , the state  $|\uparrow\rangle_x$  should get ionized. Contrary to this, the  $|\downarrow\rangle_x$  state, which is prepared if the photon is detected in APD<sub>2</sub> ( $|V\rangle$ ), remains unaffected by the read-out laser. When the polarization of the read-out laser is rotated in the plane of linear polarization of the Poincaré sphere, the bright state (4.7) is also rotated and we expect the ionization probability to behave as  $\cos^2(2\phi) = 1/2 + 1/2 \cos(4\phi)$ . On the other hand the unaffected orthogonal dark state (4.8) is ionized with a probability of  $\sin^2(2\phi) = 1/2 - 1/2 \cos(4\phi)$ .

This behavior can be clearly seen in fig. 4.10 (a). The read-out procedure is started conditioned on the detection of a photon coming from a spontaneous decay of the  $5^2P_{3/2}, |F' = 0, m_F = 0\rangle$  state. If a horizontally polarized photon is measured

(APD<sub>1</sub>, red), the atom is ionized. By rotating a HWP this ionization probability is reduced and we obtain the expected  $\cos^2(2\phi)$  behavior. For the detection of a vertically polarized photon (APD<sub>2</sub>, green) the ionization probability goes like  $\sin^2(2\phi)$ . We get a visibility for the atom-photon state of  $v_{|H\rangle} = 0.922 \pm 0.0087$  ( $v_{|V\rangle} = 0.935 \pm 0.0072$ ) by fitting a sinusoidal function on the data points, respectively.

A similar behavior of the ionization probabilities can be seen in fig. 4.10 (b). Here, the photonic measurement basis is chosen to be  $\hat{\sigma}_y$ , hence the photon is detected in state  $|P\rangle$  ( $|M\rangle$ ) if measured by APD<sub>1</sub> (APD<sub>2</sub>). The polarization of the read-out laser is varied in steps of  $5.625^\circ$  as before. Therefore the probability to ionize the atom is equal 0.5 for both measured polarizations for  $\alpha = 0^\circ$  due to the commutation relations of  $\hat{\sigma}_x$  and  $\hat{\sigma}_y$ . The contrast re-appears by rotating the read-out polarization to the  $\hat{\sigma}_y$  basis and by fitting the data we obtain a visibility of  $v_{|P\rangle} = 0.932 \pm 0.0118$  ( $v_{|M\rangle} = 0.905 \pm 0.0090$ ) respectively.

With the results shown in fig. 4.10 we analyzed the correlations between the polarization of the spontaneously emitted photon from the decay of the  $5^2P_{3/2}$ ,  $|F' = 0, m_F = 0\rangle$  state and the Zeeman sub-levels of the  $^{87}\text{Rb}$  atom by measuring the photon in the complementary bases  $\hat{\sigma}_x$  and  $\hat{\sigma}_y$  and by continuously varying the polarization of the read-out laser along the equatorial plane of the atomic state Poincaré sphere. The obtained visibilities of these correlations show that the read-out procedure is capable to verify the entanglement of the joined atom-photon state as we can measure in all bases with high fidelity.

### 4.3.2 State Tomography

The results of the previous chapter prove that the joint atom-photon state can be analyzed via Zeeman state selective ionization together with polarization measurements on the photon. To test the performance and accuracy of this technique a full tomography of the entangled atom-photon state can be performed. This is done by determining the density matrix of the state and comparing it with the expected state eq. (1.19). For this purpose a tomographically (over-)complete set of projection measurements, here the eigenbasis of the Pauli spin matrices  $\hat{\sigma}_x$ ,  $\hat{\sigma}_y$ ,  $\hat{\sigma}_z$ , has to be performed [98, 99].

#### Density matrix

In the standard Pauli basis the density matrix  $\hat{\rho}$  can be expressed as

$$\hat{\rho} = \frac{1}{4} \sum_{k,l=0}^3 \langle \hat{\sigma}_k \otimes \hat{\sigma}_l \rangle \cdot \hat{\sigma}_k \otimes \hat{\sigma}_l \quad (4.10)$$

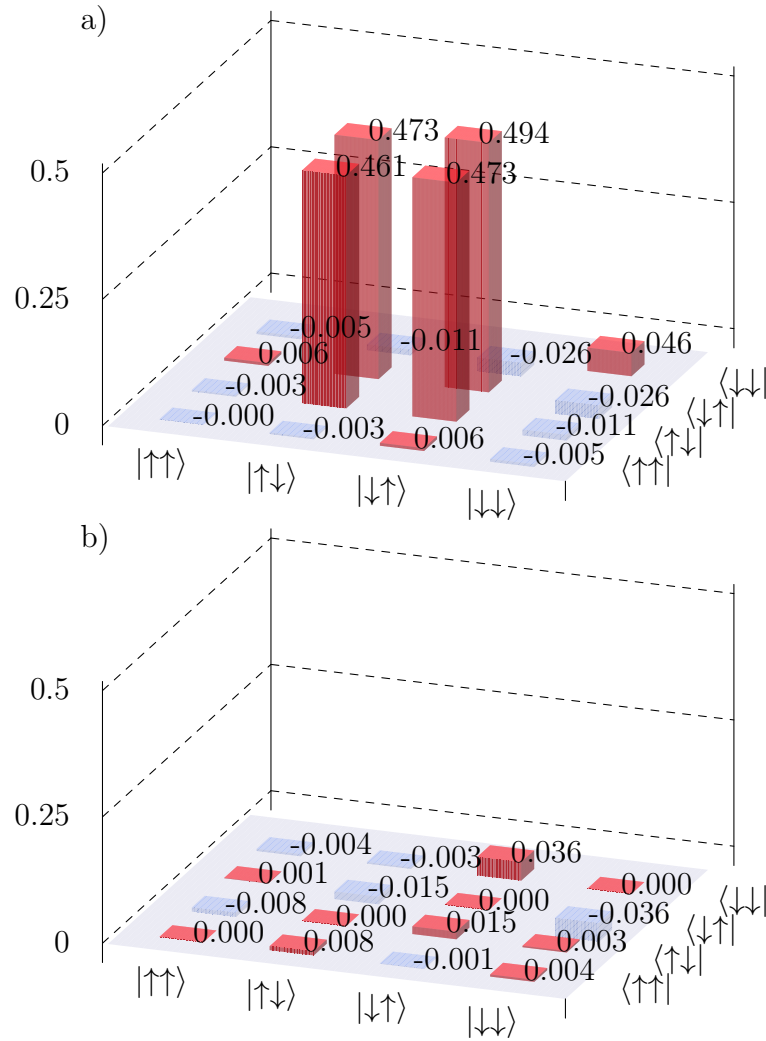


**Figure 4.11:** Measured (a) real  $\Re(\hat{\rho})$  and (b) imaginary  $\Im(\hat{\rho})$  part of the density matrix  $\hat{\rho}$  of the joined atom-photon state. The similarity with the expected state (1.19) can be seen, especially the four components in the center of the real part of the matrix. These values are 0.5 in the ideal case.

with correlations  $\langle \hat{\sigma}_k \otimes \hat{\sigma}_l \rangle = \langle \hat{\sigma}_{k,l} \rangle$ . Hence for measuring the density matrix all the correlations have to be determined. These can be inferred from the expectation values of the projective measurements as

$$\langle \hat{\sigma}_{0,0} \rangle = 1 \quad (4.11a)$$

$$\langle \hat{\sigma}_{0,k} \rangle = \frac{1}{3} \sum_{l=1}^3 \frac{N_{l,k}^{\uparrow\uparrow} + N_{l,k}^{\downarrow\uparrow} - N_{l,k}^{\uparrow\downarrow} - N_{l,k}^{\downarrow\downarrow}}{N_{l,k}^{\uparrow\uparrow} + N_{l,k}^{\downarrow\uparrow} + N_{l,k}^{\uparrow\downarrow} + N_{l,k}^{\downarrow\downarrow}} \quad (4.11b)$$

$$\langle \hat{\sigma}_{k,0} \rangle = \frac{1}{3} \sum_{l=1}^3 \frac{N_{k,l}^{\uparrow\uparrow} + N_{k,l}^{\uparrow\downarrow} - N_{k,l}^{\downarrow\uparrow} - N_{k,l}^{\downarrow\downarrow}}{N_{k,l}^{\uparrow\uparrow} + N_{k,l}^{\downarrow\uparrow} + N_{k,l}^{\uparrow\downarrow} + N_{k,l}^{\downarrow\downarrow}} \quad (4.11c)$$

$$\langle \hat{\sigma}_{l,k} \rangle = \frac{N_{l,k}^{\uparrow\uparrow} - N_{l,k}^{\uparrow\downarrow} - N_{l,k}^{\downarrow\uparrow} + N_{l,k}^{\downarrow\downarrow}}{N_{l,k}^{\uparrow\uparrow} + N_{l,k}^{\downarrow\uparrow} + N_{l,k}^{\uparrow\downarrow} + N_{l,k}^{\downarrow\downarrow}} \quad (4.11d)$$

where e.g.  $N_{l,k}^{\uparrow\downarrow}$  is the number of events, when the atom is found in the state  $|\uparrow\rangle_l$  and the photon in the state  $|\downarrow\rangle_k$ .  $\langle \hat{\sigma}_{0,0} \rangle$  is set to 1 due to normalization [98]. With the relative frequency

$$p_{l,k}^{a,b} = \frac{N_{l,k}^{a,b}}{\sum_{a,b} N_{l,k}^{a,b}} \quad (4.12)$$

and using eq. (4.11) the density matrix can be expressed in closed-form as

$$\hat{\rho} = \frac{1}{4} \sum_{k,l=1}^3 \sum_{a,b \in \{\uparrow, \downarrow\}}^{\uparrow=0, \downarrow=1} p_{l,k}^{a,b} \left( \frac{1}{3} \hat{\sigma}_0 + (-1)^a \hat{\sigma}_k \right) \otimes \left( \frac{1}{3} \hat{\sigma}_0 + (-1)^b \hat{\sigma}_l \right). \quad (4.13)$$

Further details can be found in [99].

By measuring all correlations (4.11) the density matrix  $\hat{\rho}_{meas} = \Re(\hat{\rho}_{meas}) + i\Im(\hat{\rho}_{meas})$  with

$$\Re(\hat{\rho}_{meas}) = \begin{pmatrix} -0.0003 & -0.0030 & 0.0056 & -0.0055 \\ -0.0030 & 0.4606 & 0.47299 & -0.0113 \\ 0.0056 & 0.47299 & 0.4935 & -0.0265 \\ -0.0055 & -0.0113 & -0.0265 & 0.0461 \end{pmatrix} \quad (4.14a)$$

$$\Im(\hat{\rho}_{meas}) = \begin{pmatrix} 0 & -0.0079 & 0.0008 & -0.0041 \\ 0.0079 & 0 & -0.0150 & -0.0029 \\ -0.0008 & 0.0150 & 0 & 0.0363 \\ 0.0041 & 0.0029 & -0.0363 & 0. \end{pmatrix} \quad (4.14b)$$

is obtained, whose graphical representation is shown in fig. 4.11.

We can write the density matrix of the (ideal) atom-photon state (1.19) as

$$\hat{\rho}_{AP} = |\Psi_{AP}\rangle \langle \Psi_{AP}| = \begin{pmatrix} 0 & 0 & 0 & 0 \\ 0 & \frac{1}{2} & \frac{1}{2} & 0 \\ 0 & \frac{1}{2} & \frac{1}{2} & 0 \\ 0 & 0 & 0 & 0 \end{pmatrix} \quad (4.15)$$

and we can see a high degree of analogy with the measured state (4.14). As for the pure state the four essential elements of the real part (4.14a) are  $\sim 0.5$  and the remaining elements are approximately zero. The same can be seen for the imaginary part ep. (4.14b) where all values are in the vicinity of zero.

To quantify the overlap of the measured atom-photon state  $\hat{\rho}_{meas}$  with the pure state  $|\Psi_{AP}\rangle$ , the fidelity is evaluated as

$$F = \langle \Psi_{AP} | \hat{\rho}_{meas} | \Psi_{AP} \rangle = 0.950 \pm 0.030. \quad (4.16)$$

As the fidelity relative to a maximally entangled state  $F > 1/2$  the atom-photon state is proven to be entangled [100, 101] and the observed fidelity is in good agreement with the predicted maximum fidelity of the Zeeman state read-out in fig. 4.7 and the measured correlations in fig. 4.10.

The error  $\Delta F$  of the fidelity

$$\Delta F = \sqrt{\left(\frac{\partial F}{\partial N_{l,k}^{a,b}}\right)^2 \cdot (\Delta N_{l,k}^{a,b})^2} \quad (4.17)$$

$$= \sqrt{\sum_{l,k=1}^3 \sum_{a,b \in \{\uparrow, \downarrow\}} \frac{N_{l,k}^{a,b}}{(\sum_{a,b} N_{l,k}^{a,b})^2} \cdot \langle \Psi | \hat{\rho}_{meas} | \Psi \rangle^2} \quad (4.18)$$

is determined by the statistical fluctuations of the event rates  $\Delta N_{l,k}^{a,b} = \sqrt{N_{l,k}^{a,b}}$ , while the total event rate for each measurement basis is assumed to be without error.

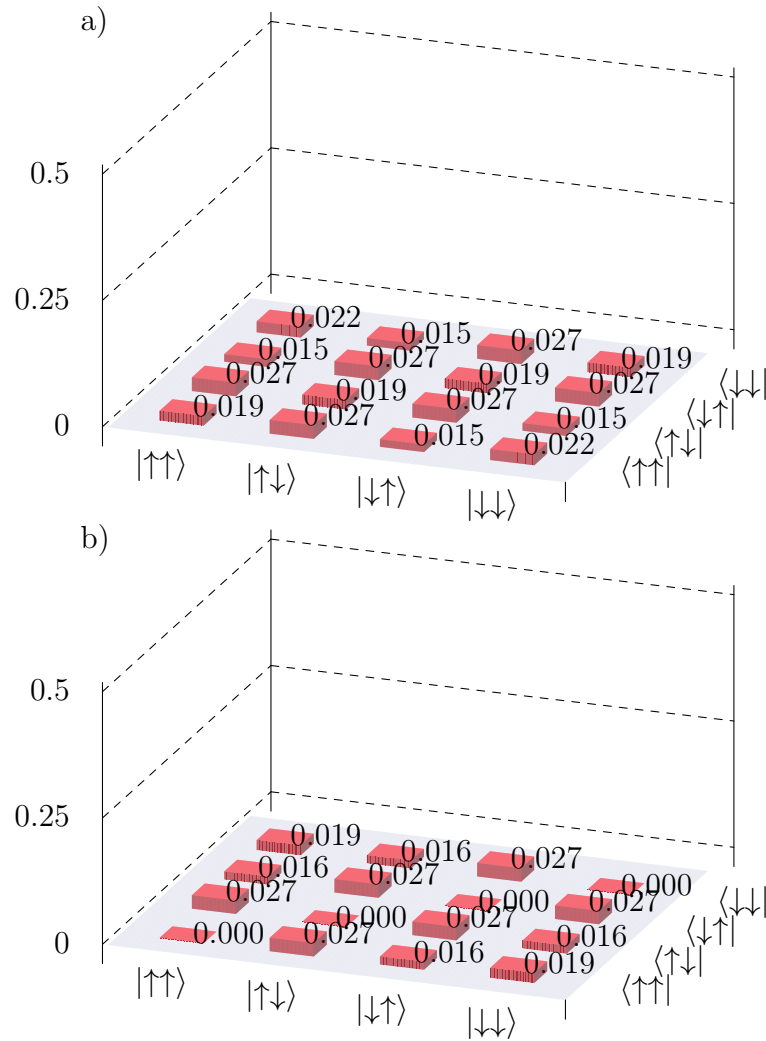


**Figure 4.12:** Statistical  $1\sigma$  errors on each element of the measured density matrix

The statistical error of each density matrix element

$$\begin{aligned}
\Delta \hat{\rho}_{i,j} &= \sqrt{\sum_{k,l=1}^3 \sum_{a,b \in \{\uparrow, \downarrow\}} \left( \frac{\partial \langle i | \hat{\rho}_{meas} | j \rangle}{\partial N_{l,k}^{a,b}} \right)^2 \cdot (\Delta N_{l,k}^{a,b})^2} \\
&= \frac{1}{4} \sqrt{\sum_{k,l=1}^3 \sum_{a,b \in \{\uparrow, \downarrow\}} \frac{N_{l,k}^{a,b}}{(\sum_{a,b} N_{l,k}^{a,b})^2} \times} \\
&\quad \times \sqrt{\left( \langle i | \left( \frac{1}{3} \sigma_0 + (-1)^a \sigma_k \right) \otimes \left( \frac{1}{3} \sigma_0 + (-1)^b \sigma_l \right) | j \rangle \right)^2} \quad (4.19)
\end{aligned}$$

is depicted in fig. 4.12. It can be seen that the error is equally spread over the entire matrix.

The eigenvalues of  $\hat{\rho}_{meas}$  are

$$\lambda_1^{meas} = 0.952 \quad (4.20a)$$

$$\lambda_2^{meas} = 0.0613 \quad (4.20b)$$

$$\lambda_3^{meas} = -0.0152 \quad (4.20c)$$

$$\lambda_4^{meas} = 0.00183 \quad (4.20d)$$

where  $\lambda_3 < 0$  renders the density matrix unphysical due to the fluctuations in the event rates of the correlations (4.11). Using the maximum likelihood estimation [98, 102] a physical density matrix  $\hat{\rho}_{phys}$  that is close to the measured one can be reconstructed, yielding

$$\Re(\hat{\rho}_{phys}) = \begin{pmatrix} 0.0112 & -0.000214 & -0.00417 & -0.00521 \\ -0.000214 & 0.472 & 0.468 & -0.0214 \\ -0.00417 & 0.468 & 0.477 & -0.0213 \\ -0.00521 & -0.0214 & -0.0213 & 0.0391 \end{pmatrix} \quad (4.21a)$$

$$\Im(\hat{\rho}_{phys}) = \begin{pmatrix} 0. & -0.000245 & 0.000194 & -0.00624 \\ 0.000245 & 0. & -0.0116 & -0.000938 \\ -0.000194 & 0.0117 & 0. & 0.0205 \\ 0.00624 & 0.000938 & -0.0205 & 0. \end{pmatrix}. \quad (4.21b)$$

Necessarily,  $\hat{\rho}_{phys}$  has only positive eigenvalues

$$\lambda_1^{ml} = 0.944 \quad (4.22a)$$

$$\lambda_2^{ml} = 0.0464 \quad (4.22b)$$

$$\lambda_3^{ml} = 0.00947 \quad (4.22c)$$

$$\lambda_4^{ml} = 0. \quad (4.22d)$$

and a fidelity of 0.9428.

## 4.4 Summary

In this chapter a new approach on the read-out of an atomic qubit encoded in a Zeeman spin state is described. The dynamics of the system interacting with a single resonant light field and a light field with sufficient energy to ionize the excited atom is calculated using the Lindblad equation. As a first test, the dynamics of a three level system was modeled, yielding a broadening of the  $5^2S_{1/2}, |F = 2\rangle \rightarrow 5^2P_{3/2}, |F' = 3\rangle$  line due to a decreasing life time of the excited state. The next step was the extension of the theoretical model to six levels to describe the ionization of the  $^{87}\text{Rb}$  atom depending on its Zeeman spin state. The results predict a limit on the read-out visibility of 0.961 by the spontaneous decay of the bright state into the dark state, while the atom is excited but not yet ionized together with off-resonant excitation of the dark state. Entanglement between the polarization state of a spontaneously emitted photon and the spin state of the atom is utilized to prepare the atom in arbitrary superpositions of Zeeman states. This can be used to test the read-out procedure and it can be shown, that this procedure is capable to reconstruct the experimental atom-photon state with a fidelity of  $0.950 \pm 0.030$  with an ionization time of  $5 \cdot \tau_{bright} = 89 \pm 2.8$  ns.

# Chapter 5

## Summary and Outlook

In this thesis, a new read-out scheme for an atomic qubit encoded in the Zeeman state of a single  $^{87}\text{Rb}$  atom is investigated. The state detection is based on the state selective excitation and subsequent photo-ionization of the atom. With this scheme, a highly accurate state detection can be implemented in the current experiments for observing atom-photon and atom-atom entanglement. The overall ionization time is less than 100 ns and in combination with two opposing channel electron multipliers [32, 44], a read-out time of less than 1  $\mu\text{s}$  can be achieved. The fidelity for the atom-photon read-out of  $F = 0.950 \pm 0.030$  and the detection efficiency of the ionization fragments of  $\eta_{ion} = 0.991 \pm 0.001$  are sufficient to violate a Bell inequality without relying on the fair sampling assumption as the generation of atom-atom entanglement is heralded by a two photon coincidence [11, 95]. The fast detection procedure requires a distance of the two entangled atoms of 300 m for excluding any local interaction between the two experiments.

The atom trap setup surrounding a UHV chamber is capable of storing a single  $^{87}\text{Rb}$  atom for sufficient time (see p. 20) to perform all the experiments. In combination with the new availability of high power laser diodes for wavelengths of  $\lambda = 450 \text{ nm}$ ,  $\lambda \leq 473 \text{ nm}$  the influence of the ionization laser on the atomic levels could be investigated. Comparing the experimental results with calculations yields good agreement and a light shift for  $\lambda = 450 \text{ nm}$  of  $-0.246 \pm 0.017 \text{ MHz}/\frac{\text{kW}}{\text{mm}^2}$  for the  $5^2S_{1/2}, |F = 2\rangle \rightarrow 5^2P_{3/2}, |F' = 3\rangle$  transition is observed (see p. 37). The ionization procedure opens a new decay channel for the atomic system. This leads to a broadening of the line width of the transition. By modeling the atomic system as a three level system, the broadening of the line width can be explained and good agreement can be seen between the theory and the experimental results (see p. 50). The generation of atom-photon entanglement is utilized for the preparation of arbitrary superposition of the Zeeman manifold of the  $5^2S_{1/2}, |F = 1\rangle$  ground state. The dynamic of the system is modeled by a 6-level Lindblad equation and with this model a maximum read-out contrast of  $v_{theory} = 0.961$  is predicted (see p. 53). To

verify this predictions a full state tomography of the joined atom-photon state is performed and a fidelity of  $F = 0.950 \pm 0.030$  within  $89 \pm 2.8$  ns is obtained (see p. 59).

## 5.1 Combining Zeeman state ionization and Channel electron multipliers

The results presented in this thesis were obtained by using the fluorescence detection method [6, 103] to determine whether the atom was ionized or not. The downside of this method is the long time required to obtain a measurement result (see p. 21) of  $\approx 60$  ms. By combining the ionization based read-out scheme with direct detection of the ionization fragments using [32] the probability to detect the correct state is  $\eta_{corr} = \eta_{ion} \cdot \frac{2}{3}(F + \frac{1}{2}) = 0.9580 \pm 0.0218$ . The measurement can be performed within  $1 \mu\text{s}$  as the time used for the ionisation of the atom is  $t_{ion} = 89 \pm 2.8$  ns, while the detection of the ionization fragments requires  $t_{det} = 415.5$  ns. Within the framework of a loophole-free test of Bell's inequality the residual time is required, e.g., for an arbitrary selection of the measurement bases [31].

## 5.2 Estimations on Loophole-free Test of Bell's Inequality

For the proposed test of Bell's inequality, a sufficient statistical significance of the results is required. The number of detected atoms depends on the quality of the generation of atom-atom entanglement [104], the detection of the ionization fragments [32] and the read-out fidelity of the atomic state. By combining the results obtained so far fig. 5.1 shows the number of required events. We assume a fidelity of the atom-atom entanglement generation of  $0.913 \pm 0.0039$ , a probability to detect at least one ionization fragment of  $0.991 \pm 0.002$ , and the fidelity for the atomic state read-out is  $0.95 \pm 0.03$ . With these values a S parameter of 2.21 can be achieved. 5.1 shows the number of required measurement events depending on the desired statistical significance. 2315 measurement events are required for a significance of three standard deviations.

As the successful generation of a pair of entangled atoms happens with a frequency of 1 per 90 s a measurement time of 58 hours is necessary. As the event rate so far is determined by using only a fiber with a length of 35 m the event rate will drop over the length of 650 m by 40% as the attenuation is specified to be  $-2.34$  dB. This is the length of the new fiber used to connect a new lab with the current setting.

A custom designed microscope objective for collecting the emitted photons from the atom is in preparation to be used to increase the event rate by a factor of 5 to

5.2. ESTIMATIONS ON LOOPHOLE-FREE TEST OF BELL'S INEQUALITY 67

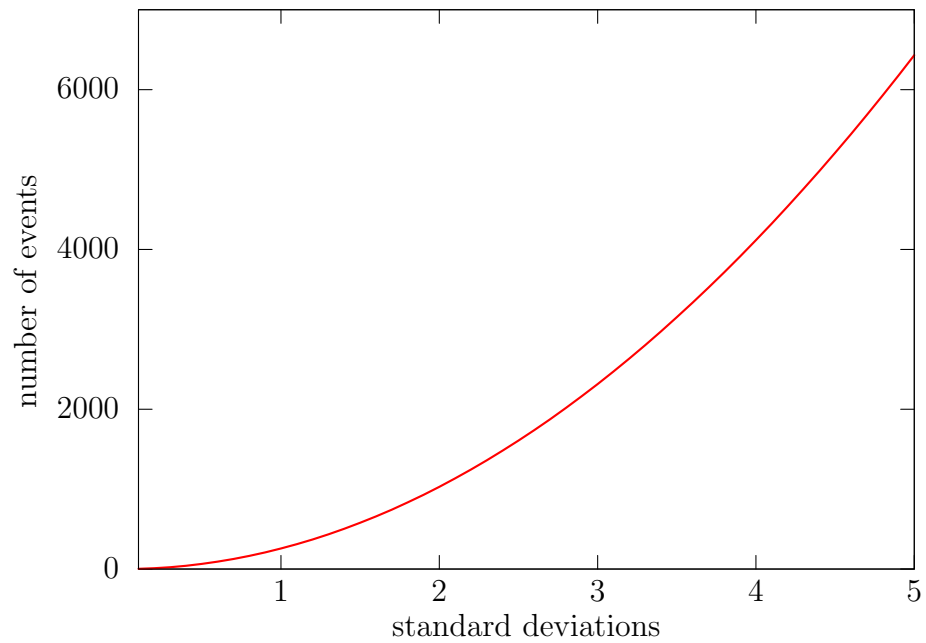


**Figure 5.1:** Required number of events depending on the statistical significance for violating Bell's inequality

10. This will reduce the measurement time and a conclusive test of Bell's inequality seems possible.

### 5.3 Recent Progress

After finishing the experimental work on this thesis the work continued on the experiment. The atomic trap was implemented into the setup of the CEM. With this, the ionization process was investigated in-depth by R. Garthoff and showed a contrast of 0.938 with optimized pulse parameters [105, 106].

The two atomic traps were separated by 398 m and connected via optical fibers. Furthermore the second trap was implemented into the CEM setup. After this modifications a loophole-free test of Bell's inequality was performed. Evaluation of the correlations in the measurement outcomes on both sides yielded an S-value of  $2.221 \pm 0.033$  [107].

# Appendix A

## Data tables

Speed of Light	$c$	299792458 m/s
Permeability (vacuum)	$\mu_0$	$4\pi \cdot 10^{-7}$ N/A <sup>2</sup> 12.566370614 N/A <sup>2</sup>
Permittivity (vacuum)	$\epsilon_0$	8.854187817 F/m
Planck's constant	$h$ $\hbar$	$6.62606957(29) \cdot 10^{-34}$ Js $1.054571726(47) \cdot 10^{-34}$ Js
Elementary Charge	$e$	$1.602176565(35) \cdot 10^{-19}$ C
Electron Mass	$m_e$	$9.10938291(40) \cdot 10^{-31}$ kg
Proton Mass	$m_p$	$1.672621777(74) \cdot 10^{-27}$ kg
Boltzmann constant	$k_B$	$1.3806488(13) \cdot 10^{-23}$ J/K
Electron Volt ( $e/C$ ) J	$eV$	$1.602176565(35) \cdot 10^{-19}$ J
(unified) atomic mass unit $\frac{1}{12}m(^{12}C)$	$u$	$1.660538921(73) \cdot 10^{-27}$ kg

**Table A.1:** Fundamental Physical Constants [108]

Atomic Number	$Z$	37
Total Nucleons	$Z + N$	87
Nuclear Spin	$I$	3/2
Atomic Mass	$m$	86.909180520(15) u $1.443160648(72) \cdot 10^{-25}$ kg
Ionization Limit	$E_I$	4.17712706(10) eV
Ionization wavelength	$\lambda_I$	296.817 nm

**Table A.2:** <sup>87</sup>Rb Physical Properties [74]

Ionization cross section $\sigma_p(\text{m}^2)$	wavelength nm	ref.
$(1.3 \pm 0.1) \cdot 10^{-21}$	406.7	[92]
$(1.4 \pm 0.1) \cdot 10^{-21}$	413.1	[92]
$(1.1 \pm 0.3) \cdot 10^{-21}$	425.6	[109]
$(1.0 \pm 0.3) \cdot 10^{-21}$	440	[91]
$(1.5 \pm 0.2) \cdot 10^{-21}$	476.5	[42]

**Table A.3:** Ionization cross-section of the  $5^2P_{3/2}$  state of  $^{87}\text{Rb}$  for different wavelengths.

Frequency	$\omega_0$	$2\pi \cdot 384.2304844685(62)$ THz
Transition energy	$\hbar\omega_0$	1.589049462(38) eV
Wavelength (vacuum)	$\lambda$	780.241209686(13) nm
Wavelength (air)	$\lambda_{\text{air}}$	780.033330(23) nm
Life time	$\tau$	26.2348(77) ns
Decay Rate	$\Gamma$	$38.117(11) \times 10^6 \text{ s}^{-1}$
Natural line width (FWHM)		$2\pi \cdot 6.0666(18)$ MHz
Doppler temperature	$T_D$	145.57 $\mu\text{K}$

**Table A.4:**  $^{87}\text{Rb}$  D<sub>2</sub> Transition Optical Properties

Wavelength	waist $w_0$	Rayleigh range $z_R$	Transmission
856 nm	$1.94 \pm 0.03 \mu\text{m}$	$13.8 \pm 0.4 \mu\text{m}$	0.58
780 nm	$1.19 \pm 0.04 \mu\text{m}$	$5.7 \pm 0.4 \mu\text{m}$	0.70
473 nm	$1.13 \pm 0.03 \mu\text{m}$	$8.5 \pm 0.4 \mu\text{m}$	0.81

**Table A.5:** Optical properties of the confocal microscope [81]

# Appendix B

## Six-Level system

In the Lindblad eq. (4.4)

$$\dot{\rho}(t) = \hat{\mathcal{L}}(t)$$

for the six level system the single elements for  $\hat{\mathcal{L}}(t) = \sum_{i,j}^n l_{i,j}(t)$  are

$$l_{1,1} = \frac{\imath}{2} (\rho_{1,2}\Omega_{2,1} - \rho_{2,1}\Omega_{1,2}) + \rho_{2,2}\gamma_{1,2} \quad (\text{B.1a})$$

$$l_{1,2} = -\rho_{1,2}(\gamma_{1,2} + \gamma_{3,2} + \gamma_{4,2} + \gamma_{5,2}) + \frac{\imath}{2} [\rho_{1,4}\Omega_{2,1} + \Omega_{1,2}(\rho_{1,1} - \rho_{2,2})] \quad (\text{B.1b})$$

$$l_{1,3} = -\frac{\imath}{2}\Omega_{1,2}\rho_{2,3} \quad (\text{B.1c})$$

$$l_{1,4} = \frac{\imath}{2} (\rho_{1,2}\Omega_{2,1} - \rho_{2,4}\Omega_{1,2}) - \imath\delta_4\rho_{1,4} \quad (\text{B.1d})$$

$$l_{1,5} = \frac{\imath}{2} (\rho_{1,6}\Omega_{6,5} - \rho_{2,5}\Omega_{1,2}) \quad (\text{B.1e})$$

$$l_{1,6} = \frac{\imath}{2} (\rho_{1,5}\Omega_{5,6} - \rho_{2,6}\Omega_{1,2}) - \frac{1}{2}\rho_{1,6}(\gamma_{3,6} + \gamma_{5,6}) \quad (\text{B.1f})$$

$$l_{2,1} = -\frac{1}{2} [\rho_{2,1}(\gamma_{1,2} + \gamma_{3,2} + \gamma_{4,2} + \gamma_{5,2}) + i\Omega_{2,1}(\rho_{1,1} - \rho_{2,2} + \rho_{4,1})] \quad (\text{B.2a})$$

$$l_{2,2} = -\rho_{2,2}(\gamma_{1,2} + \gamma_{3,2} + \gamma_{4,2} + \gamma_{5,2}) + \frac{i}{2} [\rho_{2,1}\Omega_{1,2} - \Omega_{2,1}(\rho_{1,2} - \rho_{2,4} + \rho_{4,2})] \quad (\text{B.2b})$$

$$l_{2,3} = -\frac{1}{2} [\rho_{2,3}(\gamma_{1,2} + \gamma_{3,2} + \gamma_{4,2} + \gamma_{5,2}) + i\Omega_{2,1}(\rho_{1,3} + \rho_{4,3})] \quad (\text{B.2c})$$

$$l_{2,4} = -\frac{1}{2} [\rho_{2,4}(\gamma_{1,2} + \gamma_{3,2} + \gamma_{4,2} + \gamma_{5,2} + 2i\delta_4) + i\Omega_{2,1}(\rho_{1,4} - \rho_{2,2} + \rho_{4,4})] \quad (\text{B.2d})$$

$$l_{2,5} = -\frac{1}{2}(\gamma_{1,2} + \gamma_{3,2} + \gamma_{4,2} + \gamma_{5,2})\rho_{2,5} + \frac{i}{2} [\rho_{2,6}\Omega_{6,5} - \Omega_{2,1}(\rho_{1,5} + \rho_{4,5})] \quad (\text{B.2e})$$

$$l_{2,6} = \frac{i}{2} [\rho_{2,5}\Omega_{5,6} - \Omega_{2,1}(\rho_{1,6} + \rho_{4,6})] - \frac{1}{2}(\gamma_{1,2} + \gamma_{3,2} + \gamma_{3,6} + \gamma_{4,2} + \gamma_{5,2} + \gamma_{5,6})\rho_{2,6} \quad (\text{B.2f})$$

$$l_{3,1} = \frac{i}{2}\rho_{3,2}\Omega_{2,1} \quad (\text{B.3a})$$

$$l_{3,2} = \frac{i}{2} [\rho_{3,1}\Omega_{1,2} + \rho_{3,4}\Omega_{2,1}] - \frac{1}{2}(\gamma_{1,2} + \gamma_{3,2} + \gamma_{4,2} + \gamma_{5,2})\rho_{3,2} \quad (\text{B.3b})$$

$$l_{3,3} = \gamma_{3,2}\rho_{2,2} + \gamma_{3,6}\rho_{6,6} \quad (\text{B.3c})$$

$$l_{3,4} = \frac{i}{2}(\rho_{3,2}\Omega_{2,1} - 2\delta_4\rho_{3,4}) \quad (\text{B.3d})$$

$$l_{3,5} = \frac{i}{2}\rho_{3,6}\Omega_{6,5} \quad (\text{B.3e})$$

$$l_{3,6} = \frac{i}{2} [\rho_{3,5}\Omega_{5,6} - (\gamma_{3,6} + \gamma_{5,6})\rho_{3,6}] \quad (\text{B.3f})$$

$$l_{4,1} = i\delta_4\rho_{4,1} + \frac{i}{2}\Omega_{2,1}(\rho_{4,2} - \rho_{2,1}) \quad (\text{B.4a})$$

$$l_{4,2} = \frac{i}{2} [\rho_{2,4}\Omega_{1,2} + \Omega_{2,1}(\rho_{4,4} - \rho_{2,2})] \quad (\text{B.4b})$$

$$l_{4,3} = \frac{i}{2}(2\delta_4\rho_{4,3} - \rho_{2,3}\Omega_{2,1}) \quad (\text{B.4c})$$

$$l_{4,4} = \gamma_{4,2}\rho_{2,2} - \frac{i}{2}\Omega_{2,1}(\rho_{2,4} - \rho_{4,2}) \quad (\text{B.4d})$$

$$l_{4,5} = \frac{i}{2}(\rho_{4,6}\Omega_{6,5} - \rho_{2,5}\Omega_{2,1} + 2\delta_4\rho_{4,5}) \quad (\text{B.4e})$$

$$l_{4,6} = \frac{i}{2}(\rho_{4,5}\Omega_{5,6} - \rho_{2,6}\Omega_{2,1}) - \frac{1}{2}(\gamma_{3,6} + \gamma_{5,6} - 2i\delta_4\rho_{4,6}) \quad (\text{B.4f})$$

$$l_{5,1} = \frac{i}{2}(\rho_{5,2}\Omega_{2,1} - \rho_{6,1}\Omega_{5,6}) \quad (\text{B.5a})$$

$$l_{5,2} = \frac{i}{2}(\rho_{5,1}\Omega_{1,2} + \rho_{5,4}\Omega_{2,1} - \rho_{6,2}\Omega_{5,6}) - \frac{1}{2}(\gamma_{1,2} + \gamma_{3,2} + \gamma_{4,2} + \gamma_{5,2})\rho_{5,2} \quad (\text{B.5b})$$

$$l_{5,3} = -\frac{i}{2}\rho_{6,3}\Omega_{5,6} \quad (\text{B.5c})$$

$$l_{5,4} = \frac{i}{2}(\rho_{5,2}\Omega_{2,1} - \rho_{6,4}\Omega_{5,6} - 2\delta_4\rho_{5,4}) \quad (\text{B.5d})$$

$$l_{5,5} = \gamma_{5,2}\rho_{2,2} + \gamma_{5,6}\rho_{6,6} + \frac{i}{2}(\rho_{5,6}\Omega_{6,5} - \rho_{6,5}\Omega_{5,6}) \quad (\text{B.5e})$$

$$l_{5,6} = \frac{i}{2}\Omega_{5,6}(\rho_{5,5} - \rho_{6,6}) - \frac{1}{2}(\gamma_{3,4} + \gamma_{5,6})\rho_{5,6} \quad (\text{B.5f})$$

$$l_{6,1} = \frac{i}{2}(\Omega_{2,1}\rho_{6,2} - \rho_{5,1}\Omega_{6,5}) - \frac{1}{2}(\gamma_{3,6} + \gamma_{5,6})\rho_{6,1} \quad (\text{B.6a})$$

$$l_{6,2} = \frac{i}{2}(\Omega_{1,2}\rho_{6,1} + \Omega_{2,1}\rho_{6,4} - \Omega_{6,5}\rho_{5,2}) - \frac{1}{2}(\gamma_{1,2} + \gamma_{3,2} + \gamma_{3,6} + \gamma_{4,2} + \gamma_{5,2} + \gamma_{5,6})\rho_{6,2} \quad (\text{B.6b})$$

$$l_{6,3} = -\frac{i}{2}\rho_{5,3}\Omega_{6,5} - \frac{1}{2}(\gamma_{3,6} + \gamma_{5,6})\rho_{6,3} \quad (\text{B.6c})$$

$$l_{6,4} = \frac{i}{2}(\rho_{6,2}\Omega_{2,1} - \rho_{5,4}\Omega_{6,5}) - \frac{1}{2}(\gamma_{3,6} + \gamma_{5,6} + 2i\delta_4)\rho_{6,4} \quad (\text{B.6d})$$

$$l_{6,5} = \frac{i}{2}\Omega_{6,5}(\rho_{6,6} - \rho_{5,5}) - \frac{1}{2}(\gamma_{3,6} + \gamma_{5,6})\rho_{6,5} \quad (\text{B.6e})$$

$$l_{6,6} = \frac{i}{2}(\rho_{6,5}\Omega_{5,6} - \rho_{5,6}\Omega_{6,5}) - (\gamma_{3,6} + \gamma_{5,6})\rho_{6,6} \quad (\text{B.6f})$$



# Appendix C

## Pulse Sequence

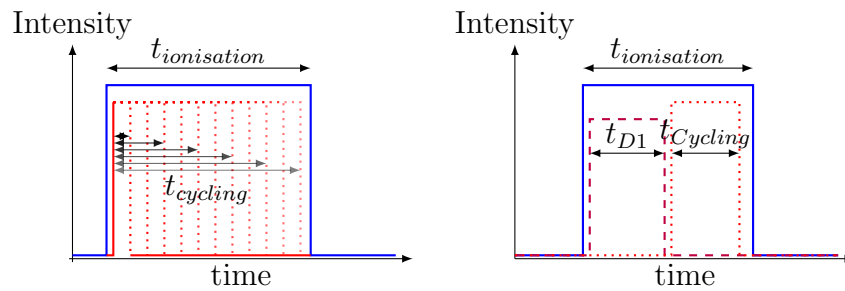


**Figure C.1:** Pulse sequence for hyperfine state dependent ionization. The length of the cycling pulse can be varied while the ionization pulse is fixed in length. For the light shift measurements the intensity of the blue laser is varied while the Cycling laser intensity is kept constant but its frequency is varied.



# Appendix D

## ac-Stark shift calculated values

$m_F$	-3	-2	-1	0	1	2	3
$F' = 3$	78.47	76.10	78.95	87.03	100.3	118.9	142.6
$F' = 2$		77.21	87.34	97.67	108.2	118.9	
$F' = 1$			82.49	108.9	102.9		
$F' = 0$				98.22			
$F = 2$		52.30	52.13	51.96	51.78	51.61	
$F = 1$			51.79	51.95	52.13		

**Table D.1:** Values of the calculated light shift induced by a  $\sigma^-$  polarized laser at a wavelength of 450 nm and an intensity of 85.2 kW/mm<sup>2</sup> used for photo-ionization. The upper row are the data for the  $5^2P_{3/2}$  state while the lower row is for the ground state  $5^2S_{1/2}$ .

$m_F$	-3	-2	-1	0	1	2	3
$F' = 3$	142.6	118.9	100.3	87.02	78.95	76.10	78.47
$F' = 2$		118.9	108.2	97.67	87.34	77.20	
$F' = 1$			102.9	108.9	82.49		
$F' = 0$				98.2			
$F = 2$		51.61	51.78	51.96	52.13	52.30	
$F = 1$			52.13	51.96	51.79		

**Table D.2:** Values of the calculated light shift induced by a  $\sigma^+$  polarized laser at a wavelength of 450 nm and an intensity of 85.2 kW/mm<sup>2</sup> used for photo-ionization. The upper row are the data for the  $5^2P_{3/2}$  state while the lower row is for the ground state  $5^2S_{1/2}$ .

$m_F$	-3	-2	-1	0	1	2	3
$F' = 3$	71.35	76.90	80.23	81.34	80.23	76.90	71.35
$F' = 2$		76.90	78.01	78.38	78.01	76.90	
$F' = 1$			80.97	72.46	80.97		
$F' = 0$				78.38			
$F = 2$		51.96	51.96	51.96	51.96	51.96	
$F = 1$			51.96	51.96	51.96		

**Table D.3:** Values of the calculated light shift induced by a  $\pi$  polarized laser at a wavelength of 450 nm and an intensity of 85.2 kW/mm<sup>2</sup> used for photo-ionization. The upper row are the data for the  $5^2P_{3/2}$  state while the lower row is for the ground state  $5^2S_{1/2}$ .

$m_F$	-3	-2	-1	0	1	2	3
$F' = 3$	14.88	12.40	9.511	6.232	2.558	-1.511	-5.974
$F' = 2$		12.40	8.919	5.544	2.271	-0.8994	
$F' = 1$			9.314	5.162	2.870		
$F' = 0$				5.850			
$F = 2$		-30.14	-29.01	-27.87	-26.73	-25.60	
$F = 1$			-26.73	-27.86	-28.99		

**Table D.4:** Values of the calculated light shift induced by a  $\pi$  polarized laser at a wavelength of 856 nm and an intensity of 2.94 kW/mm<sup>2</sup> used for optical dipole trap. The upper row are the data for the  $5^2P_{3/2}$  state while the lower row is for the ground state  $5^2S_{1/2}$ .

$m_F$	-3	-2	-1	0	1	2	3
$F' = 3$	-5.974	-1.511	2.558	6.232	9.511	12.40	14.88
$F' = 2$		-0.8994	2.271	5.544	8.919	12.40	
$F' = 1$			2.870	5.162	9.314		
$F' = 0$				5.850			
$F = 2$		-25.60	-26.73	-27.87	-29.01	-30.14	
$F = 1$			-28.99	-27.86	-26.73		

**Table D.5:** Values of the calculated light shift induced by a  $\pi$  polarized laser at a wavelength of 856 nm and an intensity of 2.94 kW/mm<sup>2</sup> used for optical dipole trap. The upper row are the data for the  $5^2P_{3/2}$  state while the lower row is for the ground state  $5^2S_{1/2}$ .

$m_F$	-3	-2	-1	0	1	2	3
$F' = 3$	7.416	14.20	18.27	19.62	18.27	14.20	7.416
$F' = 2$		14.20	16.17	16.82	16.17	14.20	
$F' = 1$			20.19	8.773	20.19		
$F' = 0$				16.82			
$F = 2$		-27.87	-27.87	-27.87	-27.87	-27.87	
$F = 1$			-27.86	-27.86	-27.86		

**Table D.6:** Values of the calculated light shift induced by a  $\pi$  polarized laser at a wavelength of 856 nm and an intensity of 2.94 kW/mm<sup>2</sup> used for optical dipole trap. The upper row are the data for the  $5^2P_{3/2}$  state while the lower row is for the ground state  $5^2S_{1/2}$ .



# Bibliography

- [1] E. Schrödinger. Discussion of probability relations between separated systems. *Mathematical Proceedings of the Cambridge Philosophical Society*, 31:555–563, 9 1935.
- [2] Michael A. Nielsen and Isaac L. Chuang. *Quantum Computation and Quantum Information (Cambridge Series on Information and the Natural Sciences)*. Cambridge University Press, 1 edition, January 2004.
- [3] Samuel L. Braunstein, A. Mann, and M. Revzen. Maximal violation of bell inequalities for mixed states. *Phys. Rev. Lett.*, 68:3259–3261, Jun 1992.
- [4] U. Fano. Description of states in quantum mechanics by density matrix and operator techniques. *Rev. Mod. Phys.*, 29:74–93, Jan 1957.
- [5] Hans-Otto Georgii. *Stochastik, Einführung in die Wahrscheinlichkeitstheorie und Statistik*. e Gruyter, erlin, Boston, 2009.
- [6] Jürgen Volz, Markus Weber, Daniel Schlenk, Wenjamin Rosenfeld, Johannes Vrana, Karen Saucke, Christian Kurtsiefer, and Harald Weinfurter. Observation of entanglement of a single photon with a trapped atom. *Physical Review Letters*, 96(3):030404, 2006.
- [7] W. Rosenfeld. *Experiments with an Entangled System of a Single Atom and a Single Photon*. PhD thesis, Ludwig-Maximilians-Universität München, 2008.
- [8] M. Żukowski, A. Zeilinger, M. A. Horne, and A. K. Ekert. “event-ready-detectors” bell experiment via entanglement swapping. *Phys. Rev. Lett.*, 71:4287–4290, Dec 1993.
- [9] H. Weinfurter. Experimental bell-state analysis. *EPL (Europhysics Letters)*, 25(8):559, 1994.
- [10] C. K. Hong, Z. Y. Ou, and L. Mandel. Measurement of subpicosecond time intervals between two photons by interference. *Phys. Rev. Lett.*, 59:2044–2046, Nov 1987.

- [11] J. Hofmann, M. Krug, N. Ortegel, L. Gérard, M. Weber, W. Rosenfeld, and H. Weinfurter. Heralded entanglement between widely separated atoms. *Science*, 2012.
- [12] A. Einstein, B. Podolsky, and N. Rosen. Can Quantum-Mechanical Description of Physical Reality Be Considered Complete? *Phys. Rev.*, 47(10):777–780, May 1935.
- [13] F. Kröner. Albert einstein, philosopher-scientist. *Dialectica*, 7(1):61–69, 1953.
- [14] D. Bohm and Y. Aharonov. Discussion of Experimental Proof for the Paradox of Einstein, Rosen, and Podolsky. *Phys. Rev.*, 108(4):1070–1076, Nov 1957.
- [15] J. S. Bell. On the Einstein-Podolsky-Rosen paradox. *Physics*, 1964:195, 1964.
- [16] D. Dürr. *Bohmsche Mechanik Als Grundlage Der Quantenmechanik*. Springer-Verlag GmbH, 2001.
- [17] J. F. Clauser, M. A. Horne, A. Shimony, and R. A. Holt. Proposed experiment to test local hidden-variable theories. *Phys. Rev. Lett.*, 23:880–884, 1969.
- [18] A. Aspect, P. Grangier, and G. Roger. Experimental tests of realistic local theories via Bell’s theorem. *Phys. Rev. Lett.*, 47:460–463, 1981.
- [19] A. Aspect, P. Grangier, and G. Roger. Experimental realisation of Einstein-Podolski-Rosen-Bohm Gedankenexperiment: A new violation of Bell’s inequality. *Phys. Rev. Lett.*, 49:91–94, 1982.
- [20] A. Aspect, J. Dalibard, and G. Roger. Experimental test of Bell’s inequality using time-varying analyser. *Phys. Rev. Lett.*, 49:1804–1807, 1982.
- [21] Gregor Weihs, Thomas Jennewein, Christoph Simon, Harald Weinfurter, and Anton Zeilinger. Violation of bell’s inequality under strict einstein locality conditions. *Phys. Rev. Lett.*, 81:5039–5043, Dec 1998.
- [22] M. A. Rowe, D. Kielpinsky, V. Meyer, C.A. Sacket, W. M. Itano, C. Monroe, and Wineland D.J. Experimental violation of Bell’s inequality with efficient detection. *Nature*, 409:791–794, 2001.
- [23] Markus Ansmann, H. Wang, Radoslaw C. Bialczak, Max Hofheinz, Erik Lucero, M. Neeley, A. D. O’Connell, D. Sank, M. Weides, J. Wenner, A. N. Cleland, and John M. Martinis. Violation of bell’s inequality in josephson phase qubits. *Nature*, 461(7263):504–506, September 2009.

- [24] Thomas Scheidl, Rupert Ursin, Johannes Kofler, Sven Ramelow, Xiao-Song Ma, Thomas Herbst, Lothar Ratschbacher, Alessandro Fedrizzi, Nathan K. Langford, Thomas Jennewein, and Anton Zeilinger. Violation of local realism with freedom of choice. *Proceedings of the National Academy of Sciences*, 107(46):19708–19713, 2010.
- [25] Marissa Giustina, Alexandra Mech, Sven Ramelow, Bernhard Wittmann, Johannes Kofler, Jorn Beyer, Adriana Lita, Brice Calkins, Thomas Gerrits, Sae Woo Nam, Rupert Ursin, and Anton Zeilinger. Bell violation using entangled photons without the fair-sampling assumption. *Nature*, 497(7448):227–230, May 2013.
- [26] B. G. Christensen, K. T. McCusker, J. B. Altepeter, B. Calkins, T. Gerrits, A. E. Lita, A. Miller, Y. Shalm, L. K. Zhang, S. W. Nam, N. Brunner, C. C. W. Lim, N. Gisin, and P. G. Kwiat. Detection-loophole-free test of quantum nonlocality, and applications. *arXiv:1306.5772*, 2013.
- [27] Philip M. Pearle. Hidden-variable example based upon data rejection. *Phys. Rev. D*, 2:1418–1425, Oct 1970.
- [28] J F Clauser and A Shimony. Bell’s theorem. experimental tests and implications. *Reports on Progress in Physics*, 41(12):1881, 1978.
- [29] Marek Zukowski. private communication, 2013.
- [30] Paul G. Kwiat, Philippe H. Eberhard, Aephraim M. Steinberg, and Raymond Y. Chiao. Proposal for a loophole-free bell inequality experiment. *Phys. Rev. A*, 49:3209–3220, May 1994.
- [31] Wenjamin Rosenfeld, Markus Weber, Jürgen Volz, Florian Henkel, Michael Krug, Adan Cabello, Marek Zukowski, and Harald Weinfurter. Towards a loophole-free test of bell’s inequality with entangled pairs of neutral atoms. *Advanced Science Letters*, 2(4):469–474, 2009.
- [32] F. Henkel. *Photoionisation detection of single  $^{87}\text{Rb}$  -atoms using channel electron multipliers*. PhD thesis, Ludwig-Maximilians-Universität, München, 2011.
- [33] Hermann Haken and Hans C. Wolf. *The Physics of Atoms and Quanta: Introduction to Experiments and Theory (Advanced Texts in Physics)*. Springer, 6th rev. and enlarged ed. edition, October 2000.
- [34] H. Hertz. Ueber einen einfluss des ultravioletten lichtes auf die electrische entladung. *Annalen der Physik*, 267(8):983–1000, 1887.

- [35] Wilhelm Hallwachs. Ueber die electrisirung von metallplatten durch bestrahlung mit electrischem licht. *Annalen der Physik*, 270(8A):731–734, 1888.
- [36] P. Lenard. Erzeugung von kathodenstrahlen durch ultravioletes licht. *Annalen der Physik*, 307(6):359–375, 1900.
- [37] A. Einstein. Über einen die erzeugung und verwandlung des lichtet betreffenden heuristischen gesichtspunkt. *Annalen der Physik*, 322(6):132–148, 1905.
- [38] Max Planck. Ueber das gesetz der energieverteilung im normalspectrum. *Annalen der Physik*, 309(3):553–563, 1901.
- [39] John M. Blatt and L. C. Biedenharn. The angular distribution of scattering and reaction cross sections. *Rev. Mod. Phys.*, 24:258–272, Oct 1952.
- [40] Miron Y. Amusja. *Atomic photoeffect*. Plenum Press, New York, 1990.
- [41] Anthony Starace. Photoionization of Atoms Springer Handbook of Atomic, Molecular, and Optical Physics. In Gordon Drake, editor, *Springer Handbook of Atomic, Molecular, and Optical Physics*, chapter 24, pages 379–390. Springer New York, New York, NY, 2006.
- [42] C. Gabbanini, S. Gozzini, and A. Lucchesini. Photoionization cross section measurement in a rb vapor cell trap. *Optics Communications*, 141(1–2):25 – 28, 1997.
- [43] G Mainfray and G Manus. Multiphoton ionization of atoms. *Reports on Progress in Physics*, 54(10):1333, 1991.
- [44] F. Henkel, M. Krug, J. Hofmann, W. Rosenfeld, M. Weber, and H. Weinfurter. Highly efficient state-selective submicrosecond photoionization detection of single atoms. *Phys. Rev. Lett.*, 105:253001, Dec 2010.
- [45] L. Ricci, M. Weidemüller, T. Esslinger, A. Hemmerich, C. Zimmermann, V. Vuletic, W. König, and T.W. Hänsch. A compact grating-stabilized diode laser system for atomic physics. *Optics Communications*, 117:541–549, 1995.
- [46] Paul Horowitz and Winfield Hill. *The art of electronics*. Cambridge University Press, second edition, 1989.
- [47] Michael Krug. Atomic traps for efficient state detection of a single atom. Master’s thesis, May 2007.
- [48] Norbert Ortegel. Atom-photon entanglement. Master’s thesis, 2009.

- [49] Mathias Müller. Schnelle detektion von atomzuständen. Master's thesis, Ludwig-Maximilians-Universität München, February 2011.
- [50] Kai Redeker. Detektion von ionisationsfragmenten von  $^{87}\text{Rb}$ -atomen. Master's thesis, Ludwig-Maximilians-Universität München, 2012.
- [51] E. L. Raab, M. Prentiss, Alex Cable, Steven Chu, and D. E. Pritchard. Trapping of neutral sodium atoms with radiation pressure. *Phys. Rev. Lett.*, 59:2631–2634, Dec 1987.
- [52] C. D. Wallace, T. P. Dinneen, K. Y. N. Tan, A. Kumarakrishnan, P. L. Gould, and J. Javanainen. Measurements of temperature and spring constant in a magneto-optical trap. *J. Opt. Soc. Am. B*, 11(5):703–711, May 1994.
- [53] H. J. Metcalf and P. van Straten. *Laser Cooling and Trapping*. Springer, New York, Berlin, Heidelberg, 1999.
- [54] K. Saucke. Optische Dipolfalle für Einzelatome. Master's thesis, Ludwig-Maximilians-Universität München, 2002.
- [55] M. Weber. *Quantum optical experiments towards atom-photon entanglement*. PhD thesis, Ludwig-Maximilians-Universität München, 2005.
- [56] J. Volz. *Atom-photon entanglement*. PhD thesis, Ludwig-Maximilians-Universität München, 2006.
- [57] P. Hamilton, G. Kim, T. Joshi, B. Mukherjee, D. Tiarks, and H. Müller. Sisyphus Cooling of Lithium. *ArXiv e-prints*, August 2013.
- [58] Buijs Ballot. Akustische versuche auf der niederländischen eisenbahn, nebst gelegentlichen bemerkungen zur theorie des hrn. prof. doppler. *Annalen der Physik*, 142(11):321–351, 1845.
- [59] Steven Chu, L. Hollberg, J. E. Bjorkholm, Alex Cable, and A. Ashkin. Three-dimensional viscous confinement and cooling of atoms by resonance radiation pressure. *Phys. Rev. Lett.*, 55:48–51, Jul 1985.
- [60] T.W. Hänsch and A.L. Schawlow. Cooling of gases by laser radiation. *Optics Communications*, 13(1):68 – 69, 1975.
- [61] Paul D. Lett, Richard N. Watts, Christoph I. Westbrook, William D. Phillips, Phillip L. Gould, and Harold J. Metcalf. Observation of atoms laser cooled below the doppler limit. *Phys. Rev. Lett.*, 61:169–172, Jul 1988.

- [62] J. Dalibard and C. Cohen-Tannoudji. Laser cooling below the doppler limit by polarization gradients: simple theoretical models. *J. Opt. Soc. Am. B*, 6(11):2023–2045, Nov 1989.
- [63] N. Schlosser, G. Reymond, and P. Grangier. Collisional blockade in microscopic optical dipole traps. *Phys. Rev. Lett.*, 89:023005, Jun 2002.
- [64] T. A. Savard, K. M. O’Hara, and J. E. Thomas. Laser-noise-induced heating in far-off resonance optical traps. *Phys. Rev. A*, 56:R1095–R1098, Aug 1997.
- [65] C. Cohen-Tannoudji, J. Dupont-Roc, and G. Grynberg. *Atom-Photon Interactions, Basic Processes and Applications*. Wiley, New York, 1998.
- [66] H.A. Lorentz. The width of spectral lines. *Proceedings of Royal Netherlands Academy of Arts and Sciences (KNAW)*, 18 I:134–150, 1915.
- [67] Marlan O. Scully and Muhammad Suhail Zubairy. *Quantum optics*. University Press, 1997.
- [68] J. J. Sakurai. *Modern Quantum Mechanics (Revised Edition)*. Addison Wesley, 1 edition, September 1993.
- [69] F. J. Dyson. The radiation theories of tomonaga, schwinger, and feynman. *Phys. Rev.*, 75:486–502, Feb 1949.
- [70] V. Weisskopf and E. Wigner. Berechnung der natürlichen linienbreite auf grund der diracschen lichttheorie. *Zeitschrift für Physik*, 63:54–73, 1930.
- [71] M. S. Safronova and U. I. Safronova. Critically evaluated theoretical energies, lifetimes, hyperfine constants, and multipole polarizabilities in  $^{87}\text{Rb}$ . *Phys. Rev. A*, 83:052508, May 2011.
- [72] A. Kramida, Yu. Ralchenko, J. Reader, and NIST ASD Team. Nist atomic spectra database. Online, Nov. 2012.
- [73] R.L. Kurucz and B. Bell. *Atomic Line Data*. Smithsonian Astrophysical Observatory, Cambridge, Mass., 1995.
- [74] Daniel A. Steck. Rubidium 87 d line data (revision 2.1.4). <http://steck.us/alkalidata>, December 2010.
- [75] Tey Meng Khoon. *Interfacing Light and a Single Quantum System with a Lens*. PhD thesis, National University of Singapore, 2009.

- [76] Fam Le Kien, Philipp Schneeweiss, and Arno Rauschenbeutel. Dynamical polarizability of atoms in arbitrary light fields: general theory and application to cesium. *The European Physical Journal D*, 67(5):1–16, 2013.
- [77] Robert C. Hilborn. Einstein coefficients, cross sections, f values, dipole moments, and all that. *American Journal of Physics*, 50(11):982–986, 1982.
- [78] Optical Society Of America. *Handbook of Optics, Vol. 2: Devices, Measurements, and Properties*. McGraw-Hill Professional, 2 edition, September 1994.
- [79] Thomas Williams, Colin Kelley, and many others. Gnuplot 4.6: an interactive plotting program. <http://gnuplot.sourceforge.net/>, 2012.
- [80] A. Einstein. Zur Quantentheorie der Strahlung. *Physikalische Zeitschrift*, 18:121–128, 1917.
- [81] Andreas Deeg. Zustandsdetektion eines einzelnen atoms. Master’s thesis, 2008.
- [82] Warren Nagourney, Jon Sandberg, and Hans Dehmelt. Shelved optical electron amplifier: Observation of quantum jumps. *Phys. Rev. Lett.*, 56:2797–2799, Jun 1986.
- [83] D. J. Wineland, J. C. Bergquist, Wayne M. Itano, and R. E. Drullinger. Double-resonance and optical-pumping experiments on electromagnetically confined, laser-cooled ions. *Opt. Lett.*, 5(6):245–247, Jun 1980.
- [84] K. Sengstock, U. Sterr, J.H. Müller, V. Rieger, D. Bettermann, and W. Ertmer. Optical ramsey spectroscopy on laser-trapped and thermal mg atoms. *Applied Physics B*, 59(2):99–115, 1994.
- [85] R. Unanyan, M. Fleischhauer, B.W. Shore, and K. Bergmann. Robust creation of an phase-sensitiv probing of superposition states via stimulated Raman adiabatic passage (STIRAP) with degenerate states. *Optics Communications*, 155, 1998.
- [86] H. Carmichael. *An open systems approach to quantum optics*. Springer, 1993.
- [87] M. L. Citron, H. R. Gray, C. W. Gabel, and C. R. Stroud. Experimental study of power broadening in a two-level atom. *Phys. Rev. A*, 16:1507–1512, Oct 1977.
- [88] R. E. Grove, F. Y. Wu, and S. Ezekiel. Measurement of the spectrum of resonance fluorescence from a two-level atom in an intense monochromatic field. *Phys. Rev. A*, 15:227–233, Jan 1977.

- [89] L. Allen and J. H. Eberly. *Optical Resonance and Two-Level Atoms*. Dover Publications, December 1987.
- [90] G. Lindblad. On the generators of quantum dynamical semigroups. *Communications in Mathematical Physics*, 48:119–130, 1976.
- [91] A. N. Klyucharev and V. Y. Sepman. Two-stage photoionization of rubidium. *Optics and Spectroscopy*, 38:712–713, June 1975.
- [92] Timothy P. Dinneen, Christopher D. Wallace, Kit-Yan N. Tan, and Phillip L. Gould. Use of trapped atoms to measure absolute photoionization cross sections. *Opt. Lett.*, 17(23):1706–1708, Dec 1992.
- [93] B. B. Blinov, D. L. Moehring, L.-M. Duan, and C. Monroe. Observation of entanglement between a single trapped atom and a single photon. *Nature*, 428(6979):153–157, March 2004.
- [94] L. Gérard. Spin-state-selective detection of single rubidium atoms. diploma thesis, Ludwig-Maximilians-Universität, 04 2012.
- [95] J. Hofmann. *Heralded Atom-Atom Entanglement*. PhD thesis, Ludwig-Maximilians-Universität, 2014.
- [96] Max Born and Emil Wolf. *Principles of Optics: Electromagnetic Theory of Propagation, Interference and Diffraction of Light*. Cambridge University Press, 7th edition, October 1999.
- [97] Eugene Hecht. *Optics (4th Edition)*. Addison Wesley, 4 edition, August 2001.
- [98] Daniel F. V. James, Paul G. Kwiat, William J. Munro, and Andrew G. White. Measurement of qubits. *Phys. Rev. A*, 64:052312, Oct 2001.
- [99] N. Kiesel. *Experiments on Multiphoton Entanglement*. PhD thesis, LMU, 2007.
- [100] Reinhard F. Werner. Quantum states with einstein-podolsky-rosen correlations admitting a hidden-variable model. *Phys. Rev. A*, 40:4277–4281, Oct 1989.
- [101] O. Gühne, P. Hyllus, D. Bruss, A. Ekert, M. Lewenstein, C. Macchiavello, and A. Sanpera. Experimental detection of entanglement via witness operators and local measurements. *Journal of Modern Optics*, 50(6-7):1079–1102, 2003.
- [102] Christian Schwemmer. private communication, 2013.

- [103] Markus Weber, Jurgen Volz, Karen Saucke, Christian Kurtsiefer, and Harald Weinfurter. Analysis of a single-atom dipole trap. *Physical Review A (Atomic, Molecular, and Optical Physics)*, 73(4):043406, 2006.
- [104] J. Hofmann. *in preparation*. *Phys. Rev. Lett.*, 2013.
- [105] R. Garthoff. Optimierte erzeugung und nachweis von atom-photon-zuständen zur verschränkung räumlich getrennter atome. Master's thesis, Ludwig-Maximilians-Universität München, 2015.
- [106] N. Ortegel. *State readout of single Rubidium-87 atoms for a loophole-free test of Bell's inequality*. PhD thesis, Ludwig-Maximilians-Universität München, 2016.
- [107] Wenjamin Rosenfeld, Daniel Burchardt, Robert Garthoff, Kai Redeker, Norbert Ortegel, Markus Rau, and Harald Weinfurter. Event-ready bell test using entangled atoms simultaneously closing detection and locality loopholes. *Phys. Rev. Lett.*, 119:010402, Jul 2017.
- [108] P.J. Mohr, B.N. Taylor, and D.B. Newell. The 2010 codata recommended values of the fundamental physical constants. Online, 2011. This database was developed by J. Baker, M. Douma, and S. Kotochigova.
- [109] S. Hensler. *Wechselwirkungen in ultrakalten dipolaren Gasen*. PhD thesis, University of Stuttgart, 2004.